UNIVERSITAT DE VALÈNCIA
FACULTAT DE FÍSICA

DOCTORAT EN FÍSICA

Dinàmica de sistemes complexos

Caos, xarxes adaptatives i anàlisi de dades en neurociències

Tesi presentada per
VICENTE BOTELLA SOLER

Dirigida per
JOSÉ ÁNGEL OTEO ARACO

València
Abril, 2012

JOSÉ ÁNGEL OTEO ARACO, Professor titular de la Universitat de València,

CERTIFICA:

Que la present memòria,

"Dinàmica de sistemes complexos: Caos, xarxes adaptatives i anàlisi de dades en neurociències" ha sigut realitzada sota la seua direcció al Departament de Física Teòrica de la Universitat de València, per VICENTE BOTELLA SOLER i constitueix la seua Tesi per optar al grau de Doctor en Física.

I per tal què així conste, en compliment de la legislació vigent, presenta al Departament de Física Teòrica la referida Tesi Doctoral, i signa el present certificat.

Vist i plau tutor de tesi

València, a 27 de març de 2012

José Ángel Oteo Araco

A vosaltres, que heu posat l'amor en aquest temps de treball.

Tots els temps són el mateix temps,
perque només hi ha un temps,
i és temps d'amor i de treball,
de contribuir, entre tothom,
i cadascú en allò que faça...

Vicent Andrés Estellés

Agraïments

Una de les coses que u aprèn treballant amb sistemes dinàmics no lineals és que, de vegades, subtils influències tenen grans conseqüències. Aquesta tesi és, sens dubte, la conseqüència d'un gran nombre d'influències, més o menys subtils, a les quals m'he vist exposat durant la meva trajectòria vital i acadèmica. Sols en puc identificar unes quantes, però les agraïsc totes.

Vull agrair en primer lloc a José Ángel Oteo que acceptés dirigir aquesta tesi i que ho haja fet amb tant de criteri. Per suposat, faig extensiu l'agraïment a Josep Ros. Ha sigut un plaer treballar amb tots dos aquests quatre anys. Hem compartit l'interès pels problemes abordats i han sigut una font inestimable de confiança, coneixement i bons consells.

Així mateix, agraïsc al Departament de Física Teòrica i a la Universitat de València els mitjans i l'espai, físic i humà, on s'ha realitzat aquest treball.

Quan la dèria viatgera m'ha dut a realitzar estades d'investigació fóra de València, he tingut la sort de trobar sempre una generositat genuïna. Vull agrair a Michel Le Van Quyen que m'acollís al seu grup d'investigació de l'Institut du Cerveau et de la Moelle Épinière a París de Juny a Desembre de 2009 i en les visites subsegüents. Cal agrair també l'ajuda i la companyia de Mario Valderrama, Mario Chávez, Jacques Martinerie i la resta de personal de l'ICM. De la mateixa manera, agraïsc a David Broomhead i a Paul Glendinning per acceptar acollir dues estades (Febrer-Juliol 2011 i Febre-Abril 2012) al Center for Interdisciplinary Computational and Mathematical Analysis (CICADA, School of Mathematics) de la universitat de Manchester.

L'assistència a congressos i escoles ha sigut possible gràcies al suport, l'eficàcia i la disponibilitat dels investigadors principals dels dos projectes d'investigació pels quals he transitat, Jesús Navarro i Alberto Fernández-Soto. I també, per suposat, gràcies al personal d'administració i serveis del departament de Física Teòrica de la Universitat de València i de l'Institut de Física Corpuscular (CSIC) que amb el seu treball donen suport constant a la tasca investigadora.

És de rigor fer l'agraïment institucional a la Generalitat Valenciana pel suport econòmic durant aquests quatre anys. No deixa de ser sorprenent i molt d'agrair que no hi haja hagut cap problema de finançament en aquests temps obscurs de deliris pressupostaris.

Vaja també un agraïment, a la bestreta, per als membres del tribunal que han acceptat fer l'esforç de llegir el manuscrit.

Un agraïment especial va per a tots els estudiants, becaris i postdocs, amb els quals he compartit (tant a València com a París i a Manchester) dinars, sopades i cafès, a més de frustracions, discussions (polítiques i científiques) i moltes rialles. La llista és massa

llarga per detallar-la, així que doneu-vos tots per agraïts. Quan la carrera acadèmica sembla una travessia del desert ajuda a mantenir l'ànim tindre tan bona companyia.

La vocació científica té, en el meu cas, un origen incert. Cal, però, reconèixer la influència, molt positiva, de professors i amics com ara Josep Pedro, Josep Lluís Doménech, Jesús Borrull i Rafa Pérez 'Petete' que em contagiaren el seu entusiasme i la seua dedicació per ensenyar ciència. Les lliçons tàcites són, quasi sempre, les més importants.

I deixant el millor i més important per al final, vull agrair a la meva família i a Diana el suport i la confiança constants. La seva influència (la seva estima) és, sens dubte, la més decisiva.

Gata de Gorgos, 25 de març de 2012

Contents

Chapter 1
Introducció

Des de fa ja quasi mig segle i gràcies en gran part a l'aparició dels ordinadors que han augmentat enormement la nostra capacitat de càlcul, la comunitat científica ha començat a afrontar problemes que no havien sigut considerats prèviament, o sols de manera parcial, degut a la seva gran complexitat. Avui en dia, sistemes dinàmics no lineals amb comportament caòtic que no admeten un tractament analític senzill poden ser explorats i compresos amb l'ajuda de simulacions numèriques. De la mateixa manera, sistemes complexos amb propietats emergents que no admeten un tractament estadístic convencional, poden ser modelitzats i simulats en un ordinador. Així mateix, els ordinadors ens permeten també recollir i analitzar enormes quantitats de dades experimentals a la recerca de patrons, correlacions i en definitiva, una millor comprensió de sistemes tan complexos com, per exemple, el cervell.

En aquesta tesi ens acostem a l'estudi de la dinàmica d'aquests sistemes complexos a través de tres camps d'estudi distints i que explicarem a continuació. La tesi s'organitza per tant en tres parts. Cada part consta d'una introducció (en valencià) i una sèrie de capítols (en anglés) on s'exposen la metodologia i els resultats del treball d'investigació. En les introduccions s'expliquen alguns conceptes generals sobre el tema de la part corresponent, es fa un breu resum dels resultats i es situen en un marc més ampli les noves aportacions.

La primera part de la tesi *Dynamics of piecewise defined maps* tracta sobre el treball realitzat junt amb el Prof. José Ángel Oteo i el Prof. Josep Ros en el camp dels sistemes dinàmics discrets definits per funcions definides a trossos. L'estudi d'aquests sistemes m'ha permès aprendre els conceptes i ferraments fonamentals de la dinàmica no lineal i el caos. A més a més, hem fet una contribució nova al camp en descriure i explicar un tipus concret de bifurcació que havia romàs desatès en la literatura. Aquest treball ha estat publicat en tres articles en diferents revistes científiques [1, 2, 3].

La segona part de la tesi *Adaptive networks and Polysynchrony* és el fruit de la col·laboració amb el Prof. Paul Glendinning del *Centre for Interdisciplinary Computational and Dynamical Analysis* (CICADA-School of Mathematics) de la Universitat de Manchester (Regne Unit) en el camp de les xarxes complexes adaptatives. Durant els meus estudis doctorals he realitzat dues estades d'investigació de llarga durada en aquest centre (Febrer-Juny 2011 i Febrer-Abril 2012). En aquesta col·laboració he aprofundit en l'estudi dels fenòmens de sincronització, característics dels sistemes complexos, i en els models de xarxes complexes. El principal resultat d'aquest treball és la introducció d'un model de xarxa complexa adaptativa en el qual la xarxa evoluciona cap a estructures jeràrquiques i la dinàmica és polisíncrona per a certs valors del paràmetre. La descripció d'aquest model i de les seves característiques més rellevants s'ha publicat a la revista Europhysics Letters [4].

En la tercera part de la tesi *Analysing real-world complex dynamics: The sleep slow waves* s'exposa el treball realitzat en col·laboració amb el grup del Prof. Michel Le Van Quyen al *Centre de Recherche de l'Institut du Cerveau et de la Moelle Épinière* (CRICM) a París (França) estudiant la dinàmica de les ones lentes cerebrals a partir de l'anàlisi de dades electroencefalogràfiques intracranials. Aquesta col·laboració començà amb la realització d'una estada d'investigació al CRICM entre Juny i Desembre de 2009. Els resultats que es descriuen en aquesta part han estat publicats a la revista PLoS ONE [5].

En aquesta tesi, per tant, es resumeixen els diferents treballs d'investigació realitzats en els últims quatre anys (2008-2012) en el camp de la dinàmica no lineal i els sistemes complexos des d'aproximacions tant teòriques com experimentals.

Vicent Botella i Soler
Manchester, març de 2012

Part I
Dynamics of piecewise defined maps

Chapter 2
Introducció: dinàmica caòtica i sistemes dinàmics discrets

2.1 Orígens de l'estudi de la dinàmica caòtica

Les matemàtiques han demostrat ser una eina molt útil per a l'estudi del món natural. Al segle XVII, la publicació per part d'Isaac Newton (1642-1727) dels seus *Philosophiae Naturalis Principia Mathematica* (1687) ens va dur a un esclat d'entusiasme i de confiança en la nostra capacitat de formular, d'una manera comprensible i útil, lleis matemàtiques per descriure el món que ens envolta. Entre altres coses, en els *Principia*, Newton enuncià els seus famosos tres principis i la llei de la gravitació universal. Açò li va permetre, per exemple, calcular l'òrbita d'un planeta al voltant del Sol i deduir per tant, de forma rigorosa, les lleis fenomenològiques enunciades per Johannes Kepler (1571-1630) un segle abans (*Astronomia Nova*, 1609). La diferència entre saber que un planeta transcorre en òrbites el·líptiques al voltant del Sol - com sabia Kepler - i saber quina equació regeix el moviment d'aquest planeta - com va deduir Newton - és fonamental: la capacitat de fer prediccions. En el cas del problema de dos cossos en interacció gravitatòria - per exemple, el Sol i un planeta - les matemàtiques de la gravetat clàssica ens permeten, donades les condicions del problema en un instant donat - posició del planeta, velocitat, massa, etc. -, predir l'evolució futura del sistema.

Al segle XVIII la confiança en la capacitat predictiva de les lleis naturals formulades matemàticament era tal que el matemàtic francès Pierre-Simon Laplace (1749-1827) escriuria al seu *Essai philosophique sur les probabilités* (1814)

> Une intelligence qui, à un instant donné, connaîtrait toutes les forces dont la nature est animée et la situation respective des êtres qui la compose embrasserait dans la même formule les mouvements des plus grands corps de l'univers et ceux du plus léger atome; rien ne serait incertain pour elle, et l'avenir, comme le passé, serait présent à ses yeux.[1]

És a dir, aquesta intel·ligència, el famós dimoni o geni de Laplace, podria predir hipotèticament l'evolució de qualsevol sistema físic - inclòs l'univers com un tot - donades les condicions del sistema en un instant de temps determinat.

La confiança en aquest poder predictiu es va veure reforçada pel descobriment del planeta Neptú per part del també francès Urban Jean Joseph Le Verrier (1811-1877). L'òrbita d'Urà - que havia sigut descobert observacionalment per William Herschel (1738-1822) l'any 1781- no s'ajustava a les prediccions newtonianes i aquest era un problema que preocupava molt els astrònoms de l'època. Le Verrier va calcular l'òrbita que hauria de seguir un hipotètic planeta situat més enllà d'Urà per tal de causar les

[1] Una intel·ligència que, en un instant donat, coneguera totes les forces que donen moviment a la natura i la posició de tots els cossos que la composen, resumiria en una sola fórmula els moviments dels cossos més grans de l'univers i els del més petit àtom; res seria incert per a aquesta intel·ligència, i el futur, així com el passat, es presentarien davant dels seus ulls.

anomalies observades. En 1846 Le Verrier envià una carta a l'astrònom Johann Gottfried Galle (1812-1910) a l'observatori de Berlin indicant-li la posició on havia de buscar aquest hipotètic planeta. La nit del 23 de Setembre, el mateix dia que reberen la carta, Galle i Heinrich Louis d'Arrest (1822-1875) observaren Neptú per primera vegada a tan sols 1º de la posició predita per Le Verrier. A l'astrònom francès - de parla catalana - Francesc Arago (1786-1853), que dirigia en aquell moment l'Observatori de Paris, se li atribueix una frase que resumeix tota la potència del paradigma determinista, en dir que Le Verrier havia descobert una planeta "amb la punta del seu llapis". No obstant, la nostra confiança sense mesura en el poder de predicció de les lleis naturals en forma matemàtica no havia de romandre il·lesa molts més anys.

Paradoxalment, fou el propi sistema solar, que havia sigut el sistema on el determinisme havia recollit els seus millors fruits, el primer sistema en presentar resistència a la capacitat predictiva de les lleis de Newton. Si bé el problema de dos cossos en interacció gravitatòria és de fàcil resolució (avui dia és matèria dels primers cursos de física general), el problema de tres o més cossos no té una solució gens senzilla. De fet, com veurem, no té una solució general i analítica [6].

Podem dir que la primera i més exitosa aproximació al problema fou la del matemàtic francès Henri Poincaré (1854-1912). Amb motiu del seu 60 aniversari, el rei Òscar II de Suècia (1829-1907) convocà un concurs matemàtic que tenia com a un dels possibles temes l'estabilitat del sistema solar o problema dels N cossos. Poincaré guanyà el concurs amb el treball *Sur le probléme des trois corps et les équations de la dynamique* (1889). Poincaré demostrava en aquest treball que el problema dels tres cossos no té solució general - diem que és un sistema no integrable - i que la dinàmica d'aquest sistema pot ser increïblement complicada segons quines siguen les condicions inicials: s'havia descobert el caos.

Tanmateix, la dinàmica caòtica hauria d'esperar encara quasi un segle per ser redescoberta i convertir-se en un camp d'investigació fructífer gràcies, en gran part, al desenvolupament de les tècniques gràfiques i computacionals necessàries per simular o resoldre aquest tipus de sistemes.

El redescobriment del caos en la segona meitat del segle XX li'l devem al meteoròleg i matemàtic estatunidenc Edward N. Lorenz (1917-2008). Lorenz estudià un model de convecció atmosfèrica de sols tres variables [7]

$$\dot{x} = \sigma(y - x), \tag{2.1}$$
$$\dot{y} = -xz + rx - y, \tag{2.2}$$
$$\dot{z} = xy - bz. \tag{2.3}$$

En intentar trobar la solució numèrica d'aquest sistema no lineal, Lorenz detectà que la dinàmica podia ser fortament irregular i que l'evolució del sistema depenia d'una manera dramàtica de les condiciones inicials del problema. A la figura 2.1 s'observa l'evolució temporal d'una de les variables del model de Lorenz per a dues condicions inicials lleugerament diferents. L'evolució del sistema no segueix cap patró regular i a més, les dues òrbites divergeixen ràpidament (exponencialment) amb el temps.

Aquestes són dues de les característiques fonamentals de la dinàmica caòtica. De fet, Steven Strogatz (1959-) defineix caos com un *comportament aperiòdic a llarg termini en un sistema determinista que presenta sensibilitat extrema a les condicions inicials* [8]. Aquest conceptes seran definits d'una manera més formal en les seccions següents.

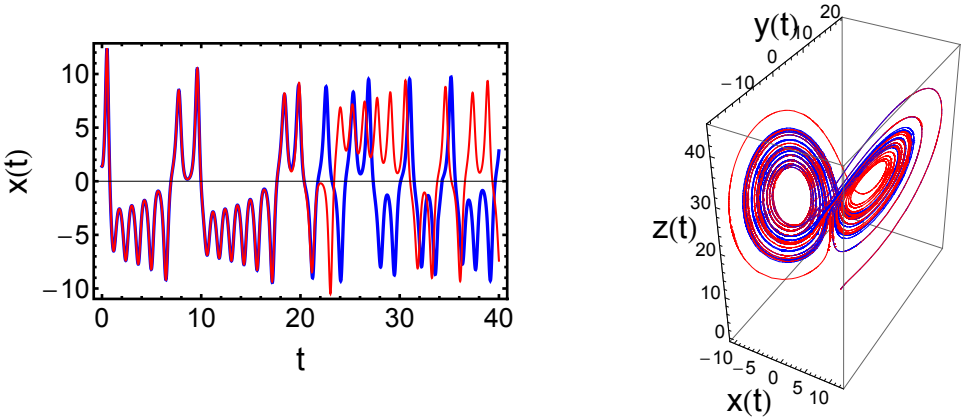

Figura 2.1 *Esquerra*: exemple de solucions del sistema de Lorenz per a la variable x amb diferents condicions inicials ($x_0 = 1.4$ en blau, $x_0 = 1.4003$ en roig). *Dreta*: atractor de Lorenz.

2.2 Sistemes dinàmics discrets

Un dels camps en els quals més s'ha estudiat la dinàmica caòtica ha sigut el dels sistemes dinàmics discrets. De fet, el terme 'caos' s'emprà per primera vegada en la literatura científica en un article sobre sistemes dinàmics discrets unidimensionals publicat el 1975 [9]. Un sistema dinàmic discret, en el sentit en què ho emprarem en aquesta tesi, és el resultat del procés d'iteració d'una aplicació f d'un cert espai en ell mateix $f : E \to E$, $E \subset \mathbb{R}^n$,

$$\mathbf{x}_{n+1} = f(\mathbf{x}_n), \quad \mathbf{x} \in E. \tag{2.4}$$

Donada una condició inicial $\mathbf{x}_0$, la iteració de f ens permet calcular una òrbita o trajectòria, definida com el conjunt de valors $S_{\mathbf{x}_0} = \{\mathbf{x}_0, \mathbf{x}_1, \mathbf{x}_2, \mathbf{x}_3, \dots\}$. L'estudi de la dinàmica dels sistemes dinàmics discrets és bàsicament l'estudi de l'evolució d'aquestes òrbites quan n tendeix a infinit. En aquest sentit, definim *atractor* de f un conjunt en l'espai E cap al qual evolucionen un conjunt de condicions inicials - *conca d'atracció* - quan $n \to \infty$. Una aplicació pot tenir simultàniament més d'un atractor i aquests poden ser estables o inestables segons si condicions inicials pròximes a ells evolucionen cap a l'atractor o s'allunyen d'ell.

Els tipus més senzills d'atractors en sistemes dinàmics discrets són el punt fix i el cicle límit. Direm que un punt $\mathbf{x}^*$ és un punt fix de l'aplicació f si

$$\mathbf{x}^* = f(\mathbf{x}^*). \tag{2.5}$$

En el cas més general, l'estabilitat dels punts fixos s'estudia fent l'aproximació lineal al voltant del punt i estudiant els autovalors λ_i, $i = 1 \dots n$, de la matriu jacobiana en el punt

$$J(\mathbf{x}) = \begin{pmatrix} \frac{\partial f_1}{\partial x_1} & \cdots & \frac{\partial f_1}{\partial x_n} \\ \vdots & & \vdots \\ \frac{\partial f_n}{\partial x_1} & \cdots & \frac{\partial f_n}{\partial x_n} \end{pmatrix}. \tag{2.6}$$

La taula 2.1 conté una breu classificació dels diferents tipus de punt fix que podem trobar en funció dels autovalors de la matriu jacobiana.

Punt fix	Autovalors	Estabilitat
Engolidor	$\lvert\lambda_i\rvert < 1, \forall i$	Estable
Font	$\lvert\lambda_i\rvert > 1, \forall i$	Inestable
Punt de sella	$\lvert\lambda_i\rvert < 1, i = 1 \dots m$ $\lvert\lambda_j\rvert > 1, j = m \dots n$	Inestable

Taula 2.1 Classificació dels punts fixos segons els autovalors de la matriu jacobiana.

Un altre tipus d'atractor molt comú en la dinàmica dels sistemes dinàmics discrets és l'atractor periòdic o cicle límit. Per tal de definir òrbita periòdica cal introduir primer el concepte d'iterada enèsima. La iterada enèsima de l'aplicació f és l'aplicació resultant de composar n vegades f i es representa com

$$f^n(\mathbf{x}) = f(f(f \dots^n \dots f(\mathbf{x}))). \tag{2.7}$$

Amb açò ja podem definir una òrbita periòdica de període k com el conjunt de k punts $S^k = \{\mathbf{x_1}, \dots, \mathbf{x_k}\}$ tals que

$$f^k(\mathbf{x_i}) = \mathbf{x_i},\ f^l(\mathbf{x_i}) \neq \mathbf{x_i},\ 1 < l < k-1, \forall \mathbf{x_i} \in S^k \tag{2.8}$$

Evidentment, els elements d'una òrbita de període k de l'aplicació f són punts fixos de la iterada k-èsima d'aquesta.

L'estabilitat de les òrbites periòdiques es pot estudiar de dues maneres. Podem estudiar l'estabilitat dels punts fixos de la iterada k-èsima fent ús d'aquesta per calcular la matriu jacobiana com hem explicat abans. Tanmateix, aquesta opció pot ser força laboriosa si k és un nombre gran i f no és senzilla. La segona opció és fer ús de la regla de la cadena per calcular la matriu jacobiana de la iterada k-èsima com a producte de matrius jacobianes de l'aplicació f avaluades en els punts de l'òrbita periòdica

$$J_k = J(\mathbf{x_1})J(\mathbf{x_2}) \dots J(\mathbf{x_k}). \tag{2.9}$$

De la mateixa manera que per als punts fixos, els cicles límit poden ser estables ($|\lambda_i| < 1$) o inestables ($|\lambda_i| > 1$).

Fins ací els atractors regulars. En la secció següent introduïm el tercer tipus d'atractors: els atractors caòtics.

2.3 Caos en sistemes dinàmics discrets: l'aplicació logística

L'origen de l'estudi del caos en aplicacions discretes està lligat a l'estudi de la dinàmica de poblacions. Al segle XVIII, Thomas R. Malthus (1766-1834) proposava en el seu *An Essay on the Principle of Population* (1798) que en absència de limitacions de recursos, les poblacions creixen de manera exponencial. Matemàticament, el creixement proposat per Malthus es pot escriure com

$$\frac{dx}{dt} = gx, \tag{2.10}$$

on x representa densitat de població.

Uns anys més tard, un matemàtic belga anomenat Pierre-François Verhulst (1804-1849), preocupat pel problema de la població màxima que podria assolir la seva recentment estrenada nació, es dedicà a estudiar l'evolució de poblacions quan els recursos no son il·limitats. En un treball presentat a l'Acadèmia de Ciències belga i publicat l'any

1845 sota el títol *Recherches mathématiques sur la loi d'accroissement de la population* Verhulst introduí l'anomenada equació logística [10]

$$\frac{dx}{dt} = gx(1-\frac{x}{k}), \tag{2.11}$$

que té com a solució

$$x(t) = \frac{k}{1+C\exp(-gt)}, \quad C = \frac{k-x(0)}{x(0)}. \tag{2.12}$$

El terme $(1-\frac{x}{k})$ en (2.11) s'introdueix per limitar el creixement exponencial de la densitat de població x, on el paràmetre k representa el valor màxim de la població que el sistema pot suportar. A partir de la solució podem veure fàcilment que, independentment de la condició inicial, la població s'estabilitza sempre en el seu valor màxim

$$\lim_{t\to\infty} x(t) = k. \tag{2.13}$$

Discretitzant l'equació diferencial trobem una aplicació discreta amb una dinàmica molt interessant. L'anomenada aplicació logística ve donada per

$$x_{n+1} = f(x_n) = rx_n(1-x_n), \tag{2.14}$$

on x és un nombre real entre 0 i 1 que representa densitat de població respecte d'un valor màxim (k en l'equació diferencial). Dins l'interval $r \in [0,4]$, l'aplicació logística és una aplicació contínua de l'interval $I = [0,1]$ en ell mateix, $f : I \to I$. En funció del valor del paràmetre r, l'evolució de les successives x_n pot tendir a un valor constant - punt fix -, oscil·lar entre un nombre fix de valors - òrbita periòdica - o ser caòtica. El caràcter caòtic de l'aplicació logística fou estudiat per Robert May (1938-) en un article publicat el 1976 [11].

A la figura 2.2 podem veure un diagrama de bifurcació de l'aplicació logística. En aquest tipus de diagrama es representen els valors x_n en l'atractor en funció del paràmetre r.

Per a $r < 1$ l'únic punt fix estable és $x = 0$. En $r = 1$ el punt $x = 0$ passa a ser inestable i quan r augmenta apareix com a punt fix estable $x = 1 - \frac{1}{r}$. Açò es deu a un fenomen anomenat bifurcació transcrítica que explicarem amb més detall en la secció següent. Aquest punt fix és estable fins $r = 3.0$, on perd el seu caràcter estable i apareix una òrbita periòdica de període 2. A partir d'ací trobem el que s'anomena en la literatura una *cascada de duplicació de període*. L'òrbita de període 2 esdevé inestable donant lloc a una òrbita de període 4. Aquesta perd l'estabilitat en aparèixer una òrbita de període 8 i així successivament. Els valors de r per als quals existeix una bifurcació de duplicació de període els denotarem per r_n. Podem construir així la taula 2.2. S'observa tant en el diagrama de bifurcació com en la taula que els intervals entre bifurcacions de duplicació de període són cada vegada més menuts a mesura que augmenta r, arribant a un valor limit r_∞. Per a $r > r_\infty$ trobem ja òrbites caòtiques. Convé remarcar ací que aquesta cascada de duplicació de període va donar lloc al descobriment de dues noves constants matemàtiques. Ambdues foren descobertes per Mitchell J. Feigenbaum (1944-) [12, 13] i es defineixen així [8]

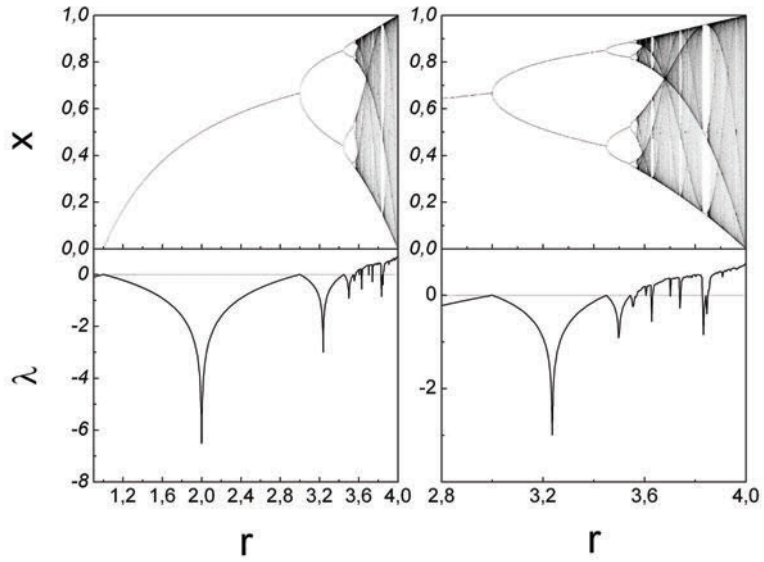

Figura 2.2 Diagrama de bifurcació i exponent de Lyapunov de l'aplicació logística en funció del paràmetre r.

r_n	Període
$r_1 = 3$	2
$r_2 = 3.449\ldots$	4
$r_3 = 3.54409\ldots$	8
$r_4 = 3.5644\ldots$	16
$r_5 = 3.568759\ldots$	32
$\ldots$	$\ldots$
$r_\infty = 3.569946\ldots$	∞

Taula 2.2 Valors del paràmetre r de l'aplicació logística per als quals hi ha una duplicació de període. El valor r_∞ representa el punt d'acumulació o frontera del caos.

$$\delta = \lim_{n\to\infty} \frac{r_n - r_{n-1}}{r_{n+1} - r_n} = 4.669\ldots, \tag{2.15}$$

$$\alpha = \lim_{n\to\infty} \frac{d_n}{d_{n+1}} = -2.5029\ldots \tag{2.16}$$

on d_n és la distància més curta d'una branca del diagrama de bifurcació al màxim de l'aplicació (en el cas de la logística, el màxim es troba sempre a $x = 0.5$). El més interessant d'aquestes constants és el seu caràcter universal donat que es pot demostrar que no depenen de la forma concreta de l'aplicació f sinó que són vàlides per a, bàsicament, qualsevol aplicació contínua unimodal (amb un sol màxim) de l'interval $[0,1]$ en ell mateix. A més a més, les constants de Feigenbaum s'han determinat també experimentalment en sistemes físics que presenten cascades de duplicació de període en alguna variable sota la variació d'un paràmetre [8].

En [14], Robert Devaney (1948-) introduí una definició formal d'aplicació caòtica. Aquesta definició requereix però de dues definicions prèvies.

Definició. Siga V un cert espai. Diem que l'aplicació $f : V \to V$ és *transitiva* si per a qualsevol parella de conjunts $U, W \subset V$, existeix un $k > 0$ tal que $f^k(U) \bigcap W \neq \emptyset$.

Definició. Diem que l'aplicació $f : V \to V$ presenta *sensibilitat extrema a condicions inicials* si existeix un $\delta > 0$ tal que, per a qualsevol $x \in V$ i qualsevol entorn N de x, existeix $y \in N$ i $n \geq 0$ tals que $|f^n(x) - f^n(y)| > \delta$.

Amb açò ja podem definir aplicació caòtica.

Definició. Diem que l'aplicació $f : V \to V$ és caòtica en V si

1. f és transitiva.
2. el conjunt dels punts periòdics de f és dens en V.
3. f presenta sensibilitat extrema a condicions inicials.

Més enllà de r_∞, enmig de les regions de dinàmica caòtica, apareixen finestres (intervals de r) per a les quals la dinàmica torna a ser regular. La més clara és sens dubte la finestra de període 3 que comença en $r = 1+\sqrt{8} = 3.828427\ldots$. Es pot demostrar que la seqüència en la que apareixen les finestres regulars de diferents períodes és també una propietat universal de totes les aplicacions de la forma $x_{n+1} = rg(x_n)$ on $g(x)$ és, bàsicament, una funció contínua, univaluada, positiva i amb un única màxim $g_{max} \leqslant 1$ en $[0,1]$ tal que $g'(g_{max}) = 0$ i amb $g(0) = g(1) = 0$ (per a la resta de condicions consultar [15]). És a dir, dins la regió caòtica, els períodes dels atractors periòdics apareixen sempre en el mateix ordre. Aquest ordre s'anomena seqüència U i fins a període 6 té aquesta forma

$$1,2,2\times 2,6,5,3,2\times 3,5,6,4,6,5,6. \tag{2.17}$$

Un altre resultat interessant per al cas de les aplicacions discretes definides per funcions contínues dels reals en els reals, $f : \mathbb{R} \to \mathbb{R}$, és l'anomenat teorema de Sarkovskii (en honor del matemàtic ucraïnès Oleksandr Mikolaiovich Sarkovskii (1936-)). Definim el següent ordenament

$$\begin{aligned}
&3 \prec 5 \prec 7 \prec 9 \prec \ldots \\
&\prec 2\cdot 3 \prec 2\cdot 5 \prec 2\cdot 7 \prec 2\cdot 9\ldots \\
&\prec 2^2\cdot 3 \prec 2^2\cdot 5 \prec 2^2\cdot 7 \prec 2^2\cdot 9\ldots \\
&\ldots \quad \ldots \quad \ldots \quad \ldots \\
&\ldots \prec 2^4 \prec 2^3 \prec 2^2 \prec 2^1 \prec 1.
\end{aligned}$$

Suposem ara que dos nombres p i q satisfan $p \prec q$ en aquest ordenament. Aleshores el teorema de Sarkovskii ens assegura que si l'aplicació f té una òrbita periòdica de període p aleshores també en té una de període q.

Cal adonar-se'n que si una aplicació f té una òrbita de període 3, aleshores també té òrbites de qualsevol període enter, incloses òrbites de període infinit o caòtiques. Aquest resultat fou publicat de manera independent per Li i Yorke en 1975, en el seu famós article titulat *Period three implies chaos* [9].

És convenient destacar que el teorema de Sarkovskii no diu res però sobre l'estabilitat de les òrbites. Per exemple, en la finestra de període 3 de l'aplicació logística, el teorema de Sarkovskii ens indica que hi ha òrbites de qualsevol període, però sols l'òrbita de període 3 és estable.

Exponent de Lyapunov

Com hem vist abans, una de les característiques que distingeix un sistema caòtic és la sensibilitat extrema a canvis en les condicions inicials. Una manera de mesurar aquesta sensibilitat i per tant el grau de caos d'un sistema, és mitjançant l'anomenat exponent de Lyapunov (en honor del matemàtic rus Aleksandr Mikhailovich Lyapunov (1857-1918)).

Suposem dues condicions inicials molt pròximes x_0 i $\overline{x_0}$ separades per una distancia

$$\delta_0 = \bar{x_0} - x_0.$$

La distància en la iteració n entre les trajectòries seguides a partir de cada condición inicial vindrà donada per

$$\begin{aligned}\delta_n = \bar{x_n} - x_n &= f^n(\bar{x_0}) - f^n(x_0) \\ &= f^n(x_0 + \delta_0) - f^n(x_0) \\ &= f^n(x_0) + \delta_0 \frac{df^n}{dx}\Big|_{x_0} + \mathcal{O}(\delta_0^2) - f^n(x_0) \\ &\approx \delta_0 \frac{df^n}{dx}\Big|_{x_0}.\end{aligned}$$

Finalment, aplicant la regla de la cadena trobem

$$\delta_n \approx \delta_0 \prod_{k=0}^{n-1} \frac{df}{dx}\Big|_{x_k} \tag{2.18}$$

Aprofitant aquest resultat, podem escriure

$$\begin{aligned}\Big|\frac{\delta_n}{\delta_0}\Big| &= \exp(\ln\Big|\frac{\delta_n}{\delta_0}\Big|) \\ &\approx \exp(\sum_{k=0}^{n-1} \ln|f'(x_k)|) \\ &\approx \exp(n\lambda_n),\end{aligned}$$

on

$$\lambda = \lim_{n\to\infty} \lambda_n = \lim_{n\to\infty} \frac{1}{n} \sum_{k=0}^{n-1} \ln|f'(x_k)| \tag{2.19}$$

és l'exponent de Lyapunov.

Si l'exponent Lyapunov és positiu les trajectòries s'allunyen augmentat la seua distància de manera exponencial i provant així la sensibilitat extrema a condicions inicials. Un exponent de Lyapunov positiu és un bon indicador de dinàmica caòtica. Per contra, un exponent de Lyapunov negatiu ens indica que la dinàmica és regular, és a dir, les trajectòries de dues condicions inicials pròximes no divergeixen de manera exponencial. A la figura 2.2 podem observar l'exponent de Lyapunov per a l'aplicació logística en funció del paràmetre r. Aquest és negatiu en la cascada de duplicació de període i en les finestres de regularitat, i positiu en les regions caòtiques. Convé destacar que cada òrbita - cada condició inicial - d'una aplicació té associat un determinat exponent de Lyapunov. Si l'aplicació sols té un atractor, com en el cas de l'aplicació logística, el que se sol representar és el promedi dels exponents de Lyapunov calculats sobre un gran nombre de condicions inicials. En l'apèndix E d'aquesta part de la tesi descrivim en detall el càlcul d'exponents de Lyapunov en el cas general d'aplicacions discretes n-dimensionals.

Diagrama *cobweb* o de Verhulst

Una ferramenta gràfica molt útil a l'hora d'il·lustrar i estudiar la dinàmica de sistemes dinàmics discrets unidimensionals és l'anomenat diagrama *cobweb* o de Verhulst. Es tracta d'un algorisme bastant senzill [16] que permet desenvolupar una certa intuïció

sobre la dinàmica d'aquest tipus de sistemes a partir del gràfic de la funció que defineix l'aplicació.

En primer lloc dibuixem en uns eixos de coordenades la funció $f(x)$ que defineix el sistema discret $x_{n+1} = f(x_n)$. Dibuixem també la recta bisectriu de pendent unitat $x_{n+1} = x_n$. Ara, donada una condició inicial x_0, podem construir gràficament la seva òrbita de la següent manera:

- Des de l'abcissa x_0 tracem una línia vertical fins tocar la corba $f(x)$.
- Des d'aquest punt dibuixem una línia horitzontal fins intersecar la bisectriu $x_{n+1} = x_n$. L'abcissa d'aquest nou punt és la primera iteració $x_1 = f(x_0)$.

Repetint aquest procés trobarem tots els punts de l'òrbita de x_0. A la figura 2.3 il·lustrem aquest mètode amb tres exemples de l'aplicació logística amb diferent comportament dinàmic.

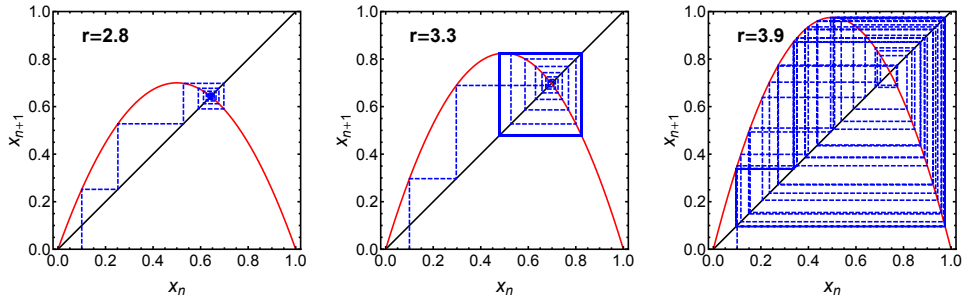

Figura 2.3 Tres exemples de diagrama *cobweb* per a l'aplicació logística $x_{n+1} = rx_n(1-x_n)$. En els tres casos es representen les primeres 300 iteracions de l'òrbita de la condició inicial $x_0 = 0.1$. Per a $r = 2.8$ l'òrbita evoluciona cap a un punt fix. Quan $r = 3.3$, l'òrbita tendeix a un cicle límit de període 2. En el cas $r = 3.9$ la dinàmica és clarament caòtica.

2.4 Bifurcacions en aplicacions contínues

Són molts els treballs i llibres de text que tracten sobre els fenòmens de bifurcació en aplicacions definides per funcions contínues unidimensionals. Tanmateix, la nomenclatura i el tractament teòric varia fortament segons el text. És per açò que ens ha semblat convenient fer un breu resum d'aquests fenòmens tant per unificar nomenclatura com per establir un contrast amb les bifurcacions en aplicacions definides per funcions discontínues que tractarem en aquesta part de la tesi. Aquesta introducció a la teoria de bifurcacions està basada en gran part en el text de referència sobre aquest tema de Wiggins [17] així com en el text de Romera [16].

Comencem considerant el cas general d'una aplicació n-dimensional $\mathbb{R}^n \to \mathbb{R}^n$ amb p paràmetres

$$y \mapsto g(y,\lambda), \quad y \in \mathbb{R}^n, \quad \lambda \in \mathbb{R}^p, \tag{2.20}$$

on g és una funció $\mathscr{C}^r$ ($r \geq 5$ sol bastar) en un conjunt obert suficientment gran en $\mathbb{R}^n \times \mathbb{R}^p$ i λ és un conjunt de paràmetres. Suposem ara que aquesta aplicació té un punt fix (y_0, λ_0) tal que

$$g(y_0, \lambda_0) = y_0, \tag{2.21}$$

i ens preguntem el següent sobre aquest punt fix: És estable o inestable? Com canvia l'estabilitat (o inestabilitat) del punt fix quan variem els paràmetres λ?

Per respondre aquestes preguntes linealitzarem l'aplicació al voltant del punt fix

$$\xi \mapsto D_y g(y_0, \lambda_0)\xi, \quad \xi \in \mathbb{R}^n, \tag{2.22}$$

on $D_y g(y_0, \lambda_0)$ és la matriu jacobiana de l'aplicació g avaluada en el punt fix. Si el punt fix és hiperbòlic (cap autovalor de $D_y g(y_0, \lambda_0)$ te mòdul unitat) l'estabilitat (inestabilitat) en l'aproximació lineal implica estabilitat (inestabilitat) del punt fix de l'aplicació original no lineal. A partir del Teorema de la Funció Implícita es pot demostrar que, en un entorn suficientment menut de (y_0, λ_0), per a cada λ existeix un únic punt fix amb la mateixa estabilitat que (y_0, λ_0). Els punts hiperbòlics no tenen per tant interés dinàmic donat que no poden 'bifurcar-se', és a dir, canviar la seva estabilitat i originar l'aparició de nous atractors. Tanmateix, si el punt fix no és hiperbòlic, l'aproximació lineal no pot emprar-se per determinar l'estabilitat del punt fix i un canvi en λ pot traduir-se en la creació de noves òrbites.

A continuació resumim en una llista els exemples bàsics de punts no hiperbòlics i les bifurcacions associades a aquests en funció dels autovalors de la matriu jacobiana.

1. $D_y g(y_0, \lambda_0)$ té un autovalor igual a $+1$ (amb els $(n-1)$ restants amb mòdul diferent de la unitat):
   - Bifurcació Tangent (també anomenada *Saddle-node* o *Fold*)
   - Bifurcació Transcrítica
   - Bifurcació Forca
2. $D_y g(y_0, \lambda_0)$ té un autovalor igual a -1 (amb els $(n-1)$ restants amb mòdul diferent de la unitat):
   - Bifurcació *Flip* (també anomenada Subharmònica o de duplicació de període)
3. $D_y g(y_0, \lambda_0)$ té dos autovalors complex conjugats amb mòdul igual a $+1$ (diferents a les primeres 4 arrels d'1) amb els $(n-2)$ autovalors restants amb mòdul diferent de la unitat:
   - Bifurcació Neimarck-Sacker

En la Taula 2.3 i la figura 2.4 es resumeixen les principals característiques de les bifurcacions dels casos 1 i 2 donat que són els únics que es presenten en aplicacions unidimensionals.

Autovalor	Nom	Condicions	Observacions	Exemple	Fenomenologia
+1	Tangent	$f_\mu(0,0) \neq 0$ $f_{xx}(0,0) \neq 0$		$f(x,\mu) = x + \mu \pm x^2$	$\emptyset \leftrightarrow 1\,\text{p.f.Est.} + 1\,\text{p.f.Inest.}$
	Transcrítica	$f_\mu(0,0) = 0$ $f_{\mu x}(0,0) \neq 0$ $f_{xx}(0,0) \neq 0$		$f(x,\mu) = x + \mu x \pm x^2$	$1\,\text{p.f.Est.} + 1\,\text{p.f.Inest.} \leftrightarrow 1\,\text{p.f.Inest.} + 1\,\text{p.f.Est.}$
	Forca	$f_\mu(0,0) = 0$ $f_{xx}(0,0) = 0$ $f_{\mu x}(0,0) \neq 0$ $f_{xxx}(0,0) \neq 0$	$f_{xxx}(0,0) < 0$ Supercrítica $f_{xxx}(0,0) > 0$ Subcrítica	$f(x,\mu) = a\mu x + bx^3$	$1\,\text{p.f.Est.} \leftrightarrow 1\,\text{p.f.Inest.} + 2\,\text{p.f.Est.}$ (Super) $1\,\text{p.f.Inest.} \leftrightarrow 2\,\text{p.f.Inest.} + 1\,\text{p.f.Est.}$ (Sub)
-1	Flip	$f^2_\mu(0,0) = 0$ $f^2_{xx}(0,0) = 0$ $f^2_{\mu x}(0,0) \neq 0$ $f^2_{xxx}(0,0) \neq 0$	$c = -2f_{xxx}(0,0) - 3(f_{xx}(0,0))^2$ $c < 0$ Supercrítica $c > 0$ Subcrítica	$f(x,\mu) = -x - \mu x + x^3$	Supercrítica: $2\,\text{p.f.Inest.} + 1\,\text{p.f.Est.} \leftrightarrow 3\,\text{p.f.Inest.} + 1\,\text{cicle T} = 2$

Taula 2.3 Classificació de les bifurcacions en aplicacions contínues unidimensionals. Suposem en tots els casos una aplicació unidimensional amb un sol paràmetre $f(x,\mu)$ que presenta un punt fix no hiperbòlic en $(x,\mu) = (0,0)$. La primera columna indica el signe de l'autovalor (de mòdul unitat) de la matriu jacobiana. En la tercera i quarta columna es detallen les condicions sobre les derivades de l'aplicació ($f_x = \frac{\partial f}{\partial x}$, $f_{xx} = \frac{\partial^2 f}{\partial x^2}$, etc.) per tal d'observar una bifurcació d'un determinat tipus en $(x,\mu) = (0,0)$. En la quinta columna s'indiquen alguns exemples d'aplicacions que presenten la bifurcació corresponent. L'última columna resumeix la fenomenologia de la bifurcació: en una bifurcació tangent, per exemple, passem de ningún punt fix per a $\mu < 0$ a observar 1 punt fix estable i 1 punt fix inestable per a $\mu > 0$.

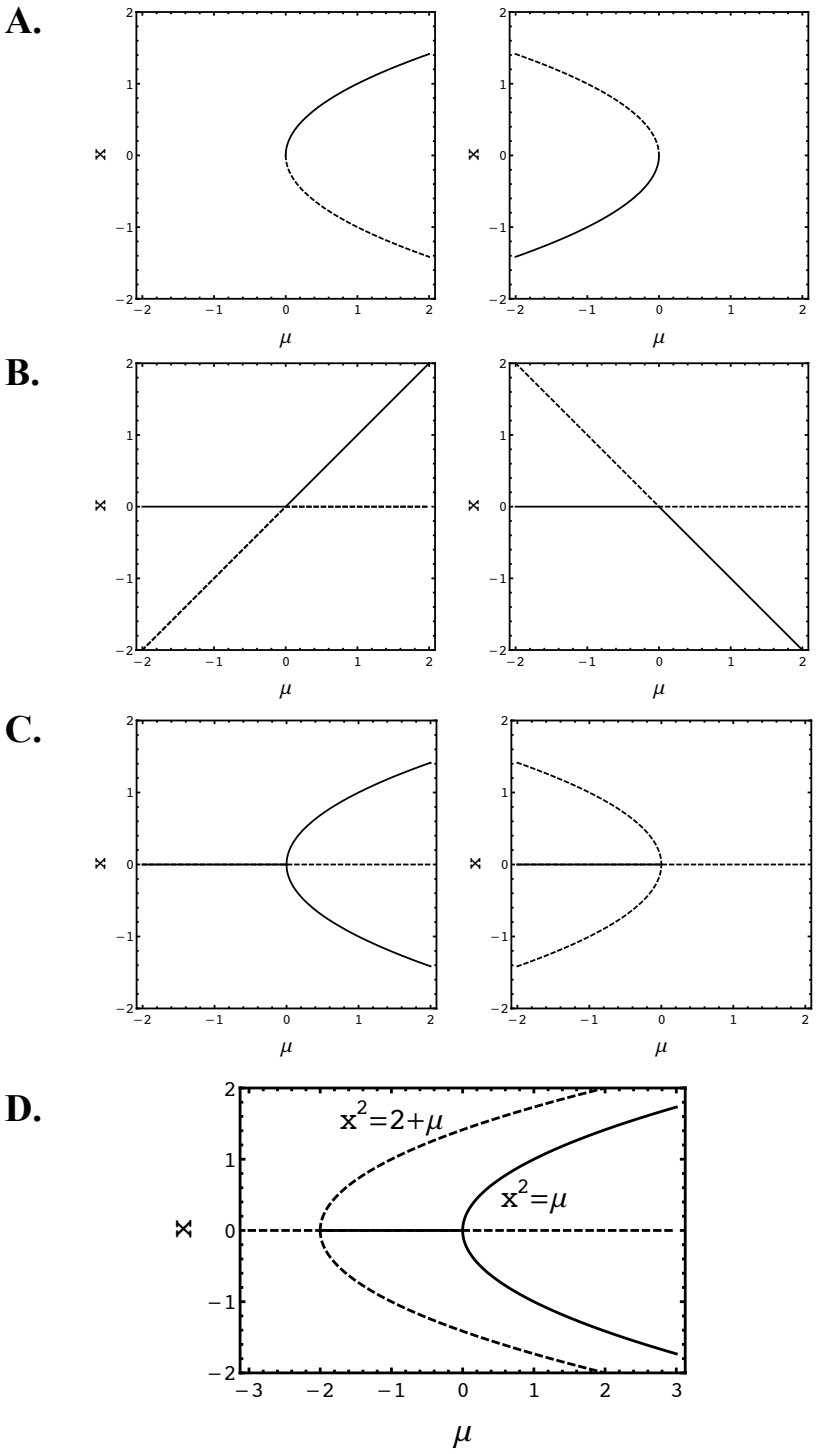

Figura 2.4 Corbes de punt fix de la bifurcació les diferents bifurcacions descrites a la Taula 2.3. Les línies contínues representen punts fixos estables i les discontínues punts fixos inestables. **A.** Bifurcació tangent. *Esquerra:* $f(x,\mu) = x+\mu-x^2 \to x^2 = \mu$. *Dreta:* $f(x,\mu) = x+\mu+x^2 \to x^2 = -\mu$. **B.** Bifurcació transcrítica. *Esquerra:* $f(x,\mu) = x+\mu x-x^2$. *Dreta:* $f(x,\mu) = x+\mu x+x^2$. **C.** Bifurcació forca. *Esquerra:* $f(x,\mu) = x+\mu x-x^3$. *Dreta:* $f(x,\mu) = x+\mu x+x^3$. **D.** Bifurcació *flip* supercrítica.

2.5 Crisis

Les bifurcacions estudiades en la secció anterior descriuen canvis en els atractors regulars (punts fixos, cicles límit) de les aplicacions discretes. Els atractors caòtics també poden sofrir canvis abruptes sota la variació d'un paràmetre. En aquest cas es parla de *crisi* [18, 19] i no de bifurcació. A continuació es descriuen els fenòmens de crisi més habituals [20, 21, 22].

Crisi de frontera (*Boundary crisis*)

Aquest tipus de crisi es produeix quan un atractor caòtic toca o creua les fronteres de la seua conca d'atracció que la separen de la conca d'un altre atractor. Açò es tradueix en la desaparició (o aparició sobtada) de l'atractor caòtic. L'aplicació logística sofreix una crisi d'aquest tipus en $r = 4$, quan l'atractor caòtic toca els límits de l'interval unitat. Per a $r > 4$ l'atractor caòtic desapareix i totes les condicions inicials tenen com atractor $-\infty$ (veure figura 2.5).

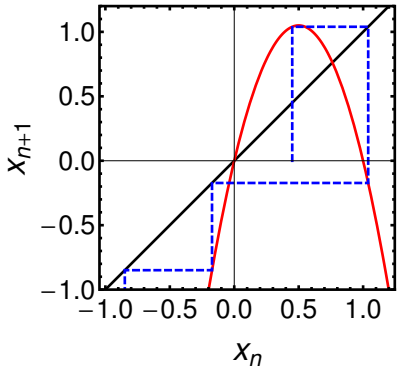

Figura 2.5 Diagrama *cobweb* de l'aplicació logistica amb $r = 4.2$. S'observa com la condició inicial $x_0 = 0.45$ té com atractor $-\infty$. En $r = 4$ es produeix una crisi de frontera i l'atractor caòtic existent per a $r \lesssim 4$ desapareix. Per a $r > 4$, totes les condicions inicials tenen com atractor $x = -\infty$.

Crisi interior

En aquest cas un punt fix - o cicle límit - inestable existent dins la conca d'atracció d'un atractor caòtic col·lideix amb aquest per a un cert valor del paràmetre. Açò produeix un augment sobtat del tamany de l'atractor. A la dreta de la finestra de període-3 de la aplicació logística ens trobem aquest fenomen com es pot veure a la figura 2.6.

Crisi de fusió de l'atractor (*Attractor merging crisis*)

Com indica el seu nom, en aquesta crisi dos atractors caòtics amb conques d'atracció distintes es fonen en un sol atractor. L'aplicació logística no ofereix cap exemple d'aquest tipus de crisi però sí ho fa una lleugera variació anomenada aplicació logística antisimètrica

$$f(x,r) = rx(1-|x|). \tag{2.23}$$

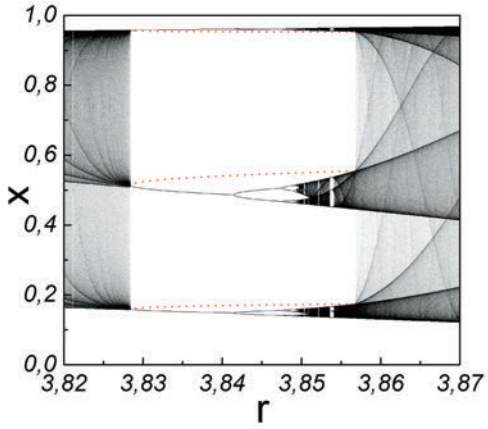

Figura 2.6 Ampliació de la finestra de període 3 en el diagrama de bifurcació de l'aplicació logística. S'han representat els punts fixos inestables amb línies discontínues. La finestra comença amb una bifurcació tangent de $f^3(x)$ i acaba quan els punts fixos inestables creats en la bifurcació col·lideixen amb l'atractor caòtic, en un clar exemple de crisi interior.

Aquesta presenta una crisi de fusió de l'atractor en $r = 4$ com s'observa a la figura 2.7. Cal no confondre aquesta crisi amb la coalescència de les dos peces de l'atractor caòtic de la logística en una sola peça en $r \approx 3.67$.

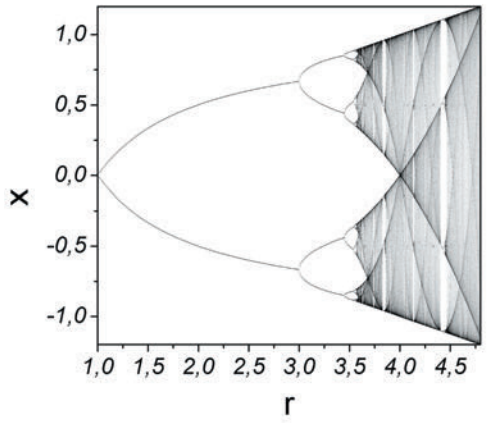

Figura 2.7 Diagrama de bifurcació de l'aplicació logística antisimètrica (2.23). S'aprecia la fusió del dos atractors caòtics en $r = 4$.

2.6 Fenòmens d'intermitència

Un altre fenomen interessant relacionat amb les bifurcacions i les crisis és l'anomenada intermitència. Es tracta de l'aparició *intermitent* en òrbites caòtiques d'intervals durant els quals la dinàmica sembla regular (anomenat de vegades règim *laminar*). Aquest fenomen es presenta generalment per a valors dels paràmetres propers a una bifurcació o crisi. Açò és fàcil d'entendre i ho vorem més avall amb un exemple en el cas de l'aplicació logística.

Imaginem una aplicació que per a un valor del paràmetre $\lambda = \lambda_c$ sofreix una crisi o bifurcació de manera que per a $\lambda < \lambda_c$ la dinàmica és regular mentre que si $\lambda > \lambda_c$ la dinàmica és caòtica. Si definim τ com la durada promedi dels intervals laminars, se satisfà [22]

$$\lim_{\lambda \to \lambda_c^+} \tau = \infty. \tag{2.24}$$

És a dir, els intervals laminars són cada vegada més llargs a mesura que ens apropem al valor crític del paràmetre.

La intermitència fou descrita per primera vegada per Yves Pomeau i Paul Manneville [23]. En l'article original es distingeixen tres tipus d'intermitència associats a diferents tipus de bifurcació. A més a més, τ escala prop de λ_c de manera distinta segons el tipus d'intermitència. La classificació és la següent

- Tipus I: associada a bifurcacions tangents

$$\tau \sim (\lambda - \lambda_c)^{-\frac{1}{2}}. \tag{2.25}$$

- Tipus II: associada a bifurcacions Hopf (Neimark-Sacker)

$$\tau \sim (\lambda - \lambda_c)^{-1}. \tag{2.26}$$

- Tipus III: associada a bifurcacions de duplicació de període inverses

$$\tau \sim (\lambda - \lambda_c)^{-1}. \tag{2.27}$$

Per tal d'il·lustrar millor aquests conceptes estudiarem un cas d'intermitència de Tipus I que trobem en l'aplicació logística abans de la finestra de període 3. Com ja hem vist, aquesta finestra comença amb una bifurcació tangent de la iterada tercera de l'aplicació en $r_c = 1 + \sqrt{8}$. Quan $r \lesssim r_c$ la dinàmica és caòtica. No obstant, com es pot observar en la figura 2.8, les trajectòries presenten segments semblants a una dinàmica de període 3 que són més llargs quan més a prop ens trobem de r_c. El diagrama *cobweb* de la figura 2.9 ens permet entendre a què es deu aquest fenomen. Com ja hem vist, l'òrbita de període 3 es crea a través de tres bifurcacions tangents de la iterada tercera en $r = r_c$. Prop d'aquest valor del paràmetre el mapa ja està molt prop de la bisectriu $x_{n+1} = x_n$ i l'òrbita pot romandre en aquestes regions durant successives iteracions produint les regions laminars d'aparent regularitat.

2.7 Aplicacions definides a trossos i *Border-collision Bifurcations*

Fins el moment hem discutit els principals fenòmens que es presenten en la dinàmica de sistemes discrets definits per aplicacions contínues i diferenciables com l'aplicació logística. No obstant, existeixen altres exemples paradigmàtics de sistemes dinàmics discrets definits per funcions discontínues o no diferenciables en algun punt de l'interval de definició. De fet, aquest tipus de sistemes s'empren en un gran nombre de problemes com ara la modelització de sistemes mecànics amb fricció o col·lisions, o també en la dinàmica de certs circuits electrònics [24, 25, 26].

Aquests sistemes presenten nous fenòmens dinàmics que s'engloben dins el nom genèric de bifurcacions induïdes per la discontinuïtat o en anglés, *Discontinuity-induced bifurcations* [24]. Potser el fenomen més estudiat és el de les *Border-Collision bifur-*

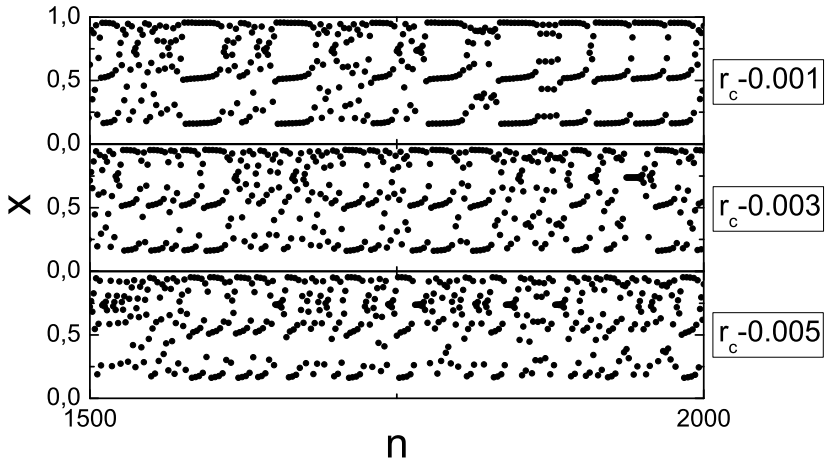

Figura 2.8 Fenomen d'intermitència en l'aplicació logística. Es mostren tres òrbites per a tres valors distints del paràmetre de bifurcació prop del valor $r_c = 1+\sqrt{8}$ on comença la finestra de període 3. S'aprecien clarament els intervals laminars quan la dinàmica sembla de període 3. Aquests intervals són cada vegada més llargs a mesura que ens aproximem a r_c.

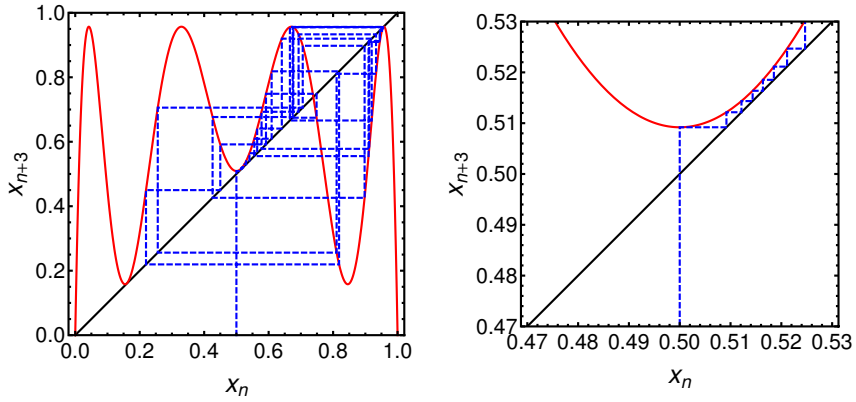

Figura 2.9 Diagrama *cobweb* il·lustrant el fenomen d'intermitència en l'aplicació logística. S'ha representat la iterada tercera $f^3(x)$ per a $r = r_c - 0.001$.

cations, un conjunt de bifurcacions que es produeixen quan un punt fix de l'aplicació col·lideix amb una discontinuïtat de l'aplicació o de la seua derivada [27, 28, 29, 30].

Un exemple d'aquest tipus de sistema és l'anomenat *skew tent map* $x_{n+1} = S(x_n)$ on $S(x)$ ve donada per

$$S(x) = \begin{cases} \frac{1}{2}x + \rho, & x \leq 0 \\ -\lambda x + \rho, & x > 0 \end{cases} \tag{2.28}$$

A la figura 2.10 podem observar un diagrama de bifurcació d'aquest sistema. Igual que en el cas de l'aplicació logística, aquest sistema presenta tant dinàmiques regulars (atractors periòdics) com caòtiques. No obstant, en aquest cas el diagrama és qualitativament distint donat que no trobem una cascada de duplicació de període i les transicions

ordre-caos són abruptes. Com hem vist abans, en el cas de l'aplicació logística les òrbites periòdiques dupliquen el seu període a mesura que augmenta el valor del paràmetre en procés límit fins arribar a la frontera del caos ($r_n \to r_\infty$). En el *skew tent map*, pel contrari, podem passar directament (sense cap procés límit) d'una òrbita periòdica de període finit a una òrbita caòtica (observar els valors $\lambda = 2, 4, 8, \ldots$ en la figura 2.10). Aquesta nova fenomenologia està causada per la no diferenciabilitat de l'aplicació en $x = 0$ i en concret, per l'aparició de bifurcacions de tipus *Border-Collision*.

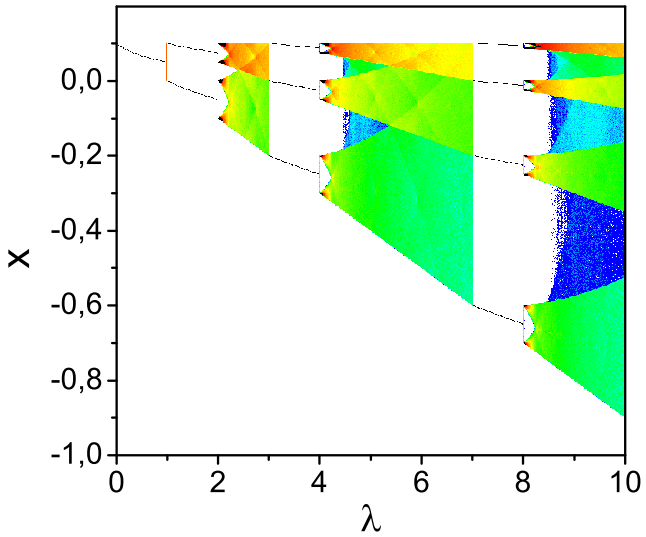

Figura 2.10 Diagrama de bifurcació del *skew tent map* $x_{n+1} = S(x_n)$ en funció del paràmetre λ ($\rho = 0.1$).

En aquesta primera part de la tesi estudiarem un nou fenomen de bifurcació que apareix en aplicacions definides a trossos i que ha romàs desatès en la literatura. Es tracta d'unes transicions abruptes, en les quals es passa d'un atractor periòdic a un altre de període diferent o a un atractor caòtic, amb una particularitat: en el punt de la bifurcació existeix un tercer atractor format per infinits cicles límit que, en el cas més general, poden ser de diferent període. En concret, estudiarem una aplicació unidimensional proposada originàriament com un model de dinàmica de poblacions i l'aplicació de Lozi, que defineix un sistema dinàmic discret bidimensional molt conegut i amb propietats interessants. En ambdós casos descriurem la dinàmica i estudiarem aquest nou fenomen de bifurcació que hem anomenat *Bisecting bifurcation.* Entre altres coses, donarem una explicació geomètrica del fenomen i veurem com aquest tipus de bifurcacions són un cas particular de bifurcació *Border-collision* que no es contempla dins les classificacions actuals d'aquest tipus de bifurcació.

Chapter 3
A one-dimensional case study: The Varley-Gradwell-Hassell map

3.1 Introduction

As we have seen in the introduction to this first part of the thesis, work on population ecology carried out in the 1970's helped chaos to move center stage as a new interdisciplinary subject [11]. One-dimensional discrete-time population models are technically among the simplest ones to consider and interpret. They provide an appropriate description of species with non-overlapping generations. The basic example for the evolution of a population density $X_n \in \mathbb{R}$ at generation n is the linear law $X_{n+1} = rX_n$. Here r represents the growth rate or fecundity, assumed constant. This is, however, too schematic allowing only extinction ($r < 1$), equilibrium ($r = 1$) or infinite growth ($r > 1$). It was soon recognized that more realistic models should be nonlinear:

$$X_{n+1} = X_n F(X_n). \tag{3.1}$$

Written in this form, F is the dimensionless non-constant fitness function of the population or per-capita growth rate. A sage choice for it should capture the essential features of the system. The crucial point is that once nonlinearity is let in, a huge variety of new phenomena may appear as is now universally recognized. The particular choice [31, 32, 33]

$$F(X_n) = r(X_n/K)^{-b},\ b > 0, \tag{3.2}$$

renders easy the numerical determination of the parameter values from experimental population data by a linear fit to $\log X_{n+1}$ versus $\log X_n$, which constitutes certainly a salient advantage. In (3.2) the presence of parameter K, the conventional carrying capacity, ensures the dimensionless character of F. A slight variant of it reads [33, 32]

$$F(X_n) = \begin{cases} r, & X_n \leq C \\ r(X_n/K)^{-b}, & X_n > C \end{cases} \tag{3.3}$$

where C is a threshold population density and the fitness parameter $b > 0$ is dimensionless.

This particular model was introduced by Varley, Gradwell and Hassell [32, 33] to study density-dependent population growth in a limited environment. Experimental evidence [32] suggested the existence of a critical population density beyond which intraspecific competition mechanisms increased mortality and limited growth. We will refer to this model as the Varley-Gradwell-Hassell map. We want to emphasize that these and similar models can also be used as mathematical instances of dynamical systems to illustrate different features when the ranges of parameters and time variable are enlarged

beyond those realistic in population dynamics. In this spirit, we analyze here the one-dimensional discrete model associated with equation (3.3) which will be referred to as the Varley-Gradwell-Hassell map (or simply VGH map) [34]. In [35] it is briefly explained that the system is chaotic for $b > 2$ and regular for $b < 2$, pointing out that in the order-to-chaos transition no cascade of period doubling emerges. In this chapter we analyze numerically and analytically how such a transition takes place what, to the best of our knowledge, has not been studied in detail in the mathematics or ecology literature.

3.2 Description of the map and its dynamics

3.2.1 Alternative formulations

We write the VGH map, equation (3.3), in the form

$$x_{n+1} = f(x_n; b, c, r), \tag{3.4}$$

with

$$f(x; b, c, r) = \begin{cases} rx, & x \leq c\,, \\ rx^{1-b}, & x > c. \end{cases} \tag{3.5}$$

In going from (3.1) and (3.3) to (3.4) and (3.5) we have used the carrying capacity K as our natural unit to measure population densities and correspondingly introduced the dimensionless variable $x_n = X_n/K$, and parameter $c = C/K$.

The function f in (3.5) is defined in $\mathbb{R}^4$ but we take $x \in [0, \infty)$ because x, although dimensionless, stands for a population density. In the three dimensional parameter space (b, c, r) we consider only the region $b > 1$ to ensure decrease of f with increasing x and $c, r > 0$ for compatibility with the range of definition of x.

According to this map the population density in a given generation is a linear function of that in the previous one as far as it does not exceed a critical value c. For greater values the population follows a nonlinear power-law. Fig. 3.1 shows the map for different values of c. We expect differences in the response of the system according to whether the value of c is below or above unity. For some purposes, we have found it useful to express the

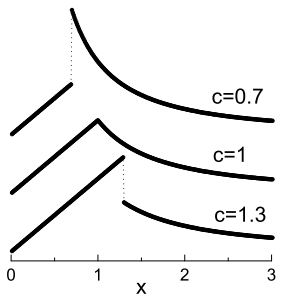

Fig. 3.1 Shape of the map (3.5) for $b = 2.5$, $r = 2$ and three different values $c = 0.7, 1, 1.3$. The curves have been vertically shifted for the sake of clarity.

VGH map in terms of the new variable z and the new parameter ξ

$$z \equiv 2\log(x)/\log(r), \quad \xi \equiv 2\log(c)/\log(r), \tag{3.6}$$

with $x \neq 0$ and $r > 1$. The numeric factor two in (3.6) has been introduced for convenience. The inverse transformation reads

$$x = r^{z/2}, \quad c = r^{\xi/2}. \tag{3.7}$$

This leads from (3.5) to

$$z_{n+1} = \begin{cases} z_n + 2, & z_n \leq \xi, \\ (1-b)z_n + 2, & z_n > \xi, \end{cases} \tag{3.8}$$

now with phase space $z \in (-\infty, \infty)$. This representation of the map has only two parameters. From a mathematical point of view this transformed version is piecewise linear, whereas (3.5) defines a piecewise continuous nonlinear system. Linearization is a standard procedure in the study of dynamical systems. It usually follows from first order approximations. Here, however, the linearization is exact. It is worth mentioning that dynamical systems of the same type can be found in applications in electronics, robotics and mechanical systems with impacts [26, 36].

3.2.2 Lyapunov exponent

The Lyapunov exponent is a measure of the rate at which two initially close trajectories move away. For the one-dimensional discrete map $x_{n+1} = f(x_n)$ the computation of the Lyapunov exponent λ admits an analytical formula (see for instance [8, 21, 22, 37])

$$\lambda = \lim_{n\to\infty} \left\{ \frac{1}{n} \sum_{k=0}^{n-1} \ln |f'(x_k)| \right\}, \tag{3.9}$$

which, in the case (3.5), leads to

$$\lambda = \ln r + \lim_{n\to\infty} \left\{ \frac{1}{n} \sum_{k=0}^{n-1} [\ln|1-b| - b\ln|x_k|]\theta(x_k - c) \right\}, \tag{3.10}$$

whereas (3.8) yields

$$\lambda = \ln|1-b| \lim_{n\to\infty} \left\{ \frac{1}{n} \sum_{k=0}^{n-1} \theta(z_k - \xi) \right\}. \tag{3.11}$$

Both formulas are given in terms of Heaviside θ function which selects the iterations that visit $x_n > c$ or $z_n > \xi$ respectively. Therefore, the interpretation of the Lyapunov exponent in this system is particularly straightforward: λ is ruled by the proportion of exterior points in the trajectories, namely those with $x_n > c$ or $z_n > \xi$.

The mathematical equivalence of the two expressions for λ in (3.10) and (3.11) yields the following result for the statistics of points $x_k > c$ in the attractor

$$\lim_{n\to\infty} \left[\frac{1}{n} \sum_{k=0}^{n-1} \ln(x_k)\theta(x_k - c) \right] = \frac{\ln r}{b} \tag{3.12}$$

meaning that the geometric mean of all the points $x_k > c$ in the trajectory equals the value $r^{1/b}$. A simpler version of (3.10) reads now

$$\lambda = \ln|1-b| \lim_{n\to\infty} \left\{ \frac{1}{n} \sum_{k=0}^{n-1} \theta(x_k - c) \right\}. \tag{3.13}$$

Equation (3.9) makes use of the derivative f' which in the present case is not defined at $x = c$ or $z = \xi$. However, as it is an isolated point, it does not cause any numerical difficulty.

In practice, one has to take care of discarding transients in order to allow the orbit to enter the attractor. In particular, transients are very long for chaotic trajectories when $b \approx 2$. Besides, it is convenient to average λ over a large number of initial seeds.

Since the summation in (3.10) and (3.11) is over a large enough number of points on the trajectory, numerical accuracy is a relevant issue. To this end, and following the analysis in [38], we have used the multi-precision Fortran package MPFUN [39, 40] which allows us to efficiently compute with a very high number of digits. We concluded that double precision gives here enough computational guaranties as regards the calculation of (3.10) and (3.11). By contrast, it is not the case for the computation of trajectories of (3.8) for some integer values of $b > 2$, an issue that we deal with in Section 3.5.5.

3.2.3 Fixed points of the VGH map

For $r < 1$, $x = 0$ is always a stable fixed point. When $c < r^{1/b}$ there is a second fixed point at $x = r^{1/b}$ which is stable if $1 < b < 2$ and attracts any initial condition in the interval (c, x^*) with $x^* = (c/r)^{1/(1-b)}$. For $b = 2$, that interval consists of period-2 points, with the exception of the fixed point $\sqrt{r}$. Values $x \le c$ and $x > x^*$ go to $x = 0$. Observe that here $r < 1$ does not necessarily imply extinction, as would be the case in the logistic map. This is due to the interplay between the different parameters.

For $r = 1$ any initial condition in $[0, c]$ remains fixed. If $c < 1$, then $x = 1$ is also fixed. It is stable for $1 < b < 2$ attracting any initial condition in the interval (c, x^*) with $x^* = c^{1/(1-b)}$. If $b = 2$, the interior points of that interval, except $x = 1$, are paired in 2-cycles. Points to the right of x^* are eventually fixed, reaching its limiting fixed value in two steps.

For $r > 1$, $x = 0$ is an unstable fixed point, independently of c. If $c < r^{1/b}$, also $x = r^{1/b}$ is fixed, although it is stable only for $1 < b < 2$.

In the rest of the paper we consider only $r > 1$ which, as we shall see, generates a much richer behavior.

3.3 Dependence on b: order-to-chaos transition

As already stated in [35], the chaotic regime corresponds to $b > 2$, independently of the values of c and r, without stable regularity windows embedded. This is clear from the positive character of λ in (3.13) when $b > 2$. The behaviour of the system with respect to b is illustrated by the bifurcation diagrams in Fig. 3.2. The three panels correspond to $c = 0.8, 1, 1.2$, from top to bottom, respectively, with the fixed value $r = 2$. In Fig. 3.3 we plot the bifurcation diagram for $c = 2.5$ and $r = 2$, as well as the Lyapunov exponent

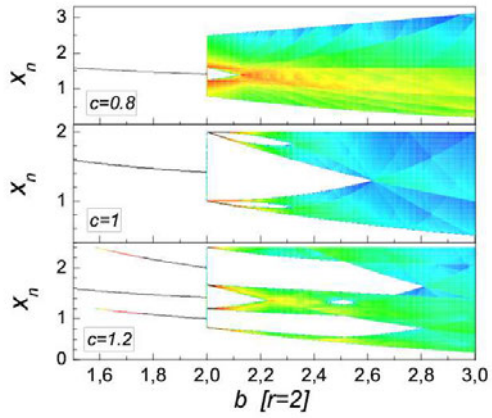

Fig. 3.2 Bifurcation diagrams as a function of b, for $r = 2$ and three different values of c. The color scale is logarithmic and it stands for the frequency the point is visited with. This holds for the rest of color figures, unless otherwise stated.

λ (upper panel). Notice the irregularities in the curve around the value $b = 2.2$ where the bifurcation diagram exhibits a number of band merging crises [19, 22]. The afore-

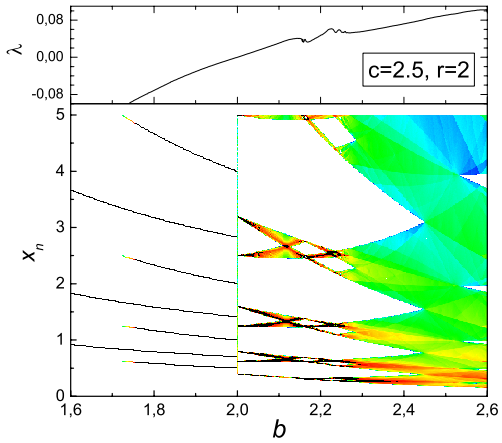

Fig. 3.3 Bifurcation diagram as a function of b, for $r = 2,\ c = 2.5$. The corresponding Lyapunov exponent is in the upper panel.

mentioned sudden transition from a regular to a chaotic system, with no period doubling, is apparent. As the negative sign of the computed Lyapunov exponent witnesses, $b < 2$ means regular behavior: every initial seed ends up in a periodic orbit. For fixed $b < 2$, the attractor consists of coexisting limit cycles. Its cardinal, i.e. the number of attracting points in the diagram - with no regard to the limit cycles they belong to -, is a piecewise constant function of c. In other words, there exist some values $c = c_n$ ($n \geq 1$ integer) where this cardinal number changes abruptly. The cardinal is given by the heuristic formula $2(n+1)/[3-(-1)^n]$, $(n \geq 1)$, whose first few terms read

$$1,3,2,5,3,7,4,9,5,11,6,13,7,15,8,17,9,\ldots \tag{3.14}$$

These can be interpreted as forming two intermingled sequences whose terms increase by one and two units respectively. As can be seen in Fig. 3.4 for $b = 1.9$ and $r = 2$, for small c only a fixed point exist but as c increases limit cycles of periods $2,3,4,\ldots,n$

progressively appear. Every two consecutive limit cycles coexist for a certain interval of c, giving rise to sequence (3.14). A detailed description of the attractors and basins of

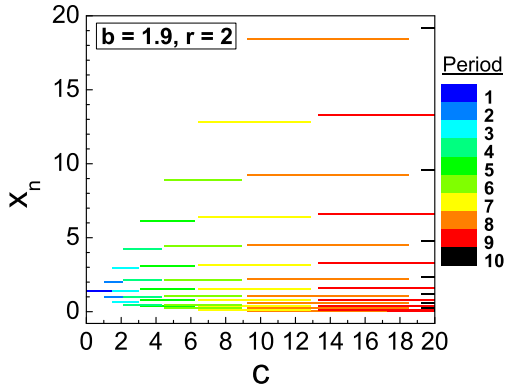

Fig. 3.4 Regular orbits. Bifurcation diagram as a function of c, with $b = 1.9$ and $r = 2$. The period of cycles is coded by the color scale (gray tone).

attraction at $b = 2$ is presented in Section 3.4.

For $b = 2$ and fixed $r > 1$ the orbit of an arbitrary initial condition $x_0 \in [0, \infty)$, is simple enough to be rigorously described. As detailed below, the general characteristic in this case is that all the initial conditions are fixed, periodic or eventually periodic. There exist an infinity of coexisting limit cycles. Their periods are allowed to take only a restricted set of values, which depend on the initial condition and parameters value through very strict laws. We defer their detailed description to Section 3.4. The reader can find there precise information about the transients length and exact account of the cycles. Here we report only the most salient features in terms of the variable x and threshold parameter c.

If $c \leq 1$, then the closed interval $[c, r/c]$ is invariant under the action of the map. Any interior point $x_0 \neq \sqrt{r}$ belongs to the $2-$cycle $\{x_0, r/x_0\}$. $x_0 = \sqrt{r}$ is a fixed point. The extremes $x_0 = c$ and $x_0 = r/c$ as well as all the exterior points are eventually periodic, entering the invariant interval after a transient.

If $c > 1$, then the closed interval $[1/c, rc]$ is invariant under the action of the map. Every exterior point is eventually periodic. Interior points are periodic. For fixed c, the period of the cycles depends on x_0 but can take on only a restricted set of values. For instance, with $c = 2$ one finds a $3-$cycle: $\{1/\sqrt{r}, \sqrt{r}, r\sqrt{r}\}$; a $4-$cycle: $\{1/r, 1, r, r^2\}$; and the rest of the points in the interval accommodates in an infinity of $6-$cycles. All these cycles are the limit cycles for the eventually periodic points. Notice that in this system the existence of period three does not imply chaos. This is not in conflict with the celebrated Li and Yorke theorem because the VGH map is defined by a discontinuous function.

The basins of attraction of such limit cycles are infinite intermingled sets of zero measure made of equidistant points in the z variable (a detailed study is provided in Section 3.4). The vertical segments located at $b = 2$ in Fig. 3.2 and 3.3 comprise all the coexisting limit cycles. In numerical simulations such a vertical segment gets filled only if enough initial conditions are used in the construction of the bifurcation diagram.

We have called this type of bifurcations mediated by infinite sets of neutrally stable limit cycle *bisecting bifurcations*. We justify this choice in the following section.

3.3.1 An explanation of the origin of the observed bifurcation

Next we develop a geometric explanation for the emergence of a bisecting bifurcation based on the cobweb diagram of a general one-dimensional piecewise defined map $f(x;p)$ with parameter p. Notice that an infinite set of regular trajectories of period n will be observed for a critical value p_c of the parameter when the nth iterate of the map f^n has a piece which is co-linear with the bisectrix. Hence, the name we are using for these bifurcations. More explicitly, at the bifurcation, f^n will be of the form

$$f^n(x;p_c) = \begin{cases} \cdots, \cdots, \\ x, \quad x \in (x_l, x_r), \\ \cdots, \cdots \end{cases} \tag{3.15}$$

An explicit instance of this phenomenon in the VGH map is given by its second iterate which reads

$$f^2(x) = \begin{cases} r^2 x, & x \le \frac{c}{r}, \\ r^{2-b}x^{1-b}, & \frac{c}{r} < x \le c, \\ r^{2-b}x^{(1-b)^2}, & c < x \le (\frac{r}{c})^{\frac{1}{b-1}}, \\ r^2 x^{1-b}, & x > c, x > (\frac{r}{c})^{\frac{1}{b-1}}. \end{cases} \tag{3.16}$$

When $b = 2$ the third piece becomes x and we find a bisecting bifurcation mediated by

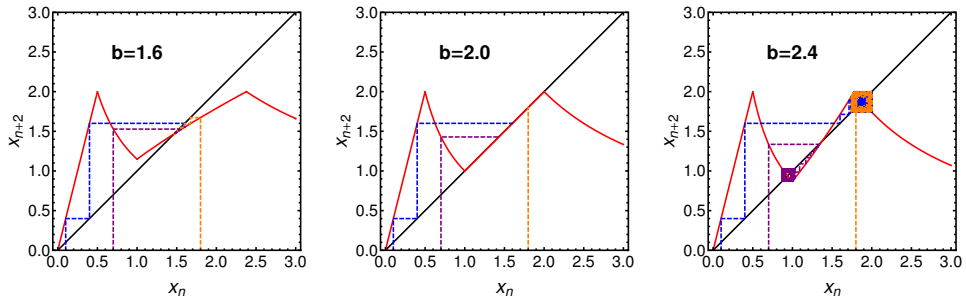

Fig. 3.5 A sequence of three cobweb plots of $f^2(x)$ illustrating the bisecting bifurcation from order to chaos at $b = 2$ ($c = 1, r = 2$).When $b = 1.6$ the map present a stable fixed point. When $b = 2$ the third piece of the map becomes x, producing an infinite set of fixed points of $f^2(x)$ (period-2 orbits of $f(x)$). When $b = 2.4$ the map presents two unstable fixed points and the dynamics is chaotic. Looking the three cases shown in decreasing order of b we can see how these two unstable fixed points collide with the borders of the map at $b = 2$.

an infinite set of neutrally stable period-2 limit cycles provided $c < \sqrt{r}$. This is illustrated in Fig. 3.5 where three cobweb plots of $f^2(x)$ for values $b = 1.6, 2.0, 2.4$ and $c = 1$ are shown. In the three cases the same three initial conditions have been evaluated. When $b = 1.6$, all trajectories converge to the stable fixed point. In the critical case, when $b = 2$, each initial condition evolves to a different neutrally stable fixed point of $f^2(x)$. For $b = 2.4$ the trajectories are chaotic.

In principle, several iterates of f can have pieces co-linear with the bisectrix simultaneously for the same value of p_c. In such cases, infinite sets of cycles of different periods will coexist when $p = p_c$. This is the case for the VGH map. When $b = 2$ and $c > 1$ the neutrally stable limit cycles can show different periods. This is illustrated in Fig. 3.6 where the evolution in the cobweb diagram and the trajectories of two different

initial conditions are shown for $b = 2$, $r = 4$ and $c = \sqrt{2}$. One of the trajectories enters a period-2 limit cycle while the other evolves to a period-4 limit cycle. The distribution of the limit cycles of different periods in phase space is detailed in the next section.

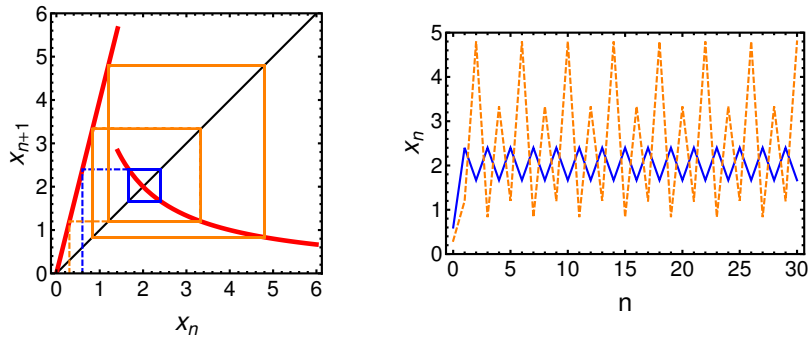

Fig. 3.6 Cobweb diagram (left panel) and trajectories (right panel) of $V(x)$ for $b = 2$, $c = \sqrt{2}$, $r = 4$ and two different initial conditions ($x_0 = 0.3, 0.6$). We illustrate here how two different initial conditions enter neutrally stable limit cycles of different periods when $b = 2$. The initial condition $x_0 = 0.3$ enters a period-4 orbit while the initial condition $x_0 = 0.6$ leads to a period-2 orbit.

3.3.2 Algebraic identification of bisecting bifurcations

In this section we prove that for the VGH map the bisecting bifurcation takes place only at $b = 2$. The linearized version (3.8) allows the following algebraic approach. In this linear form, the elements $\{z_1, z_2, \ldots, z_T\}$ of a cycle of period T satisfy

$$z_n = \begin{cases} z_{n-1} + 2, & z_{n-1} \le \xi, \\ (1-b)z_{n-1} + 2 & z_{n-1} > \xi, \end{cases} \quad n = 2, \ldots, T,$$
$$z_1 = \begin{cases} z_T + 2, & z_T \le \xi, \\ (1-b)z_T + 2, & z_T > \xi. \end{cases} \tag{3.17}$$

These expressions can be written in the form

$$\begin{aligned} z_1 + \alpha_T z_T &= 2, \\ z_n + \alpha_{n-1} z_{n-1} &= 2, \quad n = 2, 3, \ldots, T, \end{aligned} \tag{3.18}$$

with coefficients

$$\alpha_k = \begin{cases} -1, & z_k \le \xi, \\ (b-1), & z_k > \xi. \end{cases} \tag{3.19}$$

The linear system of equations (3.18) can be expressed in matrix form

$$\sum_{j=1}^{T} A_{ij} z_j = 2, \quad i = 1, 2, \ldots, T, \tag{3.20}$$

where the matrix A is

$$A = \begin{pmatrix} \alpha_1 & 1 & 0 & \dots & \dots & 0 \\ 0 & \alpha_2 & 1 & 0 & \dots & 0 \\ 0 & 0 & \alpha_3 & 1 & \dots & 0 \\ \dots & \dots & \dots & \dots & \dots & \dots \\ 0 & 0 & \dots & \dots & \alpha_{T-1} & 1 \\ 1 & 0 & \dots & \dots & 0 & \alpha_T \end{pmatrix}.$$

In order to find an attractor consisting of infinitely many limit cycles of period T we need the system of equations (3.18) to be compatible and indeterminate. A necessary condition is therefore $\det(A) = 0$. The determinant of the matrix A is

$$\det(A) = \prod_{k=1}^{T} \alpha_k + (-1)^{T+1}. \tag{3.21}$$

If the cycle has d of its elements satisfying $z_i > \xi$ this gives

$$\det(A) = (-1)^{T-d}(b-1)^d + (-1)^{T+1}, \tag{3.22}$$

which vanishes for $b = 0$ and, if d is even, also for $b = 2$. Since we are only interested in $b > 1$, the only possible solution is then $b = 2$. This is precisely the value found numerically from the bifurcation diagrams. It is important to notice that this value of b and equation (3.8) imply neutral stability for any possible cycle. Of course, the argument in this section does not complete the analysis of the vertical segment in those diagrams. It only excludes any other value of b as candidate.

3.3.3 Harter's boundaries ($x_0 = c$) at $b = 2$

It is well known that, for a continuous unimodal uniparametric map with its maximum at $x = x^*$, the plot of the successive iterates of the initial seed $x_0 = x^*$ versus the map parameter generates the so-called Harter boundaries [41, 42]. In the logistic map [11, 12, 13, 37] these correspond to the sharp cusps observed in the invariant density. Harter lines cross at unstable equilibrium points and, in the case of the logistic map, the set of crossing points follows itself a reversed bifurcation cascade.

The VGH map is not differentiable at $x = c$, although it is still unimodal in the sense of being monotonically increasing for $x \leq c$ and decreasing for $x > c$. A similar study to the one described for the logistic map leads to interesting results. To be precise, Harter lines correspond to the color boundaries visible in Figures 3.2 and 3.3. They can be directly established from the form (3.5) of the map. For $b = 2$, the seed $x_0 = c$ ends up in a cycle whose period $P(r,c)$ depends on r and c. The expression for P and the cycle elements may be explicitly written down.

For $c < 1$ the 2-cycle $\{rc, 1/c\}$ is reached just after one iteration. For $c \geq 1$, $x = c$ is always a periodic point. Obviously $c = 1$ belongs to the 2-cycle $\{1, r\}$. When $c > 1$ there is a unique integer $M \in \mathbb{N}$ such that

$$c \in \left[r^{M/2}, r^{(M+1)/2} \right). \tag{3.23}$$

with

$$M = \left\lfloor 2\frac{\log c}{\log r} \right\rfloor = \lfloor \xi \rfloor \tag{3.24}$$

in terms of the integer part or floor function. Then, for $c > 1$ we get two cases

$$P(r,c) = M+2, \text{ if } c = r^{M/2} \tag{3.25}$$

$$P(r,c) = 2(M+2), \text{ if } c \in \left(r^{M/2}, r^{(M+1)/2}\right) \tag{3.26}$$

The $2(M+2)$-points of the cycle for the case (3.26) read

$$\left\{\frac{c}{r^M}, \frac{c}{r^{M-1}}, \ldots, \frac{c}{r}, c, rc, \frac{1}{c}, \frac{r}{c}, \frac{r^2}{c}, \frac{r^{M+1}}{c}\right\} \tag{3.27}$$

which in turn, for $c = r^{M/2}$ (*i.e.*, case (3.25)) contract to the $(M+2)$-points cycle

$$\left\{r^{-M/2}, r^{-M/2+1}, \ldots, r^{M/2-1}, r^{M/2}, r^{M/2+1}\right\} \tag{3.28}$$

It is interesting to observe that (3.27) can be obtained recurrently from $\{rc, 1/c\}$ by a simple procedure. In going from M to $M+1$ two new elements are added to the cycle: the one in the leftmost position is obtained by dividing by r the first element in the previous cycle. The other, which goes at the rightmost position, is obtained by multiplying by r the last element of the previous cycle.

3.4 Attractors and basins of attraction when $b = 2$

In this Section we study in depth the structure of the attracting segment of the VGH system at the critical point $b = 2$. To facilitate the analysis we express the VGH map for $b = 2$ in terms of the new variable $w \equiv z - 1$ as

$$W(w) = \begin{cases} w+2, & w \leq \xi - 1, \\ -w, & w > \xi - 1. \end{cases}$$

One advantage of this form is that the segment of limit cycles, $\mathscr{A} \equiv [-|\xi| - 1, |\xi| + 1]$, is symmetric in phase space with respect to $w = 0$.

3.4.1 Structure of the attractor

We start our study by distinguishing the cases of positive and negative ξ.

3.4.1.1 $\xi \leq 0$

This case presents the simplest dynamics. The segment $\mathscr{A}$ is composed of infinite period-2 limit cycles around $w = 0$, which is a fixed point.

3.4.1.2 $\xi > 0$

The dynamics is more complicated for positive ξ. All integer initial conditions $w_0 \in \mathbb{Z}$ lead to limit cycles with integer elements. In particular, if the initial condition is even (resp. odd), the final limit cycle will have as its elements all even (resp. odd) integers

inside the segment $\mathscr{A}$. The periods of these cycles, which depend on ξ, are detailed in Table 3.1. If $w_0 \notin \mathbb{Z}$ we need to study the cases $\xi \in \mathbb{N}$ and $\xi \notin \mathbb{N}$ separately:

- $\xi \notin \mathbb{N}$
  For positive non-integer ξ we have two infinite sets of limit cycles of periods $T = 2(n+1)$ and $T = 2(n+2)$ with $n = \lfloor \xi \rfloor$ (where $\lfloor \cdot \rfloor$ stands for the floor function). These cycles spread over $\mathscr{A}$ in a rather peculiar way. To make it clear we find useful to consider the finite set of points

$$\mathscr{B} = \mathscr{A} \bigcap \{w = (-1)^{\alpha}\xi + (-1)^{\beta}(2k+1), \quad k = 0 \ldots n, \quad \alpha, \beta = 0, 1\} \tag{3.29}$$

  whose elements, when written in increasing order, we denote by w^i, $i = 1, 2, \ldots$. Then, $\mathscr{B}$ punctuates a partition of the interval $\mathscr{A}$ in subintervals. Points in the same subinterval belong to cycles with the same period. Points in contiguous subintervals belong to cycles with different period.
  For instance, if $0 < \xi < 1$ then $n = 0$ and the frontiers of the subintervals are given by

$$\mathscr{B} = \{w^1, w^2, w^3, w^4\} = \{-\xi - 1, \xi - 1, -\xi + 1, \xi + 1\}. \tag{3.30}$$

  Thus, in this case three subintervals exist inside the attractor. In Table 3.1 we have detailed the period of the limit cycle for initial conditions inside the attracting segment $\mathscr{A}$.
- $\xi \in \mathbb{N}$
  When ξ is a natural number every limit cycles has period $T = 2(\xi + 1)$.

All this information is contained in Fig. 3.7 where we have plotted the structure of the attracting segment at $b = 2$ as a function of ξ with $\xi \in [-1, 3]$. The different tones of gray stand for different periods. As an example, a particular $\xi^* < 1$ has been chosen to illustrate the position of the frontiers given in (3.30). The discontinuous horizontal lines stand for cycles with initial conditions $w_0 \in \mathbb{Z}$.

Table 3.1 Period of the trajectories according to the initial point $w_0 \in [-|\xi| - 1, |\xi| + 1]$, with $b = 2$ and $\xi > 0$ ($\xi \notin \mathbb{N}$). The description of the case $w_0 \in \mathbb{Z}$ is also valid for $\xi \in \mathbb{N}$.

Initial point		Period	Condition
$w_0 \in (w^i, w^{i+1})$ and $w_0 \notin \mathbb{Z}$		$2(n+1)$	even i
		$2(n+2)$	odd i
$w_0 = w^i$ and $w_0 \notin \mathbb{Z}$		$2(n+2)$	$\forall i$
$w_0 \in \mathbb{Z}$	$N = \lfloor (\xi+1)/2 \rfloor$	$2N+1$	even w_0
	$M = \lfloor \xi/2 \rfloor$	$2(M+1)$	odd w_0

3.4.2 Basins of attraction

Given the limit cycle to which a point w_0 tends, its basin of attraction can be written as

$$B_{w_0} = \{w \in \mathbb{R} | w = \lfloor w_0 \rfloor + 2k \pm d, k \in \mathbb{Z}\}, \quad d = w_0 - \lfloor w_0 \rfloor. \tag{3.31}$$

This structure of the basins of attraction is reflected in Fig. 3.8 for two different values of ξ. In this figure for each initial condition $w_0 \in [-3, 3]$ we plot the cycle in $\mathscr{A}$ which traps it. The figure suggests a periodic structure in the horizontal direction. It reflects the

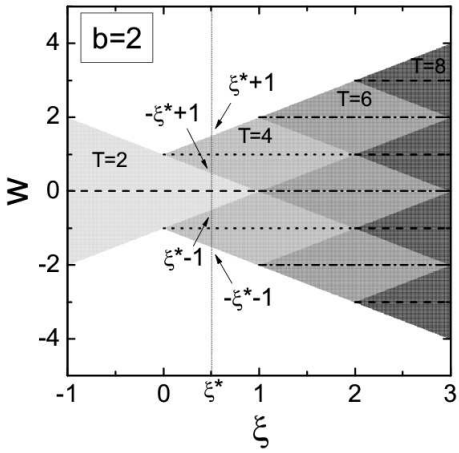

Fig. 3.7 Structure of the attracting segment ($b = 2$) in phase space for different values of ξ. The different tones of gray code cycles with different periods (periods are written inside the gray coded areas). The discontinuous horizontal lines stand for individual cycles with integer elements of periods 1, 2, 3 and 4 (dashed, dotted, dash-dotted and dashed respectively) embedded in the continuum of cycles of the attracting segment. The frontiers given by $\mathscr{B}$ have been explicitly identified for a particular value $\xi^\star$ of the discontinuity parameter fulfilling $0 < \xi^\star < 1$.

partition of phase space into equivalence classes established by (3.31). More specifically, all even, odd and odd half-integer initial conditions constitute three equivalence classes by themselves. Any other initial condition generates its equivalence class by repeatedly adding alternatively $2d$ and $2(1-d)$. The combination of Table 1 and (3.31) allows to

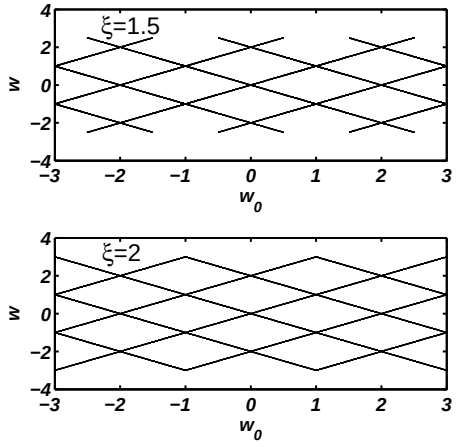

Fig. 3.8 Structure of the basins of attraction for $b = 2$ and two different values of the discontinuity location parameter ξ. The graphs show the final attractor for each w_0. For $\xi = 1.5$ (upper panel) infinite limit cycles of periods 4 and 6 exist as well as the period-2 cycle $\{$-1,1$\}$ and the period-3 cycle $\{$-2,0,2$\}$ can be seen. For $\xi = 2.0$ (lower panel) infinite limit cycles of period-6 are present filling the space between the points of the period-3 cycle $\{$-2,0,2$\}$ and the period-4 cycle $\{$-3,-1,1,3$\}$.

determine the period of the cycle to which an arbitrary point w_0 tends. For the sake of illustration, consider the case $\xi = 1.5$ and the initial condition $w_0 = 2.7$. In this case $n = \lfloor \xi \rfloor = 1$ and the frontiers inside the segment $\mathscr{A}$ are given by

$$\mathscr{B} = \{w^1, w^2, w^3, w^4, w^5, w^6\} = \{-2.5, -1.5, -0.5, 0.5, 1.5, 2.5\}. \tag{3.32}$$

Since the chosen initial condition falls outside the attracting segment we will make use of (3.31) to determine another initial condition $w_0' \in B_{w_0}$ leading to the same final limit cycle. Choosing $k = 0$ we can readily find

$$w_0' = \lfloor w_0 \rfloor + 2k - d = 1.3 \in (w^4, w^5). \tag{3.33}$$

If we now take into account the classification detailed in Table 3.1 we can conclude that both w_0 and w_0' will enter a limit cycle of period 4. It can be checked that this is in fact the case in the upper panel of Fig. 3.8.

3.5 Dependence on c: Discontinuity location

The dependence of the system with respect to the parameter c with r fixed, or equivalently ξ fixed, exhibits a large variety of features. We describe the system in the chaotic regime. First near the bifurcation point $b = 2$, and next for higher b.

3.5.1 Near $b = 2$

In Fig. 3.9 we plot the bifurcation diagram as a function of c, computed with $b = 2.01$ and $r = 4$. For $c < 1$ the trajectories x_n wander in two relatively large chaotic bands in contrast with the extremely narrow ones for $c > 1$. The upper panel in the figure gives the Lyapunov exponent. It is everywhere positive, as it must be for a chaotic regime. As a function of c, its value changes suddenly at every band merging crisis observed in the bifurcation diagram. To study the diagram with further detail we present in Fig. 3.10 – 3.12 magnifications of small areas in Fig. 3.9. The region with $c < 1$, near $b = 2$, has

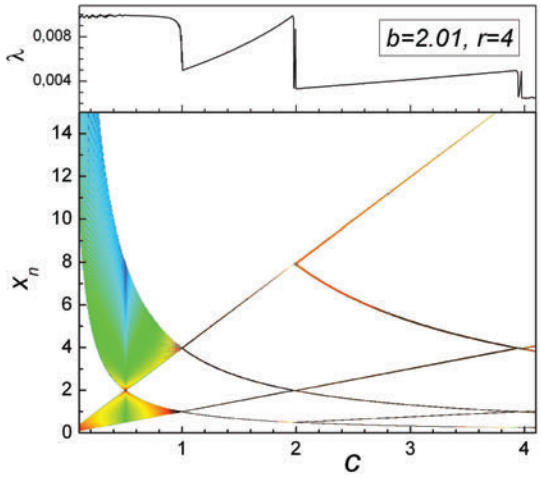

Fig. 3.9 Bifurcation diagram (bottom panel) and Lyapunov exponent (upper panel) obtained using $b = 2.01$ and $r = 4$.

further interesting features. Thus, what in Fig. 3.9 appears as two dense chaotic bands does have structure when minutely examined. Fig. 3.10 shows this feature for the up-

per band. The grid structure in the bifurcation diagrams as a function of c (or ξ) fades as c decreases. The Lyapunov exponent in the upper panels exhibits jumps associated with chaotic bands merging crises. For $c > 1$, the bifurcation diagram in Fig. 3.10 ex-

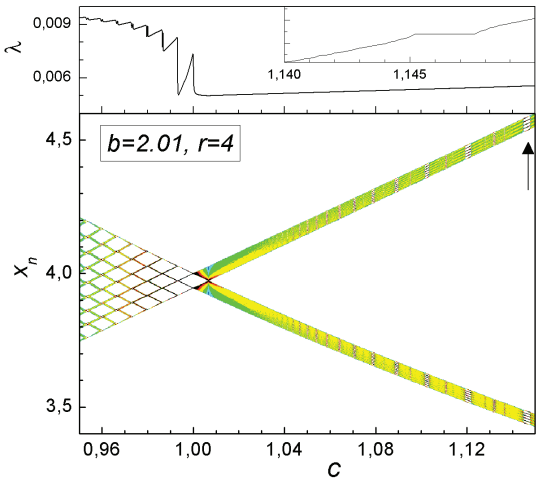

Fig. 3.10 Bifurcation diagram (bottom panel) and Lyapunov exponent (upper panel) obtained using $b = 2.01$ and $r = 4$. This plot presents a zoom of Fig. 3.9. The inset in the upper panel allows to appreciate the plateau in λ.

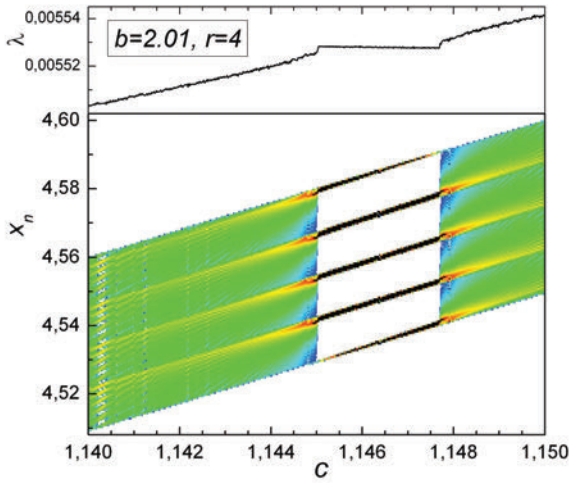

Fig. 3.11 Bifurcation diagram (bottom panel) and Lyapunov exponent (upper panel) obtained using $b = 2.01$ and $r = 4$. This plot presents a zoom of Figure 3.10 in the region located by the arrow. It exhibits interior crises.

hibits further details after magnification. A zoom of the area indicated by the arrow is given in Fig. 3.11 where a sudden variation of the size of the attractor is apparent. This thin window is composed by twenty two chaotic narrow bands (only five in the zoom). Furthermore, the crossing of Harter lines in Fig. 3.13 punctuate the start and end of the shrunk chaotic bands. An unstable orbit exists inside the window, which is represented by the dashed lines in the Fig. 3.13. Consequently, what we observe in Fig. 3.11 as a shrinking and widening of the attractor corresponds, actually, to a pair of interior crisis [19, 22, 43]. Moreover, further interior crises of various smaller sizes appear inside the

window itself in a, possibly, self-similar way. For instance, in the leftmost part of this bifurcation diagram ($1.14 < c < 1.1405$) one can hint a crisis of the very same kind.

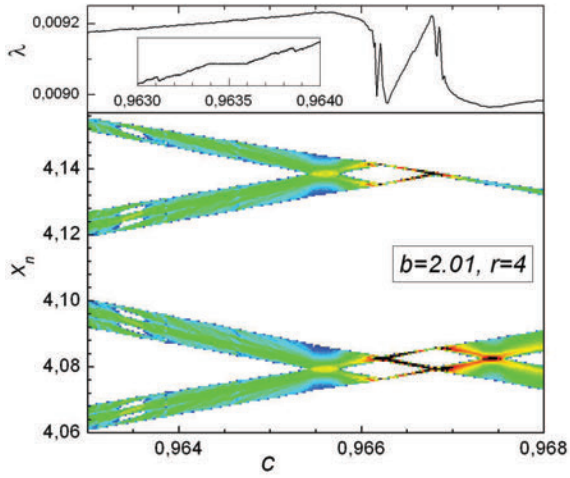

Fig. 3.12 Bifurcation diagram (bottom panel) and Lyapunov exponent (upper panel) obtained using $b = 2.01$ and $r = 4$. This plot presents a zoom of Fig. 3.10. The inset in the upper panel allows to appreciate the plateau in λ.

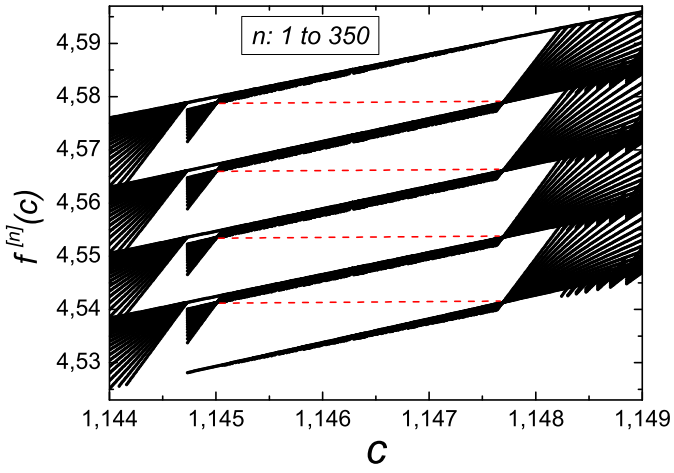

Fig. 3.13 Detail of the first 350 Harter curves obtained using $b = 2.01$ and $r = 4$. Dashed (red) lines between crossings of harter curves correspond to unstable fixed points.

Fig. 3.12 corresponds to a zoom of the left and uppermost part of the bifurcation diagram in Fig. 3.10. The Lyapunov exponent in the upper panel shows oscillations at band merging crises and, once again, a plateau (only visible in the inset) at the crisis located at $0.963 < c < 0.964$. An explanation for the occurrence of λ plateaus is deferred to Section 3.5.3. For $c > 1$ and close to the critical point $b = 2$, the crises take place at integer values of ξ. This feature is illustrated in Fig. 3.14. The left panel shows λ as a function of c for $b = 2.01$ and three different values of r. The right panel corresponds

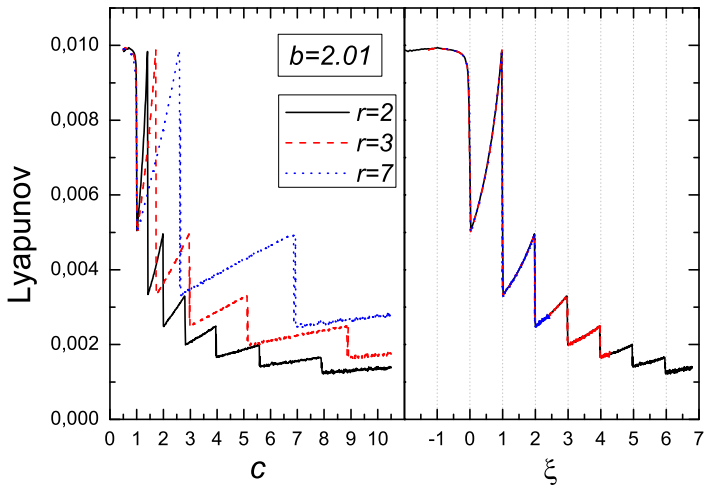

Fig. 3.14 Left panel: Lyapunov exponent as a function of c for three values of r. Right panel: Collapse of the same three curves as a function of ξ

to the same data expressed in terms of ξ: all three curves collapse onto a master curve. Furthermore, the value of the Lyapunov exponent is invariant also in magnitude. This property disappears for higher values of b, far from the critical point. All this buttresses the existence of universality in the system near the transition order-to-chaos.

Bifurcation diagrams of the VGH system always collapse when expressed in terms of z versus ξ. This is true even far from $b = 2$, in contrast with the Lyapunov exponent diagrams.

3.5.2 Far from $b = 2$

The lower panel of Fig. 3.15 gives a view of the bifurcation diagram near $c = 1$, with $r = 4$ and $b = 2.1$. The upper panel shows an enlargement of the region located by the arrow below. This is again an instance of interior crisis. Concomitantly, the uppermost panel shows the variation of the Lyapunov exponent. At variance with Fig. 3.10–3.12, here λ exhibits neither jumps nor plateaus across the window where the attractor shrinks. The reason is explained in the next subsection. In the bifurcation diagram of Fig. 3.16, with $b = 2.2$ and $r = 2$, the band merging phenomenon is more involved than in Fig. 3.9. The corresponding Lyapunov exponent, in the upper panel, exhibits large variations at crises too. However, these do not take place any longer at integer values of ξ.

Eventually, in Fig. 3.17, where $b = 3$, we observe that the Lyapunov exponent presents a large plateau whereas in the corresponding bifurcation diagram no interior crisis occurs. We have not found a justification for this case.

3.5.3 Interior crises and λ *plateaus*

A plausible explanation for the origin of λ plateaus occurring between interior crises pairs reads as follows. According to our numerical simulations, the narrow windows

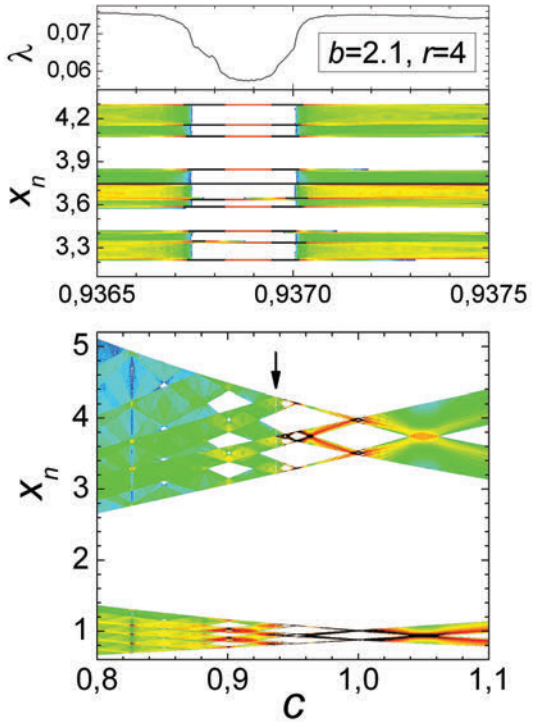

Fig. 3.15 Bottom panel: Bifurcation diagram as a function of c, with $b = 2.1$ and $r = 4$. The arrow locates the narrow window zoomed in the upper panel where λ is also shown.

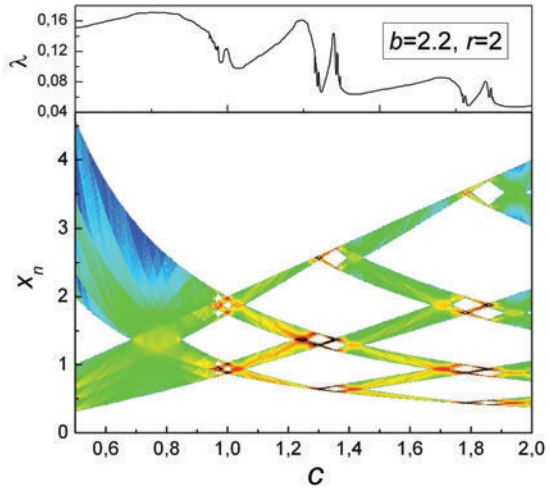

Fig. 3.16 Bifurcation diagram and Lyapunov exponent as a function of c. This particular plot was obtained using $b = 2.2$ and $r = 2$. The system is not close to the critical point $b = 2$.

between interior crises of the VGH map resemble very much the so-called cycles of chaotic intervals, where the trajectories jump in a cyclic way from one chaotic band to another. Such a phenomenon occurs, for instance, in the logistic map [44] and is also termed in the literature as cyclic chaotic attractor or cyclic chaotic bands [45].

Trajectories look quite regular and, if the line $x_n = c$ in the bifurcation diagram does not cross any of the thin bands inside the window, then the proportion of exterior points ($x_n > c$) remains almost constant. As a consequence of it and taking into account the

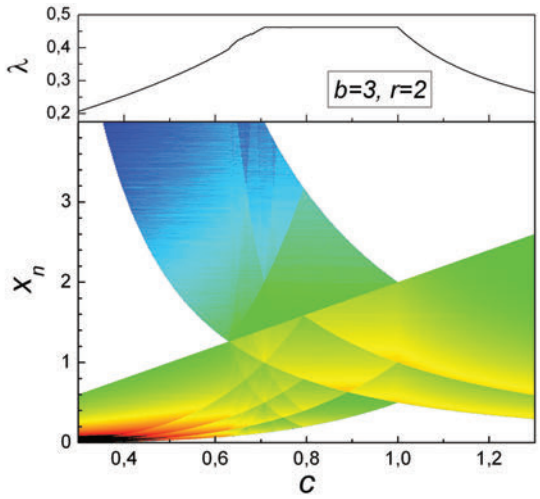

Fig. 3.17 Bifurcation diagram and Lyapunov exponent as a function of c, with $b = 3$ and $r = 2$.

interpretation of λ for this map at the end of Section 3.2.2, the Lyapunov exponent gets the plateau shape. Otherwise, λ varies across the window, as in Figure 3.15.

3.5.4 Crisis-induced intermittency

Next we gather some results, obtained from numerical simulations, concerning the behavior of trajectories around interior crises.

We commence by pointing out that interior crises in the VGH map appear in pairs. As the parameter c increases through a star value c_1^* the chaotic attractor suddenly shrinks into thin chaotic bands. This is the first interior crisis. Then, there exists a second star value $c_2^* > c_1^*$ where the set of thin bands suddenly widen and the attractor at $c > c_2^*$ recovers its previous size. This is the second interior crisis of the pair. By contrast, in the logistic map, a tangent bifurcation precedes always an interior crises [22].

For values of c slightly different than a star value, in the region where the attractor widens ($c \lesssim c_1^*, c \gtrsim c_2^*$), the orbits spend long stretches in the region where the attractor is confined between the two crises. Occasionally, the trajectories burst and visit the whole attractor. This behavior, termed crisis-induced intermittency [22, 46], is illustrated in Fig. 3.18. There, two orbits are plotted for slightly different values $c_1 = 0.8840$ and $c_2 = 0.8845$, located at both sides of the star value $c^* = 0.88411175\ldots$. The empty square symbols stand for a trajectory in a regime where the attractor is still large. Intermittency is clearly observed. The solid dots represent a trajectory in a regime with shrunk attractor. It seems, at first glance, a period-8 orbit but the inset, which is a zoom of just one single narrow band, allows us to illustrate its non-periodic character.

For fixed c, the statistics of the length of laminar stretches where the orbit stays confined in the region of the shrunk attractor is well described by an exponential distribution, provided $|c - c^*|$ is small, which yields a characteristic length $\tau(c)$. It has been shown [46] that for a large class of dynamical systems which exhibit crises, the dependence reads

$$\tau \sim |c - c^*|^{-\gamma}. \tag{3.34}$$

Indeed, this is the case for the VGH map. We have built up the statistics of τ as a function of $|c-c^*|$ for the case in Fig. 3.18. The results are given in Fig. 3.19. The linear fit in log-log scales yields a determination of the critical exponent: $\gamma = 0.89 \pm 0.02$.

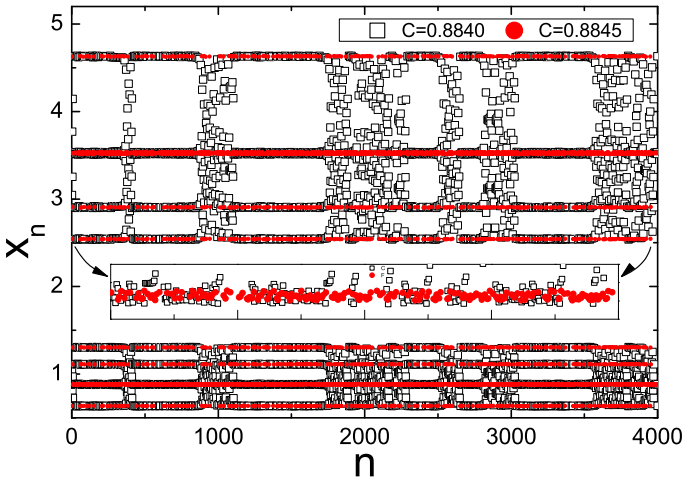

Fig. 3.18 Crisis-induced intermittency, with $r = 4$ and $b = 2.2$. Two trajectories from both sides of the critical value $c^* = 0.88411175\ldots$ are compared. Solid dots (red) correspond to a trajectory with $c = 0.8845$, where the attractor splits in narrow bands. Empty squares (black) correspond to $c = 0.8840$, namely in the wider region of the attractor. The inset is a zoom of the points close to $x = 2.5$ and allows to illustrate the non-regular character of these trajectories.

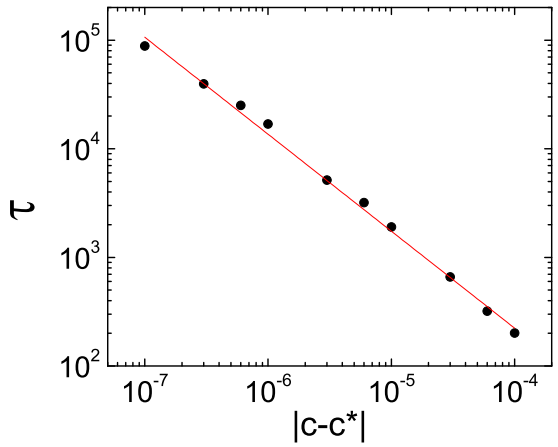

Fig. 3.19 Characteristic length τ versus $|c-c^*|$ in log-log scales. Each dot was obtained from 100 initial conditions and series of 10^6 iterates, with $c^* = 0.88411175$, $b = 2.2$ and $r = 4$. The slope of the linear fit is $\gamma = -0.89 \pm 0.02$.

3.5.5 A numerical flaw

Version (3.8) of the map presents a worth mentioning numerical nuisance. Namely, for some integer values of $b > 2$, computer generated trajectories collapse to an unstable periodic orbit after some iterations. A numerical artifact of similar nature has been studied in [47, 48].

The dynamics for real z may be viewed as follows. For an initial point $z_0 < \xi$, every iteration conveys a shift to the right by two units until the condition $z_n > \xi$ is fulfilled. The second line in (3.8) may be read as: $\{(1-b)\lfloor z_n \rfloor + 2\} + (1-b)(z_n \bmod 1)$. Thus, for integer $b > 2$ the quantity in brackets is an integer and hence, its successive iteration conveys just a shift, as above. The key point is that, for finite machine precision, the last term dramatically looses precision in each iteration for some particular integer values of $b > 2$.

This effect may be understood on the basis of a generalization of the Bernoulli or binary shift map: $z_{n+1} = 2z_n \pmod 1$. To this end, let us use the binary representation of the number $z_n \bmod 1$. Multiplication in base 2 is very simple in some cases. For instance, when $|1-b| = 2^k$ we get the binary representation of the product $2^k(z_n \bmod 1)$ simply by shifting $k-1$ places to the left every bit and (due to the finite precision of the computer) adding simultaneously $k-1$ zeros to the right of the number. Henceforth this number gets shifted by two units in every iteration till it reaches $z_n > \xi$ when the mod operator acts again. This way, the piece in bracket is preserved as an integer under the action of the floor function, whereas the term $2^k(z_n \bmod 1)$ looses significant digits before going through the loop again. Eventually it stops when, after a number of iterations, $2^k(z_n \bmod 1) = 0$. At this point the iteration reduces to a periodic orbit with elements located at integer numbers. The full output is then a set of limit cycles whose elements are always integers. This misleading result is just consequence of the computer finite precision.

3.6 Discussion and conclusions

We have revisited a one-dimensional population model, proposed as an instance of density dependent dynamics. The fitness parameter b controls the onset of chaos. Values $b > 2$ convey chaos. Otherwise the system is regular. On the critical point $b = 2$ the attractor is made of an infinity of limit cycles that share a finite number of different periods. Hence, the transition order-to-chaos takes place through three steps: *i*) Finite number of limit cycles for $b < 2$; *ii*) Infinite number of limit cycles with finite number of different periods at $b = 2$; and *iii*) Chaos for $b > 2$. We have named this transition bisecting bifurcation and we have given and exact description of the system at the bifurcation point ($b = 2$).

The described bisecting bifurcation is accompanied by border-collisions [24, 25, 28] as can be seen in Fig. 3.5 and, more clearly, in Fig. 3.20. In the example described in these figures, two of the three unstable fixed points of $V^2(x)$ (for $b > 2$) collide with discontinuities of the map when $b = 2$ and cease to exist for $b < 2$. The third fixed point does not collide with a border and becomes a stable fixed point of the map for $b < 2$.

An attempt to classify the phenomenology of border-collision bifurcations in one-dimensional discontinuous maps can be found in [30]. The classification for continuous maps is studied in [29]. Both classifications are based on the linearization of the

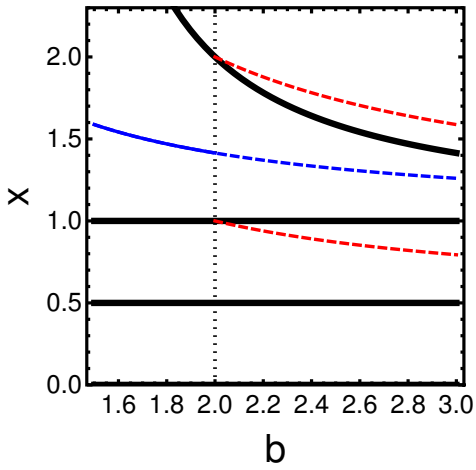

Fig. 3.20 Illustration of border-collisions for $V^2(x)$. The thick black lines correspond to the position of the borders of $V^2(x)$ ($r = 2$, $c = 1$) as a function of b. The vertical dotted line locates the bifurcation. The dashed curves stand for the position of the fixed points of $V^2(x)$. For $b > 2$ there are three unstable fixed points. When $b = 2$ two of these fixed points collide with the borders and cease to exist whereas the third one becomes stable for $b < 2$.

map around the collision point both in phase space and parameter space. However, the bisecting bifurcation presented here corresponds to one of the critical cases explicitly excluded from the classification where the linearization of the map provides no insight on the actual bifurcation phenomena. For example, if we linearize the map around the border-collision point of the first unstable fixed point, we get the 1-D normal form map [29]

$$G_1(x) = \begin{cases} \alpha x + \mu, & x \leq 0, \\ \beta x + \mu, & x > 0, \end{cases} \tag{3.35}$$

with parameters $\alpha = -1$, $\beta = 1$, which fall on one of the frontiers of the classification (see Appendix A for further detail). In our opinion, this sheds some light on this particular type of border-collisions by studying the dynamics around the bifurcation.

In this study we have restricted our attention to the VGH map but what we have called bisecting bifurcations are present in other continuous and discontinuous piecewise smooth maps. However, to the best of our knowledge, they have very often gone unnoticed in the literature. In the continuous case, bisecting bifurcations can be observed in maps such as the skew tent map [49] or the map describing the dynamics of the boost converter [29]. In particular, in [50] a continuous piecewise smooth map introduced as a model of economic growth [51] is studied and the values of the parameters for which a bisecting bifurcation takes place are identified. Discontinuous maps candidates to show bisecting bifurcations can be found in [52, 53]. Our numerical experiments have shown this is in fact the case. Moreover, the map studied in [52] shows coexistence of different periods in the set of neutrally stable limit cycles with a structure very similar to the one described in this paper for the VGH map.

Chapter 4
A two-dimensional case study: The Lozi map

4.1 Introduction

In 1978, Lozi introduced in a short note [54] a two-dimensional map the equations and attractors of which resemble those of the celebrated Hénon map [55]. Simply, a quadratic term in the latter is replaced by a piecewise linear contribution in the former. This allows one to rigorously prove the chaotic character of some attractors [56] and a detailed analysis of their basins of attraction [57]. The equations for the iterated Lozi map $L(x,y)$ read

$$\begin{aligned} x_{n+1} &= 1 + y_n - a|x_n| \equiv f(x_n, y_n) \\ y_{n+1} &= b x_n \equiv g(x_n, y_n), \end{aligned} \tag{4.1}$$

where a, b are real non-vanishing parameters. Inside the region where the orbits remain bounded, the Lozi map may present both regular and chaotic behavior.

In this chapter we will show that the Lozi map also exhibits bisecting bifurcations. As a function of the parameters the transit may take place from regular to regular as well as to chaotic regimes.

As we have seen in the previous chapter, in one-dimensional maps this kind of transitions happens whenever a piece of an iterate of the map becomes co-linear with the bisectrix in the cobweb for a particular parameter value. We will extend this explanation to maps in two dimensions and further discuss its connection with the theory of border collisions, which is commonly used to analyse this kind of maps [24, 27, 58].

4.2 Dynamics of the Lozi map: isolated attractors and stability

It is customary to start the study of a dynamical system with a catalogue of its fixed points, periodic attractors and so on, paying special attention to their stability and evolution with the system parameters. We start by collecting some of these features for the Lozi map.

For stability considerations we need the Jacobian matrix of $L(x,y)$ which reads

$$J(x,y) = \begin{pmatrix} -a\,\mathrm{sign}(x) & 1 \\ b & 0 \end{pmatrix}. \tag{4.2}$$

Notice that $J(x,y)$ depends on the point of the orbit only through $\mathrm{sign}(x)$. Accordingly, we denote its values as $J_+ \equiv J(x>0,y)$ and $J_- \equiv J(x<0,y)$. Furthermore, since $\det J_\pm =$

$-b$, we will only consider maps with $|b| \leq 1$, in order to have non-expanding systems. In particular, the maps with $b = \pm 1$ are area-preserving.

It is a simple exercise to see that for $|b| \leq 1$ the Lozi map has no fixed points if $a \leq b-1$. It has P_1 as the unique fixed point if $b-1 < a \leq 1-b$, and gains an additional fixed point, P_2, if $a > 1-b$, with

$$P_1(a,b) \equiv \Big(\frac{1}{1+a-b}, \frac{b}{1+a-b}\Big) \qquad P_2(a,b) \equiv \Big(\frac{1}{1-a-b}, \frac{b}{1-a-b}\Big). \tag{4.3}$$

Furthermore $J(P_1) = J_+$, $J(P_2) = J_-$. Therefore, only P_1 can be stable and this happens for systems with parameter values (b,a) inside the triangle with vertices $(1,0),(-1,2),(-1,-2)$ in parameter space.

As for isolated cycles of period $T = 2$, it is easy to see that they exist, if we keep $|b| < 1$, for $a > 1-b$. Their elements are (z_1, bz_2) and (z_2, bz_1), with

$$z_1 = \frac{1-b+a}{(1-b)^2+a^2} \qquad z_2 = \frac{1-b-a}{(1-b)^2+a^2}. \tag{4.4}$$

They are stable for parameter values (b,a) inside the triangle with vertices $(0,1),(1,0),(1,2)$ in parameter space.

The analysis so far is standard and may be pursued for more complicated attractors. We have recalled the previous facts just to better understand the bifurcations which will be studied in the next section.

4.3 Bisecting bifurcations and attracting sets

The fixed points and cycles mentioned above are isolated points in phase space. However, for particular values of the parameters a and b we can also find continuum sets of periodic points which act as attractors for certain regions of phase space. These can mediate bisecting bifurcations as we have described in the previous chapter for the one-dimensional VGH map. Here, we will follow the algebraic approach we described there to locate the values a and b that give rise to infinite sets of limit cycles. We solve first the cases of periods two and four which we think illustrate sufficiently the procedure. After that, we completely determine the elements of the cycles. Period three and five are then analyzed in the same way and shown to produce a different pattern. The stability of the cycles is also resolved. Higher order periodic attractors could be studied along the same line but the algebra becomes more involved.

4.3.1 Continuum of period-2 attractors

Let $\{(x_1,y_1),(x_2,y_2)\}$ be a period-2 cycle of the Lozi map. Next, instead of (4.1) we use the equivalent second order difference equation

$$x_{n+1} = 1 - a|x_n| + bx_{n-1}, \tag{4.5}$$

with the obvious corresponding change in the initialization of the iteration. The periodicity condition for this system conveys

$$x_2 = 1 - a|x_1| + bx_2, \tag{4.6}$$
$$x_1 = 1 - a|x_2| + bx_1. \tag{4.7}$$

The corresponding $2-$cycles of the Lozi map will be $\{(x_1, bx_2), (x_2, bx_1)\}$.

When the system of equations above is compatible but indeterminate then there exists an infinity of solutions and hence of period-2 cycles. From an algebraic point of view this means that the coefficient and the augmented matrices must both have rank one:

$$\begin{vmatrix} a\,\mathrm{sign}(x_1) & 1-b \\ 1-b & a\,\mathrm{sign}(x_2) \end{vmatrix} = 0, \quad \mathrm{rank} \begin{pmatrix} a\,\mathrm{sign}(x_1) & 1-b & 1 \\ 1-b & a\,\mathrm{sign}(x_2) & 1 \end{pmatrix} = 1, \tag{4.8}$$

which yield the constraints: $a > 0$, and either $b + a = 1$ or $b - a = 1$. Correspondingly there are two one-parameter families of $2-$cycles in $\mathbb{R}^2$, $\{S_1, S_2\}$ and $\{U_1, U_2\}$ with

$$S_1 = (x, b(1-ax)/a), \quad S_2 = ((1-ax)/a, bx), \quad (0 < x < 1/a, b = 1-a) \tag{4.9}$$

$$U_1 = (x, -b(1+ax)/a), \quad U_2 = (-(1+ax)/a, bx), \quad (-1/a < x < 0, b = 1+a). \tag{4.10}$$

For the $S-$family we have $J(S_1)J(S_2) = J_+^2$, whose eigenvalues are $(a^2 + 2b \pm |a|\sqrt{a^2+4b})/2$. In the critical case, $a + b = 1$, they reduce to the values 1 and $(1-a)^2$, and hence these orbits are neutrally stable for $0 < a < 2$.

For the $U-$family we have $J(U_1)J(U_2) = J_-^2$, whose eigenvalues in the critical case, $b - a = 1$, are 1 and $(1+a)^2 > 1$, with $a > 0$. Therefore these orbits are unstable.

4.3.2 Continuum of period-4 attractors

The search of sets of period-4 orbits yields the following results. First, the constraints on the parameters are $a = 1 + b$, and $0 < b < 1$, $1 < a < 2$, for the rank of the corresponding matrices to be equal to three, allowing in this way the existence of a one-parameter family of solutions. Second, if (x_i, y_i) denotes the cycle elements, with $i = 1, \ldots, 4$, then

$$x_1 = \mu + 2b\beta, \quad x_2 = \mu - (b-1)\beta, \quad x_3 = -\mu, \quad x_4 = -\mu + (b+1)\beta, \tag{4.11}$$
$$y_1 = bx_4, \quad y_2 = bx_1, \quad y_3 = bx_2, \quad y_4 = bx_3, \tag{4.12}$$

where we have used the real parameter $0 < \mu < 1$ and the definition $\beta \equiv 1/(1+b^2)$.

One can readily deduce from the expression of the cycle elements (4.11) that the $x-$components are alternatively positive and negative. Therefore the corresponding Jacobian matrix reads simply $(J_+J_-)^2$, whose eigenvalues are 1 and $(1-a)^4$ in the critical case. Hence, these period-4 orbits are neutrally stable and their union acts as an attractor.

4.3.3 Period-3 attractors

Following the same algebraic procedure as in the preceding subsections, we have determined that an infinite set of cycles of three elements exists only if $a = 1$ and $b = -1$. However, in this case the rank of the corresponding coefficient and augmented matrices is equal to one and, as a consequence of it, we get a continuum of solutions depending on two parameters.

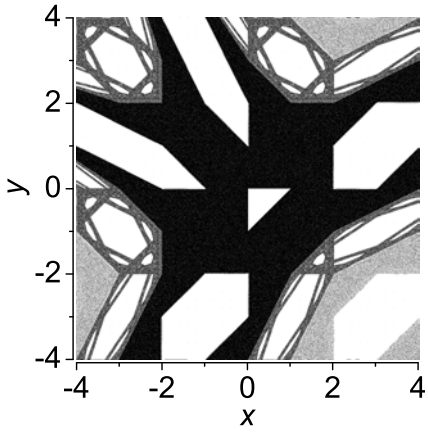

Fig. 4.1 Attractor of the system $a = 1$, $b = -1$. Black and gray regions stand for chaotic trajectories. The white areas contain only periodic orbits with neutral stability. In particular, the innermost triangle with right angle vertex at $(0,0)$ contains only period-3 trajectories.

A phase portrait which includes the period-3 orbits is shown in Fig. 4.1. Orbits of period-3 fill completely the white triangle at the center of Fig. 4.1, with right angle vertex at $(0,0)$. The acute angle vertices are located at $(1,0)$ and $(0,1)$. The elements of the cycle are given by $(\xi,-\eta)$, $(1-\xi-\eta,-\xi)$ and $(\eta,-1+\xi+\eta)$, in terms of the parameters $0<\xi,\eta<1$. The remaining white areas correspond to regular orbits of higher periods. Finally, the black and grey areas stand for chaotic trajectories.

The two eigenvalues of the Jacobian matrix of $L^{[3]}(x,y)$ evaluated on the orbit elements are equal to one, which stands for double neutral stability. Hence, the set of orbits of period-3 is two-dimensional in phase space, at variance with period-2 and -4, and is embedded into the sea of chaotic trajectories.

4.3.4 Period-5 *attractors*

The situation with period-5 attractors is similar to the one with period-3. We have found two two-parameter sets of orbits with neutral stability. They emerge when $b=-1$ and either $a=(1+\sqrt{5})/2\equiv\phi$ (the golden ratio) or $a=(1-\sqrt{5})/2$. Table 4.1 collects the elements $\{x_i,y_i\}$, with $i=1,\ldots,5$, of the orbit. We use the notation $\varphi\equiv(\sqrt{5}-1)/2=\phi-1=1/\phi$. The two parameters u and v which define the family of period-5 orbits vary in the pentagon of vertices $\{(\varphi^2,0),(\varphi,0),(\varphi^2,\varphi^2),(0,\varphi),(0,\varphi^2)\}$ in parameter space, provided $a=\phi$. Else, if $a=-\varphi$, the two parameters vary in the pentagon of vertices $\{(0,0),(1,0),(\phi,1),(1,\phi),(0,1)\}$. As far as stability is concerned, a direct calculation shows that the Jacobian matrix of $L^{[5]}(x,y)$ for the parameter values just quoted is indeed the unit matrix which means double neutral stability.

a	i	1	2	3	4	5
ϕ	x_i	$1-\phi v-u$	$-\varphi+\phi(u+v)$	$1-\phi u-v$	u	v
	y_i	$-v$	$\phi v+u-1$	$\varphi-\phi(u+v)$	$\phi u+v-1$	$-u$
$-\varphi$	x_i	$1+\varphi v-u$	$\phi-\varphi(u+v)$	$1+\varphi u-v$	u	v
	y_i	$-v$	$u-\varphi v-1$	$\varphi(u+v)-\phi$	$v-\varphi u-1$	$-u$

Table 4.1 Elements of the period-5 orbits $\{x_i, y_i\}$, $(i = 1,\ldots,5)$. The upper block entry is for $a = \phi$. The real parameters u, v take values inside and on the pentagon of vertices $\{(\varphi^2,0),(\varphi,0),(\varphi^2,\varphi^2),(0,\varphi),(0,\varphi^2)\}$ of parameter space. The lower block entry is for $a = -\varphi$ and the parameters are inside and on the pentagon of vertices $\{(0,0),(1,0),(\phi,1),(1,\phi),(0,1)\}$ in parameter space. In both cases it is $b = -1$. All the orbits elements stay in the first quadrant of phase plane.

4.3.5 Bifurcation diagrams

In the Lozi map, when enough initial conditions are considered for the numerical simulation, the continua of $2-$ and $4-$cycles discussed above may act as an attractor and show up also as a vertical line in the bifurcation diagram. This is clearly seen in Fig. 4.2 for fixed $b = 0.1$. To construct this diagram especial care has been payed to sweep a large number of initial conditions. For every trajectory a large enough transient is discarded. Also, if a component increases beyond a given threshold the trajectory is considered as unbounded. Fig. 4.2 exhibits a bifurcation from period-1 to period-2 at $a = 0.9$ and another one from period-2 to chaos at $a = 1.1$. This numerically obtained diagram illustrates clearly that these two bifurcations are mediated by the attractors described in sections 4.3.1 and 4.3.2 respectively. A further feature of Fig. 4.2 is that in the approximate intervals $1.1 < a < 1.237$ and $1.237 < a < 1.406$, the trajectories jumps between the chaotic bands in a cyclic manner, with periods 4 and 2 respectively.

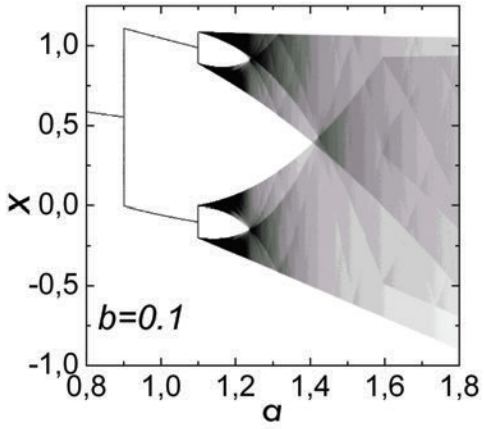

Fig. 4.2 Bifurcation diagram for $b = 0.1$. Notice that the bisecting bifurcations take place at $a = 1 \pm b$.

Similarly, in Fig. 4.3, here for fixed $a = 1.5$, two bifurcations occur at $b = \pm 0.5$, again mediated by the same mechanism. The system is chaotic for $b = 0.1$ and $a > 1.1$ in Fig. 4.2, and $a = 1.5$, $-0.5 < b < 0.5$ in Fig. 4.3. Similarly to the VGH map, these vertical segments of infinite sets of periodic orbits are produced by bisecting bifurcations. Eventually, cyclic jumping between the chaotic bands of the diagram takes place with period 2 and 4 to the left and right of the figure, respectively.

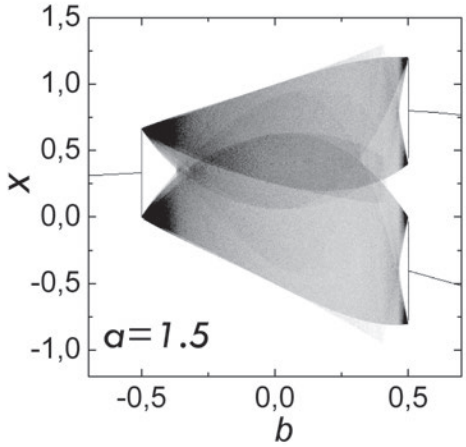

Fig. 4.3 Bifurcation diagram for $a = 1.5$. Notice that the bisecting bifurcations take place at $b = \pm(a-1)$.

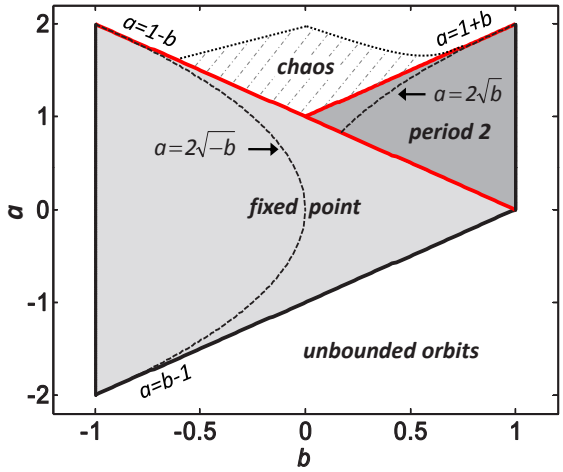

Fig. 4.4 Behaviour of the Lozi map in parameter space. White areas correspond to unbounded trajectories. The bisecting bifurcations take place at the red straight lines, $a = 1 \pm b$. This diagram does not exhaust all the possible attractors the Lozi map may exhibit.

We gather the information discussed so far in Fig. 4.4 where the behavior of the Lozi map in different regions of the parameter space is indicated. Trajectories for $|b| > 1$ are unbounded. Numerical simulations indicate this is also the case for the northern and southern parts of the diagram. The identification of the chaotic area has been done by computing numerically the Lyapunov exponents [20], thus the upper border of chaos is approximate. The numerical algorithm is explained in E. The borders of their stability region will be analysed in detail later on. The diagram by no means exhausts the variety of behaviors the trajectories of the Lozi map may develop [59].

4.4 A geometrical explanation for the bisecting bifurcations in the Lozi map

In the previous chapter, a geometrical explanation for the bisecting bifurcations in piecewise one-dimensional maps is provided. Here we develop a generalization for the two-dimensional Lozi map, albeit graphical illustration is more involved. Fig. 4.5 represents

the surface $f^4(x,y)$ and allows us to appreciate how the simple shape of $f(x,y)$ in (4.1) gets convoluted after iteration.

Notice that for the Lozi map, the existence of a bisecting bifurcation in the variable x implies its presence in the variable y, and viceversa. This is due to the fact that y is just a one iteration delayed and re-scaled version of x. This observation will render easier the design and interpretation of some three dimensional diagrams.

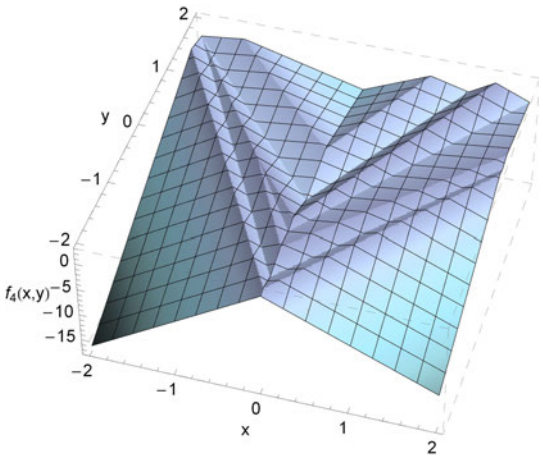

Fig. 4.5 Surface defined by the iterate $f^4(x,y)$ in the definition of the Lozi map, with $a = 1.5$ and $b = 0.5$.

From an algebraic point of view, we will find an infinity of period-n limit cycles if

$$f^n(x,y) = x, \quad g^n(x,y) = y, \tag{4.13}$$

for some range of (x,y) values, as illustrated for $n = 2$ to 5 in section 4.2. Clearly, this is the condition of fixed point extended to a continuous set of points in phase space. Furthermore, this is only a necessary condition for the observation of the infinity of limit cycles since its stability is not assured by it.

In one-dimensional maps it is a common practice to construct and study trajectories using the cobweb diagram. In a two-dimensional generalization we can visualize $f^n(x,y)$ and $g^n(x,y)$ as surfaces to which a point $p \equiv (x_m, y_m)$ of the phase plane is projected upward in order to find the new $x_{m+1} = f^n(x_m, y_m)$ and $y_{m+1} = g^n(x_m, y_m)$ on the vertical axis. This procedure is illustrated in Fig. 4.6 for the particular case $n = 1$. The horizontal plane stands there for the phase plane. The vertical axis is common for both surfaces $f^n(x,y)$ and $g^n(x,y)$, which have been sketched only partially. Using the cobweb diagram technique, the values x_{m+1} and y_{m+1} are sent back to the phase plane. Thus, the value x_{m+1} is first projected toward the bisectrix line $f^n(x,0) = x$ and then down to the x-axis. Similarly, y_{m+1} is first projected toward the bisectrix $g^n(0,y) = y$ and then down to the y-axis. This gives the point $q \equiv (x_{m+1}, y_{m+1})$ on the phase plane of Fig. 4.6.

Let us now interpret condition (4.13) in geometrical terms. The presence in a two-dimensional map of a bifurcation mediated by an infinite set of neutrally stable cycles implies the existence of a segment, or set of segments, in the phase plane whose projections upward on the surfaces $f^n(x,y)$ and $g^n(x,y)$ are contained in the bisecting planes $f^n(x,y) = x$ and $g^n(x,y) = y$ respectively.

In the case of the Lozi map, f and g allow explicit solutions for condition (4.13) to be found, at least for low values of n. Next we focus on the particular case of the bifurcation occurring at $a = 1 - b$ with $a > 0$. In this case the limit cycles at the bifurcation point

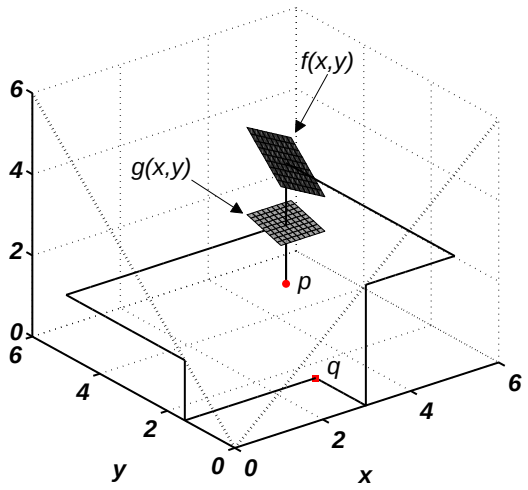

Fig. 4.6 Example of two-dimensional cobweb diagram for the Lozi map ($a = 0.6$, $b = 0.3$). The point $p \in \mathbb{R}^2$ is projected to the surfaces $f(x,y)$ and $g(x,y)$ and these projections are brought back down to $\mathbb{R}^2$ by means of reflections in the bisectrix $f(x,0) = x$ and $g(0,y) = y$ in order to find the new point q. For the sake of clarity only one small region of each surface is shown.

are all period-2 cycles, i.e. fixed points of $L^2(x,y)$. In Fig. 4.7 we have represented the surface $f^2(x,y)$ and the generalized cobweb procedure described above. For the sake of clarity, any analogous representation concerning $g^2(x,y)$ has been omitted. The plot has been generated for $b = 0.1$ and $a = 0.9$. Any initial condition (x_0, y_0) lands, after a certain transient, on the segment $y = b(1-ax)/a$ with $0 < x < 1/a$ (red line in Fig. 4.7). Every point of this segment is a fixed point of $L^2(x,y)$. When projected to the surface $f^2(x,y)$ they graze the bisector plane $f^2(x,y) = x$ and then come back to their position in the phase plane. Since this segment is invariant under the transformation $L^2(x,y)$, any point in the segment is an element of a period-2 cycle of $L(x,y)$.

In summary, from a three-dimensional geometrical perspective, we will find an infinite set of limit cycles of period n from the Lozi map when the projections on the phase plane of the two curves produced by the intersections of i) the surface $f^n(x,y)$ and the bisector plane $z = x$, and ii) the surface $g^n(x,y)$ and the bisector plane $z = y$, overlap in a certain range of the variables x,y. Whenever the intersection is not a linear segment but an area, the system has double neutrally stable orbits, which is the case of the period-3 and -5 orbits we have studied.

4.5 Bifurcations and phase space

In this section we discuss the appearance of the bisecting bifurcations in connection with the changes in the stability of other attractors. This will further clarify the meaning of the vertical segments in bifurcation diagrams like the ones in Fig. 4.2 and 4.3. To be specific we fix $b = 0.5$ and plot in Fig. 4.8 twenty regular attractors in phase space corresponding to parameter values $a = 0.1\,n$, $n = 1, 2, \ldots, 20$.

The diagram allows us to appreciate how the fixed point attractor evolves with increasing a for $n = 1, \ldots, 4$. At $a = 1 - b = 0.5$, i.e. $n = 5$, the first bisecting bifurcation takes place. Observe that this is precisely where the neutrally stable fixed point $P_1(a,b)$

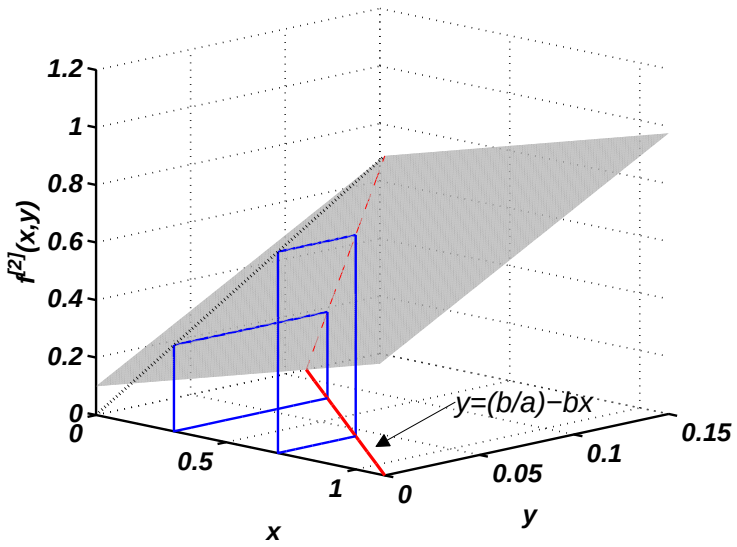

Fig. 4.7 Cobweb diagram for the 2nd iterate of the Lozi map with $b = 0.1$ and $a = 1 - b$. Only the $f^2(x,y)$ surface is shown. The cobweb trajectories (blue) of two different initial conditions ($x_0 = 0.3, 0.7$ and $y_0 = b(1-x_0)/a$) have been represented.

in (4.3) changes to be unstable. We note in passing that this type of behavior sounds familiar from the analysis of elementary systems. For example, in the most conventional period-doubling cascade that would mean the birth of a period-2 attractor. Here something of this sort is also observed because $2-$cycles exist to the right of $a = 0.5$. The difference is that the transition is mediated by a continuum of neutrally stable cycles of period-2 which fill up the segment in the figure.

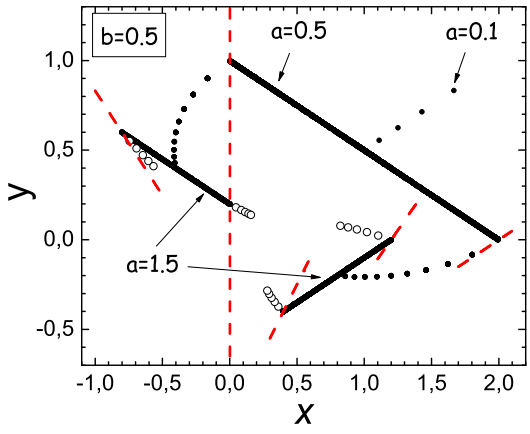

Fig. 4.8 Superposition of twenty attractors illustrating border collisions. $b = 0.5$ and $a = 0.1n$ with $n = 1, 2, \ldots, 20$. Period-2 and period-4 attractors associated to neutrally stable orbits ($a = 0.5$ and 1.5) correspond to the segments (solid pattern). In between, stable period-2 limit cycles. The dashed lines stand for the borders at the bifurcation values (as a matter of fact, the border $x = 0$ is invariant). The circles stand for a period-4 unstable orbit plotted for the values $a = 0.1n$, $n = 16, \ldots, 20$ which collides with the borders at the bifurcation.

When we go on with increasing a the system is periodic with stable period-2 cycles. These have been represented in the figure for nine values of a, namely $n = 6,\ldots,14$. Then, at $a = 1+b = 1.5$, the second bisecting bifurcation takes place. Again these parameters values punctuate the transition from stable to unstable for the 2-cycles mentioned in section 4.2. The two segments of the attractor are now built up by neutrally stable cycles of period-4, and they are apparent in Fig. 4.8. Values $a > 1.5$ convey chaos (not shown) with unstable cycles in it ($n = 16,\ldots,20$).

The case considered illustrates, for fixed b and varying a, how the Lozi map follows a route to chaos in three steps separated by two bifurcations characterized by the coexistence of a continuum of cycles with period 2 and 4 respectively. This corresponds in Fig. 4.4 to a raising vertical trajectory in parameter space. As a matter of fact this figure contains information on the whole family of bifurcation diagrams like the ones in Fig. 4.2 and 4.3 which stem from, respectively, vertical or horizontal displacements in parameter space. Accordingly, a variety of transitions are possible: fixed point to chaos, periodic cycle to chaos or fixed point to periodic cycle. We emphasize the role the bisecting bifurcations play in mediating these transitions.

Since piecewise continuous maps are usually analyzed in terms of border collisions [27, 58], it is in order to discuss the connection of the bisecting bifurcations with that scheme. In the particular case of the Lozi map, the described period-2 and period-4 attractors involving neutrally stable cycles may be seen as border collisions too. To see how this comes about we propose to look again at Fig. 4.8 but going in the reverse direction. Starting with systems with $a = 2$ and progressively decreasing its value ($n = 20,\ldots,16$), one finds unstable period-4 orbits represented by circles. For $a = 1.5$ these cycles collide with the borders, namely the discontinuities of $L^{[4]}(x,y)$ (dashed lines), originating the two segments made of an infinite set of neutrally stable cycles of period-4. After the collision, further decrease of a gives then rise to stable period-2 attractors for $a < 1+b = 1.5$. Following the way down, the 2-cycle collides, for $a = 1-b = 0.5$, with the discontinuities of $L^{[2]}(x,y)$ and we see a sudden and ephemeral segment of period-2 neutrally stable cycles. Finally, for $a < 0.5$ we find the stable fixed points P_1. Notice that in these collisions the location of the borders depends on a, except the one at $x = 0$ which is fixed.

As regards the chaotic regime, two examples of attractors appear in Fig. 4.9 intended to be complementary of Fig. 4.8. The upper panel is for $a = 1.55$ and shows an incipient zigzagged structure in phase space as the result of the destruction of the regular attractor $a = 1.5$ in Fig. 4.8. In the bottom panel, with $a = 1.7$, the strange attractor is apparent. It corresponds to the figure in the original reference [54]. This $V-$shaped structure seems to be the prototype of chaotic attractor with $|b| < 1$. Points in the dotted pattern originate unbounded orbits.

So far in this section we have considered $|b| < 1$. As has already been mentioned, systems with $|b| = 1$ are area-preserving and their attractors offer a large variety of structures. Fig. 4.1 is an instance of it. The system with $a = 1, b = -1$, contains doubly neutrally stable period-3 orbits embedded in chaos. In this regard, Fig. 4.10 illustrates that this situation corresponds also to a border collision. It shows the evolution with a of six different fixed points of $L^{[3]}(x,y)$ (curves coded as dashed and dot-dashed lines). The remaining lines in the plot stand for borders. The collisions between fixed points and borders at $a = 1$ are clearly observed.

The phase space shown in Fig. 4.1 exhibits a mixed structure of periodic an chaotic trajectories clusters. The complexity of the phase space is general for $|b| = 1$, even for non critical cases as $a = 1$. Fig. 4.11 shows the phase space, at the same scale as Fig. 4.1,

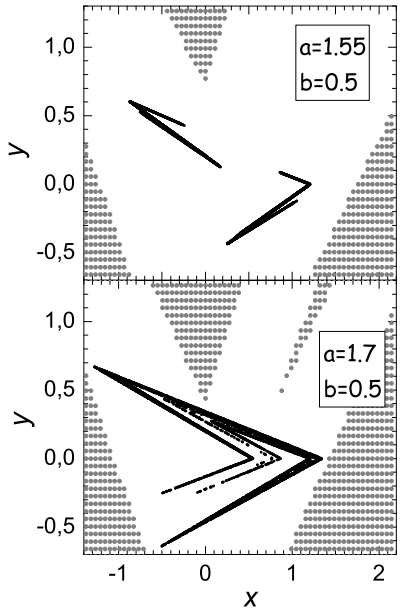

Fig. 4.9 Two strange attractors of the Lozi map for the values a and b specified in the panels. Scales are the same as in Fig. 4.8 what allows to appreciate how the regular attractor with $a = 1.5$ in Fig. 4.8 becomes strange as a increases.

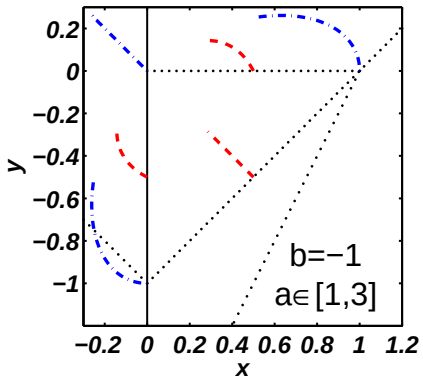

Fig. 4.10 Period-3 border collision in the Lozi map, illustrated as a sequence of snapshots in phase space. The solid line $x = 0$ stands for a border of the map, which is independent of a. The dotted lines represent further borders of the map at $a = 1, b = -1$. For other values of $a \neq 1$ these lines wander across the plot. The dashed and dot-dashed lines stand for the evolution of two different orbits of period-3 as the value of a varies in the interval $[1, 3]$. The border collision takes place at the bifurcation values $a = -b = 1$.

of the neighbouring system $a = 0.9, b = -1$. Fig. 4.12 shows the intricate phase space structure in a larger scale. It is worth noticing that for conservative systems ($|b| = 1$) trajectories fill up densely any window in phase space Thus, to obtain these kind of plots, one has to chose not only a large enough transient but also an adequate number of initial conditions and iterates to be plotted. Otherwise, the plot will hardly reveal inner structures.

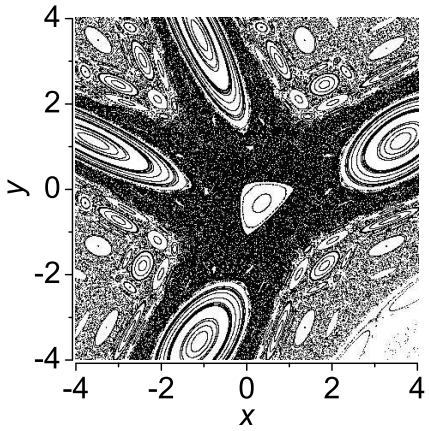

Fig. 4.11 Phase space of the Lozi map for the values $a = 0.9$ and $b = -1$. Notice that the scales are the same as in Fig. 4.1.

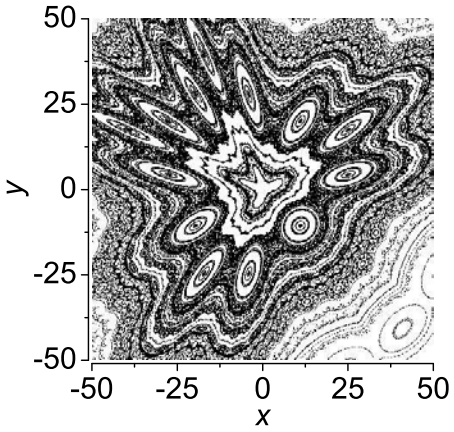

Fig. 4.12 Phase space of the Lozi map for the values $a = 0.9$ and $b = -1$.

4.6 Final comments

In this last section we mention some works related to the Lozi map which have some bearing with our results.

An interesting study of the dynamics of a Hénon–Lozi–type map is carried out in [60]. The authors introduce a C^1 smooth map which depends on a parameter ε. In the limit $\varepsilon \to 0$ their map becomes the Lozi map, and they study which properties are preserved after the limiting procedure. In particular, they point out the interesting result that whereas the smooth Lozi–like map presents a period–doubling route to chaos, the genuine Lozi map does not. This observation buttresses the interpretation advanced in the previous section. Instead of the common infinite sequence of successive period duplications, here we can observe a transition either from period 1 to 2 for $b > 1$, or none for $b < 1$, before entering the chaotic regime with the distinctive feature that at the bifurcation points there is an infinite set of neutrally stable cycles filling a segment, or a sector, in the phase plane.

The theory of border-collision bifurcations provides a classification and a description of the bifurcations caused by the collision of fixed points with boundaries in piecewise maps. This classification is based on the linearized version of the map around the collision point, usually called the *border-collision normal form map* [58]. However, when the normal form is written for the border collisions present in the Lozi map some of the non-degeneracy conditions assumed in the classification theorems do not apply [24]. In particular, the requirements related to the non-singularity of the coefficient matrices of the normal form map are not fulfilled. We refer to appendix A for further mathematical details.

Important explicit results concerning systems with stable periodic orbits embedded in chaos have been reported in the literature. In particular, two works [61, 62] study in depth the area-preserving parameter-free maps

$$x_{n+1} = 1 - y_n \pm |x_n|, \qquad y_{n+1} = x_n, \tag{4.14}$$

The former corresponds to the plus sign above and the latter to the minus sign, which is introduced because some calculations are considerably shorter. These two maps are, except for a reflection transformation ($y \to -y$), Lozi maps with $a = \pm 1, b = 1$. In [62] an infinite set of period-3 cycles, as the lowest period, are found embedded in a sea of chaos. They are essentially the ones we have reported in section 4.3.3. In [61] the analogue set is for orbits of period-6. In both cases further infinite sets of higher periods are studied too.

In this chapter we have revisited the two-dimensional Lozi map with the purpose of showing that it presents what we have called bisecting bifurcations: those which are mediated by an infinite set of neutrally stable periodic orbits. We have determined explicitly the location of some of them as well as their cycle elements. We have also provided an explanation for their existence in both algebraic and geometric terms. We think that particular analyses, like the one we have carried out for the Lozi map, may help to enhance our knowledge about the dynamics of piecewise continuous maps.

Appendix A
Bisecting bifurcations and Border-Collision bifurcations

We study in detail the relation between the bisecting bifurcations described for the VGH and Lozi maps and border-collision bifurcations. We show how these represent special cases not considered in the current Border-Collision bifurcation classification schemes.

Similarly to the classification of bifurcations for continuous maps (see Introduction), the classification of border-collision bifurcations starts by linearizing the map around the collision point. The piecewise affine approximation of the map in the neighbourhood of the border is called the normal form map.

For one-dimenasional piecewise smooth continuous maps the normal form is given by [29]

$$G_1(x;\mu) = \begin{cases} ax+\mu, & x \leq 0 \\ bx+\mu, & x > 0 \end{cases} \tag{A.1}$$

where the parameters have been defined such that the border collision occurs when $\mu = 0$. The different bifurcations are classified in terms of the parameters a and b. However, the current classifications leave out the cases $|a|, |b| = 1$, which as we shall see correspond to the bisecting bifurcations of the VGH map. For one-dimensional discontinuous maps a similar classification scheme is given in [30].

For n-dimensional maps, the classification is based also on the linear approximation of the map around the collision. We reproduce here the process explained in [24] for the obtention of the normal form in the particular case $n = 2$.

Suppose that, in a neighbourhood $\mathscr{D} \subset \mathbb{R}^2$ of the border, the map is given by

$$f(\mathbf{x};\mu) = \begin{cases} F_1(\mathbf{x};\mu), & H(\mathbf{x};\mu) \leq 0 \\ F_2(\mathbf{x};\mu) & H(\mathbf{x};\mu) > 0 \end{cases} \tag{A.2}$$

where $F_i : \mathbb{R}^2 \times \mathbb{R} \to \mathbb{R}^2$, $i = 1,2$, $H : \mathbb{R}^2 \to \mathbb{R}$, and $\mathbf{x} \in \mathbb{R}^2$. We can define the boundary as the smooth curve given by

$$\Sigma := \{\mathbf{x} \in \mathscr{D} : H(\mathbf{x};\mu) = 0\}. \tag{A.3}$$

We assume the map is continuous across the boundary so

$$F_1(\mathbf{x};\mu) = F_2(\mathbf{x};\mu) \quad \forall \mathbf{x} \in \Sigma. \tag{A.4}$$

Suppose now that a border-collision occurs for $\mu = \mu^*$ at $\mathbf{x} = \mathbf{x}^* \in \Sigma$, and that the Jacobian matrices at each side of the border are not singular and hence, that a piecewise linear approximation can be obtained. We start by making a change of variable

$$\tilde{\mathbf{x}} = \mathbf{x} - \mathbf{x}^*, \tag{A.5}$$

$$\tilde{\mu} = \mu - \mu^* \tag{A.6}$$

in order to find the border-collision at $\tilde{\mu} = 0, \tilde{\mathbf{x}} = \mathbf{0}$. To simplify the notation we drop the tildes in the following. Therefore, the map in the new variables, expanded around the collision point reads

$$g(\mathbf{x};\mu) = \begin{cases} N_1\mathbf{x} + M_1\mu + (O)(||\mathbf{x}^2||, ||\mathbf{x}||\mu, \mu^2), C^\top\mathbf{x} + D\mu \leq 0 \\ N_2\mathbf{x} + M_2\mu + (O)(||\mathbf{x}^2||, ||\mathbf{x}||\mu, \mu^2) \;\; C^\top\mathbf{x} + D\mu > 0 \end{cases} \tag{A.7}$$

where

$$N_i = \frac{\partial F_i}{\partial \mathbf{x}}, \tag{A.8}$$

$$M_i = \frac{\partial F_i}{\partial \mu}, \tag{A.9}$$

$$C^\top = \frac{\partial H}{\partial \mathbf{x}}, \tag{A.10}$$

$$D = \frac{\partial H}{\partial \mu}, \tag{A.11}$$

all evaluated at $\mathbf{x} = \mathbf{0}, \mu = 0$. Neglecting the higher-order terms and assuming the boundary does not depend on μ, we can write the normal form as

$$G_2(\mathbf{x};\mu) = \begin{cases} N_1\mathbf{x} + M\mu, C^\top\mathbf{x} \leq 0, \\ N_2\mathbf{x} + M\mu, C^\top\mathbf{x} > 0 \end{cases} \tag{A.12}$$

Note that continuity for $\mu \neq 0$ implies $M_1 = M_2 = M$. From this normal form, a classification theorem (see [24] and references therein) is proposed in terms of the eigenvalues and characteristic polynomials of N_1 and N_2. However, for this theorem to apply, certain assumptions must hold. In particular, the matrices $(I - N_1)$ and $(I - N_2)$ must be non-singular. As we shall see, in the bisecting bifurcations of the Lozi map, one of these matrices proves to be singular and thus we cannot apply the classification theorem.

A.1 Border-Collision bifurcations in the VGH map

Let us start with the linear version of the VGH map in the continuous case

$$f(z) = \begin{cases} z + 2, & z \leq 0, \\ (1-b)z + 2, & z > 0 \end{cases} \tag{A.13}$$

We know that at $b = 2$, unstable fixed points of the second iterate of the map suffer a border-Collision bifurcation. The second iterate reads

$$f^2(z) = \begin{cases} z + 4, & z \leq -2, \\ (1-b)z + 2(2-b), & -2 < z \leq 0, \\ (1-b)^2 z + 2(2-b), & 0 < z \leq \frac{2}{b-1}, \\ (1-b)z + 4, & z > \frac{2}{b-1}. \end{cases} \tag{A.14}$$

When $b = 2$, the border collisions occur at $z = 0$ and $z = 2$. We will focus in the first one. To obtain the map in the normal form G_1 we start by changing coordinates

$$\tilde{z} = z - 0, \tag{A.15}$$
$$\tilde{b} = b - 2. \tag{A.16}$$

Taking only the pieces of the second iterate around the border of interest, we obtain the map

$$g(z) = \begin{cases} -(\tilde{b}+1)z - 2\tilde{b}, & z \leq 0, \\ (\tilde{b}+1)^2 z - 2\tilde{b}, & z > 0, \end{cases} \tag{A.17}$$

The collision now takes place at $z = 0, \tilde{b} = 0$. Taking the linear approximatio around this point we obtain

$$G(z) = \begin{cases} -z + \mu, & z \leq 0, \\ z + \mu, & z > 0, \end{cases} \tag{A.18}$$

with $\mu = -2\tilde{b}$, which corresponds to the normal form with $a = -1, b = 1$. As we have seen, these values fall out of the current classification of Border-Collision bifurcations of one-dimensional piecewise maps.

A.2 Border-Collision bifurcations in the Lozi map

As in the VGH map case, we will study the border collision of a fixed point of the second iterate of the map

$$L^2(x,y;a,b) = (1 - a|1 - a|x| + y| + bx, b(1 - a|x| + y)) \tag{A.19}$$

which we can write as

$$f(x,y;a,b) = \begin{cases} F_1(x,y) = (1 - a(1 + ax + y) + bx, b(1 + ax + y)), & x \leq 0, \\ F_2(x,y) = (1 - a(1 - ax + y) + bx, b(1 - ax + y)), & x > 0, \end{cases} \tag{A.20}$$

We can check that this map is in fact continuous across the boundary $\Sigma := \{(x,y) \in \mathbb{R}^2 / x = 0\}$. We know that a border collision occurs for $a^* = 1 - b$ at $(x^*, y^*) = (0, \frac{b}{a})$. We therefore change coordinates to

$$\tilde{x} = x - 0, \tag{A.21}$$
$$\tilde{y} = y - \frac{b}{a}, \tag{A.22}$$
$$\tilde{a} = a - (1 - b), \tag{A.23}$$

and obtain the new map

$$f(\tilde{x},\tilde{y};\tilde{a}) = \begin{cases} F_1(\tilde{x},\tilde{y}) = (1 - (\tilde{a} + (1-b))(1 + \tilde{A}) + b\tilde{x}, b(1 + \tilde{A})), & \tilde{x} \leq 0, \\ F_2(\tilde{x},\tilde{y}) = (1 - (\tilde{a} + (1-b))(1 - \tilde{A}) + b\tilde{x}, b(1 - \tilde{A})), & \tilde{x} > 0, \end{cases} \tag{A.24}$$

where

$$\tilde{A} = (\tilde{a} + (1-b))\tilde{x} + \tilde{y} + \frac{b}{\tilde{a} + (1-b)}. \tag{A.25}$$

For this new map, the border-collision bifurcation takes place at $\tilde{x} = \tilde{y} = \tilde{a} = 0$. Dropping the tildes and expanding around this point as explained before, we get the map

$$G_2(x,y;a) = \begin{cases} N_1 \begin{pmatrix} x \\ y \end{pmatrix} + Ma, x \leq 0, \\ N_2 \begin{pmatrix} x \\ y \end{pmatrix} + Ma, x > 0, \end{cases} \tag{A.26}$$

where

$$N_1 = \begin{pmatrix} -(1-b)^2 + b & (1-b) \\ b(1-b) & b \end{pmatrix}, \tag{A.27}$$

$$N_2 = \begin{pmatrix} (1-b)^2 + b & -(1-b) \\ -b(1-b) & b \end{pmatrix}, \tag{A.28}$$

$$M = \begin{pmatrix} -1 \\ -(\frac{b}{1-b})^2 \end{pmatrix}. \tag{A.29}$$

It is straightforward to check that

$$|I - N_2| = 0, \tag{A.30}$$

and therefore we cannot apply the classification theorem for the Border-Collision bifurcation of the Lozi map.

Appendix B
Lyapunov exponents for n-dimensional maps

The estimation of the average Lyapunov exponent for one-dimensional maps is fairly simple as explained in the introduction. For n-dimensional maps, the process is more involved. To calculate the Lyapunov exponents for the two-dimensional Lozi map we followed the approach described in [20] (see also [22]). For the sake of completeness, we will detail the calculation algorithm in this appendix. Other algorithms for the numerical estimation of Lyapunov exponents of maps and flows can be found in [63].

Let's start by assuming f is a map $f : \mathbb{R}^m \to \mathbb{R}^m$ and $\mathbf{v}_0 \in \mathbb{R}^m$ is the initial condition of an orbit. We define U as a unit sphere in $\mathbb{R}^m$ centered in $\mathbf{v}_0$. Near $\mathbf{v}_0$ we can make use of the linear approximation of the map to study how the unit sphere U is deformed under the action of the map. If $J(\mathbf{v}_0)$ is the jacobian matrix of the map, $J(\mathbf{v}_0)U$ will be the ellipsoid resulting of applying the map once. In general, after n iterations we will have an ellipsoid $J_n(\mathbf{v}_0)U$ with m orthogonal axis of longitudes r_k^n ($k = 1,\ldots,m$ and $r_1^n > r_2^n > \cdots > r_m^n$).

The kth Lyapunov number of $\mathbf{v}_0$ is defined as

$$L_k = \lim_{n\to\infty} (r_k^n)^{\frac{1}{n}}, \tag{B.1}$$

and the kth Lyapunov exponent is just

$$\lambda_k = \ln L_k, \tag{B.2}$$

with $\lambda_1 > \lambda_2 > \cdots > \lambda_m$.

As in the simpler case of one-dimensional maps described in the introduction, the largest Lyapunov exponent of a chaotic orbit is positive. To compute numerically the Lyapunov exponent we make use of the chain rule to follow the growth of the ellipsoid

$$J_n U = J(\mathbf{v}_{n-1})J(\mathbf{v}_{n-2})\ldots J(\mathbf{v}_0)U. \tag{B.3}$$

We start with an orthonormal basis $\{\mathbf{w}_1^0,\ldots,\mathbf{w}_m^0\}$ of $\mathbb{R}^m$ which stands for the m orthogonal radius of the unit sphere U. We can now compute a new set of vectors $\mathbf{z}_1,\ldots,\mathbf{z}_m$ as

$$\begin{aligned} \mathbf{z}_1 &= J(\mathbf{v}_0)\mathbf{w}_1^0, \\ &\cdots \\ \mathbf{z}_m &= J(\mathbf{v}_0)\mathbf{w}_m^0. \end{aligned}$$

These vectors lie in the new ellipsoid $J(\mathbf{v}_0)U$ but are not necessarily orthogonal. To find an orthogonal basis spanning the same volume as $J(\mathbf{v}_0)U$ we make use of the Gram-Schmidt orthogonalization procedure

$$\begin{aligned}
\mathbf{y}_1 &= \mathbf{z}_1, \\
\mathbf{y}_2 &= \mathbf{z}_2 - \frac{\mathbf{z}_2 \cdot \mathbf{y}_1}{||\mathbf{y}_1||^2}\mathbf{y}_1, \\
\mathbf{y}_3 &= \mathbf{z}_3 - \frac{\mathbf{z}_3 \cdot \mathbf{y}_1}{||\mathbf{y}_1||^2}\mathbf{y}_1 - \frac{\mathbf{z}_3 \cdot \mathbf{y}_2}{||\mathbf{y}_2||^2}\mathbf{y}_2, \\
&\cdots \\
\mathbf{y}_m &= \mathbf{z}_m - \frac{\mathbf{z}_m \cdot \mathbf{y}_1}{||\mathbf{y}_1||^2}\mathbf{y}_1 - \cdots - \frac{\mathbf{z}_m \cdot \mathbf{y}_{m-1}}{||\mathbf{y}_{m-1}||^2}\mathbf{y}_{m-1},
\end{aligned}$$

where $||\mathbf{y}_i|| = \sqrt{\mathbf{y}_i \cdot \mathbf{y}_i}$ is the euclidian norm of the vector.

To avoid too large or too small numbers we normalize this basis to get again an orthonormal basis $\{\mathbf{w}_1^1, \ldots, \mathbf{w}_m^1\}$ and we save the norms $||\mathbf{y}_i||$ of the vectors since they measure the rate of growth in direction *i* for this iteration. After *n* iterations the quantity

$$\lambda_i \approx \frac{\ln||\mathbf{y}_i^n|| + \cdots + \ln||\mathbf{y}_i^1||}{n} \tag{B.4}$$

is a good estimate of the *i*th largest Lyapunov exponent.

A graphical scheme of the algorithm for a two-dimensional map such as the Lozi map is shown in figure B.1.

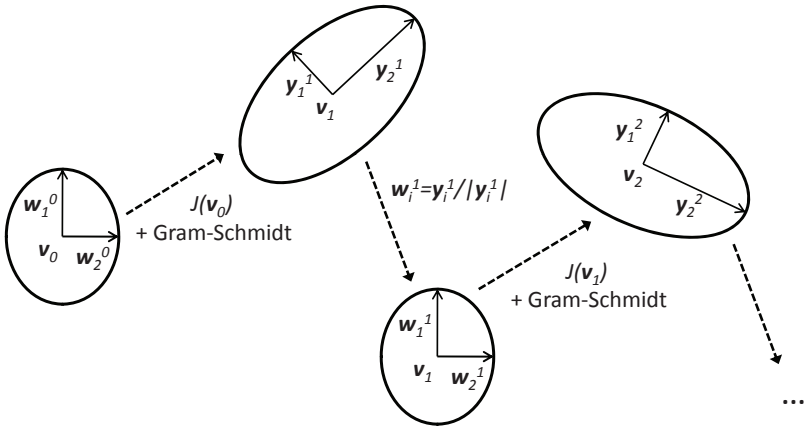

Fig. B.1 Graphical illustration of the numerical algorithm for the estimation of the Lyapunov exponent.

Part II
Adaptive networks and polysynchrony

Chapter 5
Introducció: Sistemes complexos adaptatius

5.1 El concepte de sistema complex

Segurament per tractar-se d'un camp d'estudi relativament nou i fortament multidisciplinari, no existeix encara una definició rigorosa ni universalment acceptada de sistema complex. De fet, el terme *complexitat* s'ha emprat en més d'un àmbit científic per parlar de coses ben distintes [64]. Per aquest motiu sembla convenient definir què s'entendrà per sistema complex en aquesta tesi. Al nostre parer, un sistema complex és aquell sistema composat per un gran nombre d'agents o unitats fonamentals en interacció en el qual apareixen unes propietats dinàmiques o estructurals que no es dedueixen de manera trivial de les lleis d'interacció entre els agents [65]. Posem alguns exemples. La cèl·lula, la unitat bàsica de tot organisme viu, és el sofisticat resultat de milers d'interaccions físiques entre molècules. La nostra experiència conscient és el fruit de les interaccions químiques i elèctriques de bilions de neurones. Encara en una altra escala, insectes socials com les formigues o les abelles prenen decisions col·lectives, com ara on construir el niu, a través d'un procés autoorganitzat del qual emergeix la decisió espontàniament. En cadascun d'aquests casos conèixer la llei d'interacció entre els agents (molècules, neurones, etc.) no ens permet entendre millor o deduir fàcilment la varietat de fenòmens que ocorren quan molts d'ells interaccionen simultàniament.

A l'hora d'afrontar l'estudi d'aquests sistemes es fan servir els coneixements adquirits en disciplines ja existents com ara la dinàmica no lineal, la física estadística, la teoria de jocs o la teoria de xarxes.

En aquesta part de la tesi exposarem un model teòric concret de sistema complex adaptatiu que presenta noves propietats emergents en termes de la sincronització dinàmica dels seus elements. És necessari però, introduir abans alguns conceptes com ara el de xarxa complexa o el de sincronització.

5.2 Xarxes complexes i sistemes discrets acoblats

Una manera adient de modelitzar o entendre un sistema complex és mitjançant una xarxa o graf. En una xarxa, els agents es representen com a nodes de la xarxa i les interaccions entre ells com els enllaços o fletxes (segons si el graf és dirigit o no) (Figura 5.1).

La teoria de grafs existeix des de molt abans que es parlés de sistemes complexos [66]. Concretament, es situen els inicis de l'estudi dels grafs en la resolució per part de Leonhard Euler (1707-1783) del famós problema dels set ponts de Königsberg (actualment Kaliningrad, Rússia) l'any 1735. En la segona meitat del segle XX la teoria de grafs

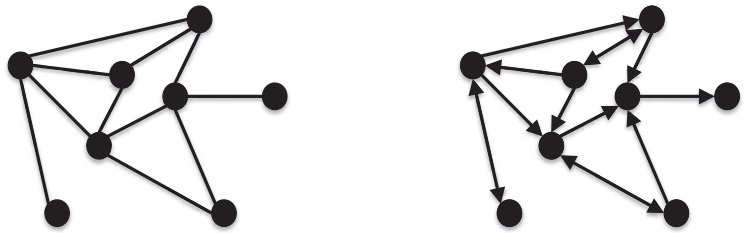

Figura 5.1 Exemples de xarxa no dirigida (esquerra) i dirigida (dreta).

va rebre una renovada atenció arran del famós experiment del psicòleg Stanley Milgram (1933-1984) sobre els "sis graus de separació" en xarxes socials [67] i sobretot des que la introducció dels ordinadors va permetre treballar fàcilment amb grafs composats per un gran nombre de nodes i estudiar les propietats estadístiques d'aquests. A finals de la dècada de 1990 s'estableix el camp de les xarxes complexes amb l'aparició de dos treballs sobre els fenòmens de xarxes de món petit (nom motivat per l'experiment de Milgram) [68] i xarxes lliures d'escala [69]. Aquests primers estudis se centren principalment en les propietats estructurals de les xarxes (la distribució de grau, la distribució de pesos, la longitud promedi del camí entre dos nodes, etc.), en una identificació o classificació de les xarxes a partir d'aquestes propietats i en la creació o evolució dinàmica d'aquestes estructures mitjançant uns certs algorismes [70]. Amb la intenció d'acostar el camp de les xarxes complexes a la modelització de la dinàmica de sistemes complexos, apareixen models en els quals s'associa una certa dinàmica als nodes d'una xarxa complexa i es defineix una llei d'acoblament entre els nodes connectats per un enllaç [71]. A continuació expliquem amb més detall alguns aspectes d'aquests models en relació amb el fenomen de la sincronització.

5.3 Sincronització i polisincronia

Potser un dels fenòmens més estudiats en el camp dels sistemes complexos és el de sincronització. La sincronització es defineix com l'ajust dels ritmes de dos sistemes oscil·lants (no lineals, en general) degut a una interacció (dèbil i no lineal, en general) entre ells [72] . La primera observació del fenòmen de sincronització s'atribueix al científic holandès Christiaan Huyguens (1629-1695). Huyguens observà que dos rellotges de pèndol que penjaven d'una barra de fusta, modificaven les seues oscil·lacions fins que ambdós pèndols oscil·laven a l'uníson.

La descripció matemàtica de la sincronització en poblacions d'oscil·ladors no lineals va començar al s. XX degut en gran part al descobriment de sistemes naturals que presentaven aquest curiós fenòmen i a la recentment adquirida capacitat de càlcul numèric que permetia simular sistemes amb un gran nombre d'oscil·ladors (per a una història detallada dels inicis d'aquest camp recomanem [73]).

El fet que alguns d'aquests sistemes estiguen formats per un gran nombre d'oscil·ladors en interacció fa que entren dins la nostra definició de sistema complex, donat que la sincronització és una propietat emergent d'aquests. La dinàmica dels oscil·ladors i la natura de la interacció pot variar fortament i tanmateix la sincronització apareix com

a solució en tots ells. Açò dóna un caràcter d'universalitat a la sincronització com a propietat emergent típica dels sistemes complexos.

Els primers models matemàtics de sincronització en grups d'oscil·ladors assumien que cada oscil·lador interaccionava amb tota la resta del grup. El model paradigmàtic és l'introduït per Kuramoto [74, 75] per a N oscil·ladors de fase

$$\dot{\theta}_i = \omega_i + \sum_{j=1}^{N} \frac{K}{N} \sin(\theta_j - \theta_i), \quad i = 1, \ldots, N \tag{5.1}$$

on θ_i representa la fase de l'oscil·lador i i el paràmetre K és la constant d'acoblament que regula la intensitat de la interacció.

També s'han estudiat models de sistemes discrets acoblats de la següent forma

$$x^i_{n+1} = f(x^i_n) + \frac{\varepsilon}{N} \sum_{j=1}^{N} h(x^i_n, x^j_n), \quad i = 1, \ldots, N, n \in \mathbb{N} \tag{5.2}$$

on $h(x^i_n, x^j_n)$ és la funció d'acoblament i ε la constant d'acoblament. En el cas dels sistemes discrets sí que s'hi va introduir una certa noció d'espai en estudiar l'acoblament en xarxes regulars (*coupled map lattice*) de manera que cada node sols interacciona amb els seus veïns [76].

De tota manera, en aquests model la topologia de la xarxa d'interaccions no juga cap paper important donat que la interacció és igual per a tots els oscil·ladors (cada oscil·lador interacciona amb tota la xarxa o en el cas de la xarxa regular, tots els oscil·ladors interaccionen amb el mateix nombre de veïns). Per tant, el següent pas lògic en el camí cap a models més realistes fou l'utilització de xarxes complexes per modelitzar l'estructura de les interaccions entre oscil·ladors. És a dir, ara cada oscil·lador és un node en una xarxa i interacciona sols amb aquells nodes amb els quals està connectat pels enllaços de la xarxa. L'interès en aquest cas és entendre com afecta la topologia de la xarxa a la dinàmica de sincronització [77]. Entre els fenòmens descoberts en aquest camp volem destacar-ne un que tindrà especial protagonisme en aquesta part de la tesi: la polisincronia.

La polisincronia és una forma de sincronització en una xarxa en la qual grups de nodes se sincronitzen sense estar directament connectats [78, 79, 80, 81, 82]. Aquest fenomen s'ha estudiat per a topologies fixes o estàtiques i s'ha demostrat que la capacitat d'una xarxa per mostrar patrons de polisincronia depèn sols de la seua topologia i no de la dinàmica concreta dels seus nodes. El principal teorema sobre polisincronia estableix que podrem trobar polisincronia en una xarxa si podem dividir els nodes en classes d'equivalència de manera que nodes en la mateixa classe reben enllaços equivalents (per veure la formulació formal d'aquest teorema consultar [78]). Aquest teorema s'entén millor amb l'ajuda gràfica de la Fig. 5.2. En la Fig.5.2**A.** es mostra un exemple de xarxa de set nodes amb tres tipus d'interacció o enllaç entre els nodes. Per tal que aquesta xarxa presente polisincronia hem de poder dividir els seus nodes en classes d'equivalència amb el mateix conjunt d'enllaços entrants (mateix *input*). És evident que sempre existeix una solució trivial a aquest problema en la qual hi ha tantes classes d'equivalència com nodes té la xarxa. No obstant, en l'exemple que hem triat trobem una solució no trivial que ens permet dividir la xarxa en tres classes d'equivalència (Fig. 5.2**B.**). A la Fig. 5.2**C.** es mostren els enllaços que reben tots els nodes de cadascuna de les classes d'equivalència. El teorema de la polisincronia estableix per tant que, independentment de la dinàmica

que imposem als nodes, existeix una solució estable per a la dinàmica en la xarxa en la qual, la dinàmica dels nodes dins de cada classe d'equivalència està sincronitzada.

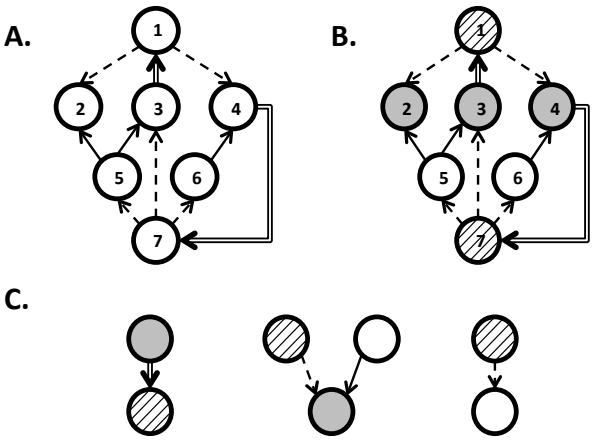

Figura 5.2 **A.** Exemple de xarxa o graf amb tres tipus distints d'enllaç. **B.** Divisió dels nodes de la xarxa en classes d'equivalència ($\{1,7\},\{2,3,4\},\{5,6\}$) segons els enllaços d'entrada o *input*. **C.** Classes d'equivalència de l'exemple amb els enllaços d'entrada corresponents.

5.4 Xarxes complexes adaptatives

Parlem de xarxes complexes adaptatives quan la topologia o estructura de la xarxa canvia amb el temps influenciada per la dinàmica local dels seus nodes [83, 84]. En aquests casos es crea una interacció de doble sentit entre l'estructura i la dinàmica que permet l'aparició de nova fenomenologia.

El concepte de xarxa complexa adaptativa ha estat introduït inspirat per un seguit de sistemes reals com ara xarxes neuronals on la força de les connexions sinàptiques varia segons l'activitat de les neurones [85, 86], propagació d'epidèmies on la xarxa d'interaccions socials varia segons l'estat de cada node (infectat o no, en el cas més senzill) [87, 88, 89] o inclús models de formació d'opinions on aquesta mateixa xarxa varia segons les opinions dels nodes [90, 91].

En aquesta part de la tesi introduïm un model de xarxa complexa adaptativa en el qual la dinàmica dels nodes ve donada per un sistema discret caòtic semblant als descrits en els primers capítols de la tesi i on els nodes varien l'estructura dels seus enllaços seguint un principi *homofílic*: els nodes busquen estar connectats a nodes en estats dinàmics semblants. Aquest model presenta propietats emergents mai observades abans en un model de xarxa complexa adaptativa. La condició inicial per a l'estructura de la xarxa és de connectivitat total i evoluciona cap a estructures jeràrquiques que poden presentar, per a un ampli rang de paràmetres, patrons de polisincronia (Fig. 5.3).

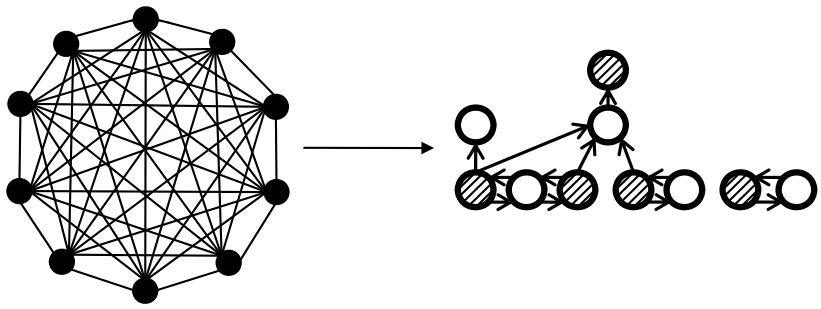

Figura 5.3 Il·lustració gràfica del model de xarxa adaptativa que estudiem al capítol 6. Començant des d'una condició inicial amb nodes indistingibles connectats tots amb tots l'algorisme d'evolució adaptativa transforma la xarxa, per a certs valors del paràmetre, en una xarxa que presenta polisincronia.

Chapter 6
Polysynchrony in adaptive networks

6.1 Introduction

Networks allow us to model a huge variety of complex systems where a multitude of agents dynamically interact [92, 93]. The agents are modeled as nodes and the links of the network stand for their interactions. When the dynamics of the agents can affect the pattern of interactions, i.e. change the structure of the network, we speak of complex adaptive networks [83, 84]. These networks can show a variety of dynamical and structural properties depending on the dynamics of the agents, the nature of the interaction or the adaptation mechanism [94, 95, 96, 97, 98, 99, 100, 101, 102]. Adaptive networks have been studied for their own interest and also as models for real systems such as the electric transportation network [103], epidemic dynamics [87, 88, 89], socioeconomic networks [104], consensus formation [90, 91], neural networks [105, 106] and functional brain networks [85, 86]. In these models the asymptotic dynamics and underlying graph can be seen as an emergent property of the system, and may provide mechanisms to explain the evolution of certain types of graph.

The dynamics of these systems can be rich, both in terms of the temporal dynamics at the nodes and the emergence of topological structure in the networks. For example, the dynamics can synchronize, so all nodes behave asymptotically in the same way [72]. Polysynchrony describes a more subtle form of synchronization [78, 79, 80, 81, 82] where groups of nodes can be synchronized and, unlike cluster synchronization, synchronized nodes need not be connected to each other.

In this chapter we show that complicated polysynchronous dynamics can emerge in adaptive networks using a simple homophilic principle to determine the evolution of the links of the network. This is based on the idea that nodes 'like' being connected to similar nodes, a common assumption in many socially motivated networks and a basic principle in neural network dynamics. In other words, we consider a collection of identical individuals operating under the same homophilic rules, and show that the system evolves to a state in which the connections no longer change with time (we call this a frozen state) with a finite number of connected components, each of which can display polysynchronous dynamics. To the best of our knowledge, polysynchrony has not been previously identified in an adaptive system. Moreover, all the examples we have looked at have a further interesting property: the final states have graphs which have a hierarchical structure, with a group of strongly connected components at the bottom, and then the remaining nodes being arranged above these (taking information from them, but not giving information) in levels reflecting the number of directed links needed to get to the node from one of the bottom nodes or 'roots'. (Note that we say a set of nodes is *strongly*

connected if there is a path in the graph following the directed edges or arrows between any two nodes, and *connected* if there is a path between any two nodes following edges, so the path can use an edge in the opposite direction to the arrow.) This suggests that polysynchrony and hierarchy are natural states that can emerge from simple undifferentiated networks over time.

Apart from polysynchrony, this model shows other dynamical regimes that will also be described in this chapter. Furthermore, we explain these different regimes through the analytical study of the stability of the different attractors or synchronized states. The structure of the chapter is as follows. In section 6.2 we introduce our model. In section 6.3 we show that the network topology reaches a frozen state where the rewiring stops and we study the final network structure. The transient times to the frozen state are evaluated as a function of the network size and the coupling strength. In section 6.4 the different dynamical regimes are described in terms of the synchronization of the nodes. In section 6.5 we provide several examples of polysynchronous networks and study the probability of finding polysynchrony as a function of the coupling strength. In section 6.6 we summarize and discuss the main results of this work and their potential applications. In two separate appendices we provide a detailed stability analysis of the fully synchronous and polysynchronous states.

6.2 The model

The model consists of a directed network of N nodes. The dynamics of the ith ($i = 1,\ldots,N$) node are given by

$$x_{n+1}^i = f(x_n^i) + \frac{\varepsilon}{m}\sum_{j=1}^{N} A_n^{ij}(f(x_n^j) - f(x_n^i)) \tag{6.1}$$

where we choose f to be the fully-chaotic logistic map $f(x) = 4x(1-x)$ and A_n is the adjacency matrix of the network at time step n, so $A_n^{ij} = k$ if there are k connections (directed edges) from j to i, with the direction indicated by the arrow in the accompanying figures. Each node is assigned a fixed number m of incoming links so

$$\sum_{j=1}^{N} A_n^{ij} = m, \tag{6.2}$$

and we choose $m = N-1$ throughout this chapter. It is clear from (6.1) that at each iteration the ith node is influenced by the dynamics of these m nodes to which it is connected by an incoming arrow. We will call these nodes the *neighbours* of node i. These links can be rewired at each iteration following an adaptation algorithm that we describe next.

At each iteration n we compute the distance matrix D_n^{ij}

$$D_n^{ij} = \begin{cases} |f(x_n^i) - f(x_n^j)|, & A_n^{ij} \neq 0 \\ 0, & A_n^{ij} = 0 \end{cases} \tag{6.3}$$

and calculate from it the mean distance of a node to all its neighbours

$$\langle D\rangle_n^i = \frac{1}{a_n^i}\sum_{j=1}^{N} D_n^{ij} \tag{6.4}$$

where a_n^i is the unweighted number of neighbours of node i at time step n, i.e. the sum over j of $\text{sign}(A_n^{ij})$.

For the rewiring we apply a homophilic principle: nodes prefer to be connected to nodes being in a similar state. We identify the *bad* neighbours $j \in \mathscr{B}_n^i$ of each node i at iteration n with the following criterion

$$j \in \mathscr{B}_n^i \quad \text{if} \quad D_n^{ij} > \langle D\rangle_n^i, \tag{6.5}$$

so a neighbour j is considered *bad* if its distance D_n^{ij} to node i is larger than the average distance of the neighbourhood $\langle D\rangle_n^i$. The *good* neighbours of node i are then given by

$$\mathscr{G}_n^i = \{1,\ldots,N\}\setminus\left(\mathscr{B}_n^i \cup \{i\}\right), \tag{6.6}$$

so $i \notin \mathscr{G}_n^i$ which, as we shall see, means that a node never becomes linked to itself. Once the good and bad neighbours have been identified node i will break the links coming from $\mathscr{B}_n^i$ and randomly rewire them to nodes in $\mathscr{G}_n^i$. Let b_n^i be the number of *bad* neighbours

$$b_n^i = \sum_{j\in\mathscr{B}_n^i} A_n^{ij}. \tag{6.7}$$

Now choose b_n^i elements of $\mathscr{G}_n^i$ at random and suppose that r_n^{ik} is the number of times node k is chosen. The adjacency matrix at the next time step is then

$$A_{n+1}^{ik} = \begin{cases} 0, & k \in \mathscr{B}_n^i \\ A_n^{ik} + r_n^{ik}, & k \in \mathscr{G}_n^i \end{cases}. \tag{6.8}$$

In all the cases we describe the initial connectivity has been chosen as the symmetric all-to-all connectivity where each node in the network is connected to all the possible $m = N-1$ neighbours and $A_0^{ii} = 0$.

6.3 Asymptotic network topology

The first main observation is that, contrary to other models of adaptive networks of chaotic maps [94, 95], in this model the network reaches a frozen or absorbing state where the rewiring stops for all values of $\varepsilon \in [0,1]$. This allows us to study the final topology and dynamics of the network as a function of the parameters.

The existence of the frozen state is partly explained by the rewiring mechanism chosen. If, for instance, a node i receives all its incoming links from one single neighbour k at some iteration n', then $\langle D\rangle_n^i = D_n^{ik}$ and $\mathscr{B}_n^i = \emptyset\ \forall n > n'$. Therefore i will remain locked to this neighbour and never activate again the rewiring mechanism. This is, however, the simplest case of locking. As we explain below, nodes can also lock to more than one node.

The duration of the transient to the frozen state increases exponentially with the system size N (Fig. 6.1) but depends greatly on the value of ε (Fig. 6.2). The dependence of the transient length on the coupling constant is a sign of the influence of the dynamics in the rewiring and freezing processes. The exponential increase of the transient time

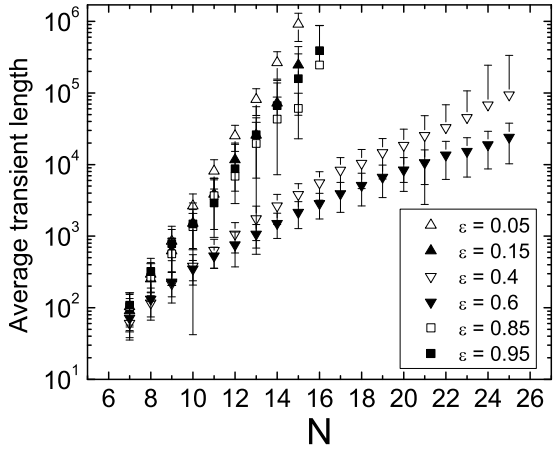

Fig. 6.1 Average transient length as a function of the system size N for different values of the coupling constant ε. The average is calculated over 500 realizations of the system. The frozen state is identified when the network topology remains constant for 10^4 iterations.

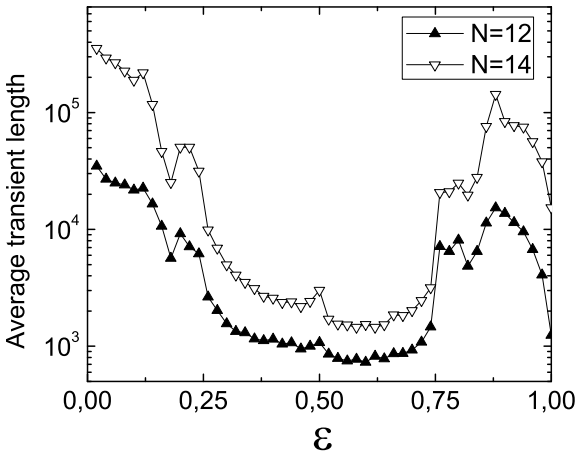

Fig. 6.2 Average transient length as a function of the coupling constant ε for different values of the system size N. The average is calculated over 100 realizations of the system. The frozen state is identified when the network topology remains constant for 10^4 iterations.

with the system size is similar to that described in [107] for the case of a coupled map lattice with diffusive coupling although the definition of the transient is different (in the lattice case the topology is fixed and the transient is defined as the time it takes to reach a certain attractor).

In Fig. 6.3 we show six examples of final topologies of a network of $N = 10$ nodes for different values of ε. The most clear feature of these network examples is the strong hierarchical structure. This model does not allow a tree structure as a final topology since all nodes have input links and therefore the network will have at least one cycle. However, the structure is very close to the hierarchy of a tree structure if we consider strongly connected components of the network as *roots*. Inspired by the definitions of 'trophic level' and 'trophic height' introduced in [108] for the study of food webs, we

can define the 'level' of a node as the minimum (directed) path length from the root to the node and the 'height' of a node as the average distance over all possible directed paths from the root to the node. We say a network is strongly hierarchical if level and height coincide for all the nodes in the network. We can see that following this definition all the topologies shown in Fig. 6.3 are strongly hierarchical.

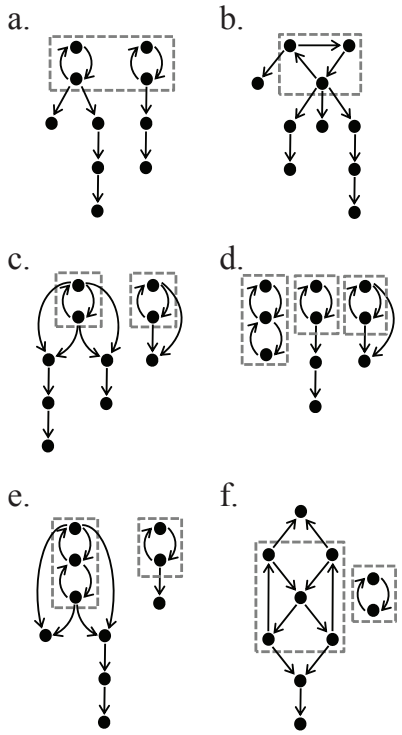

Fig. 6.3 Examples of the final network topology ($N = 10$). The values of the coupling constant are: $\varepsilon = 0.1$ in **a.** and **b.**; $\varepsilon = 0.4$ in **c.**; $\varepsilon = 0.6$ in **d.**; $\varepsilon = 0.8$ in **e.**; $\varepsilon = 0.95$ in **f.**

Interestingly, the observation of these topologies also allows us to deduce some characteristics of the dynamics on the network. In examples **a.** and **b.** ($\varepsilon = 0.1$) all nodes are locked to one single neighbour. On the contrary, in the rest of the examples in the figure we find nodes with inputs coming from two different neighbours. As we shall see in the following sections, this is only possible if these two nodes are synchronized: when a node i has only two neighbours j,k and these are synchronized in the same orbit ($x_n^k = x_n^t, \forall n$), then $D_n^{ij} = D_n^{ik} = \langle D \rangle_n^i \quad \forall n$ and the node remains locked to its neighbourhood.

The synchronization on the network is regulated almost entirely by the synchronization dynamics of the strongly connected components. This is somehow intuitive since only in these components we find closed loops of mutually influencing nodes. We study this dynamics on the following section and on the appendices of this part of the thesis. For the moment we are interested in which strongly connected components are more frequent in the final topologies as a function of ε. In Fig. 6.4 we show the probability that a node belongs to a strongly connected component of a certain size as a function of ε. As could be already appreciated in Fig. 6.3, the most common strongly connected components are pairs and triplets except in the region of large ε ($\varepsilon > 0.9$) where bigger strongly connected components are possible.

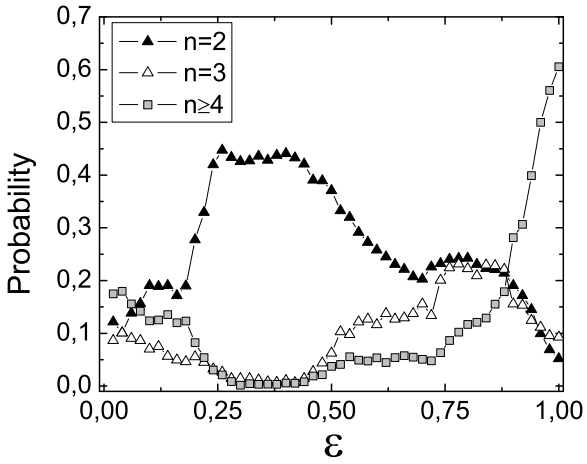

Fig. 6.4 Probability of a node being in a strongly connected component of size n calculated over 500 initial conditions for each value of ε.

6.4 Dynamics

We study now the dynamics in the final network as a function of the coupling constant. Our main interest is to see if any nodes in the network synchronize their dynamics and how they do it. It is important to keep in mind that the dynamics of an isolated node is given by the fully-chaotic logistic map and therefore, it would be chaotic on the interval $[0,1]$.

To measure the synchronization of nodes we find it useful to define the matrix

$$\beta^{ij} = \theta(\frac{1}{\tau}\sum_{n=n'}^{n'+\tau}|x_n^i - x_n^j|) \tag{6.9}$$

where $\theta(x)$ is the Heaviside step function and n' is a long transient that we allow in order to be sure the network has frozen and the dynamics have stabilized. The element β^{ij} is equal to zero if the trajectories of nodes i and j are fully synchronized ($x_n^i = x_n^j$) during τ iterations after the transient and is equal to one otherwise.

We can now define a measure of full synchronization of the network as

$$\alpha = 1 - \frac{1}{N(N-1)}\sum_{\substack{i,j \\ i\neq j}}\beta^{ij}. \tag{6.10}$$

This measures the percentage of synchronized pairs of nodes (connected or not) over the total number of pairs. If $\alpha = 1$ all nodes in the network are synchronized in the same trajectory while if $\alpha = 0$ no two nodes in the network are synchronized.

Since our network can split in several disconnected components and each connected component could be fully synchronized in a different trajectory, we introduce a second quantity to take this into account and measure the synchronization only between pairs of connected nodes. We can thus define the connected component synchronization as

$$\alpha_C = 1 - \frac{1}{|C|}\sum_{(i,j)\in C}\beta^{ij} \tag{6.11}$$

where C is the set of pairs of connected nodes and $|C|$ is the cardinality of this set.

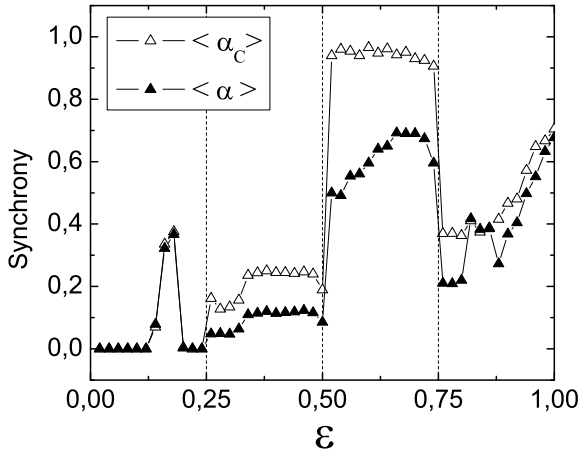

Fig. 6.5 Averages over 500 initial conditions of the synchrony measures α and α_C as a function of the coupling parameter ε. The frozen state is identified when the network topology remains constant for 10^4 iterations. Parameters: $N = 10$, $\tau = 10$, $n' = 10^4 - \tau$.

The values of α and α_C as a function of ε are shown in Fig. 6.5. To explain the different regimes in this figure it is very useful to study first the dynamics of the most common small strongly connected components such as the strongly connected pair, the triplet with transposition symmetry and the 3-cycle shown in Fig. 6.6. Since these act as *roots* from which the rest of the network take input, the dynamics of these components is what determines the behaviour of the rest of the nodes. In Appendix C we detail the stability analysis of the synchronous states of these components. Here we will only report the results that are of interest for the discussion.

The lyapunov exponent of the fully-chaotic logistic map ($r = 4$) is $\lambda = \ln 2$. Substituting this in (C.3) we find that the synchronous chaotic state of the strongly connected pair is stable in the interval $0.25 < \varepsilon < 0.75$. Similarly, the triplet with transposition symmetry (C.6) has a stable synchronous state if $0.5 < \varepsilon < 0.75$. On the contrary, when $r = 4$ the 3-cycle (C.8) has no stable synchronous state. Another important fact is that a node locked to a synchronized set of nodes (all following an orbit of the uncoupled logistic map), as in (C.12), will synchronize to them if $\varepsilon > 0.5$. These results render much more easy the interpretation of Fig. 6.5 and are shown schematically in Fig. 6.7. The change of regime at $\varepsilon = 0.25$ is thus explained by the strongly connected pairs becoming synchronized. Also, in Fig. 6.4 we can see that the probability of finding pairs in the final network increases accordingly. At $\varepsilon = 0.5$ the synchronized state of the triplet with transposition symmetry becomes stable. This is likely to be the cause of the corresponding increase of the probability of being in a strongly connected component of size $n = 3$. Moreover, as we have seen, for $\varepsilon > 0.5$ a node locked to a synchronized pair or triplet will become synchronized with it. Due to the hierarchical structure of the networks, this opens the possibility for the whole network to synchronize in the same orbit and is reflected by a sudden increase in the amount of synchrony in the networks (Fig. 6.5). For $\varepsilon > 0.75$ both the pair and the triplet lose the stability of their synchronized states. However, we can see that in the parameter ranges $0.12 \lesssim \varepsilon \lesssim 0.2$ and $\varepsilon > 0.75$, although none of the most common strongly connected components have a stable synchronous state, there is

a considerable amount of synchronized nodes in the final networks. Interestingly, this is partly caused by the phenomena of polysynchrony that we explain in detail in the next section.

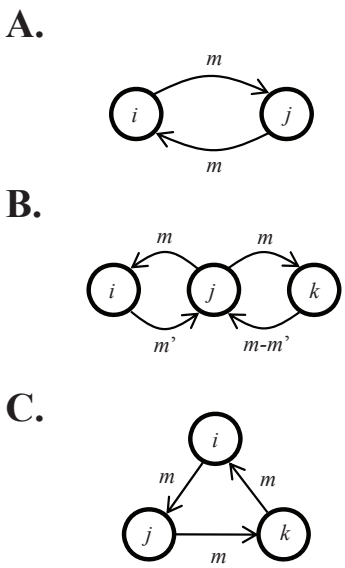

Fig. 6.6 **A.** Strongly connected pair (2-cycle). **B.** Triplet with transposition symmetry. **C.** 3-cycle. In all the cases the labels of the links stand for their weights (m is the maximum value given by (6.2) and $m' \leqslant m$)

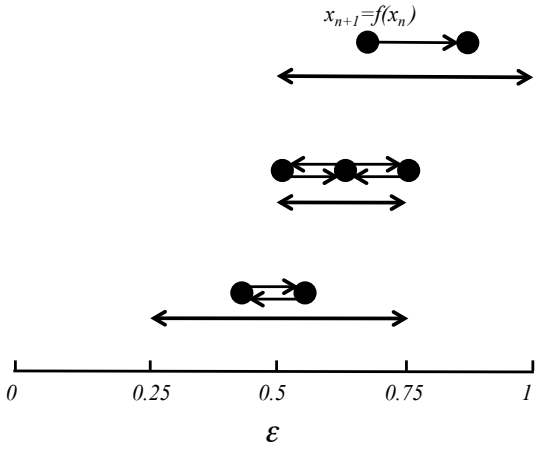

Fig. 6.7 Schematic representation of the regions of stability of the full synchronization state for the strongly connected pair, the triplet with transposition symmetry and the case of unidirectional coupling when the influencing node follows an orbit of the logistic map.

6.5 Polysynchrony

As we have explained in the introduction polysynchrony defines the situation when the dynamics of the network nodes breaks up into a small number of disconnected sets where the dynamics is synchronous. As opposed to full or cluster synchronization, in the case of polysynchrony, the synchronized nodes are not directly connected.

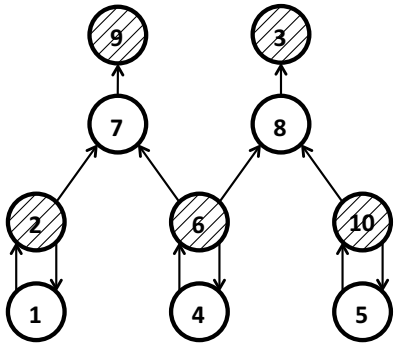

Fig. 6.8 Example of polysynchronous network for $\varepsilon = 0.85$. Nodes filled with the same pattern are synchronous. In this case each synchrony class is attracted to a different fixed point.

We illustrate now the phenomenon of polysynchrony in our model with several examples from the simplest case of fixed point dynamics to more involved examples of quasiperiodic and chaotic polysynchronous dynamics. In Fig. 6.8, for $\varepsilon = 0.85$, we find that each synchrony class has a fixed point as the final attractor. These fixed points correspond to the fixed point dynamics of the strongly connected pair since the root of the network in this example is composed of three strongly connected pairs. In fact, for most of the examples of polysynchrony provided, the quotient system of the network (basically a reduced network where each synchrony class is represented by a single node with the same input) reduces to a strongly connected pair. Therefore, the available dynamics are those of the strongly connected pair (see Fig. 6.9).

For $\varepsilon = 0.18$, in Fig. 6.10 we find an instance of a network with polysynchronous period-2 dynamics. The dynamics is divided into two synchrony classes following the same period-2 orbit in antiphase. Since for a given ε the dynamics of all pairs is the same, the nodes of a pair are synchronous with the corresponding nodes of the other pair.

In Fig. 6.11 (for $\varepsilon = 0.861$), the network has divided into two separate clusters. In one of them the dynamics of the nodes is quasiperiodic while in the other it is periodic with period 3. Both clusters have a triplet with transposition symmetry as a root. As in the previous examples no two synchronized nodes are connected and all nodes with equivalent inputs are synchronized. Although the two clusters have different dynamics, their quotient systems are strongly connected pairs and therefore, both the period-3 and the quasiperiodic orbit are attractors of the strongly connected pair (see Fig. 6.9) when $\varepsilon = 0.861$.

Another example of strongly hierarchical polysynchronous network is shown in Fig. 6.12 where the root is composed of two strongly connected pairs. This example has the additional interest that different synchrony classes inside the same cluster show different dynamical behaviour. While the root pairs $\{5, 10\}$ and $\{4, 6\}$ follow a period-2 cycle, the rest of the nodes in the network show period-4 dynamics. Moreover, it is inter-

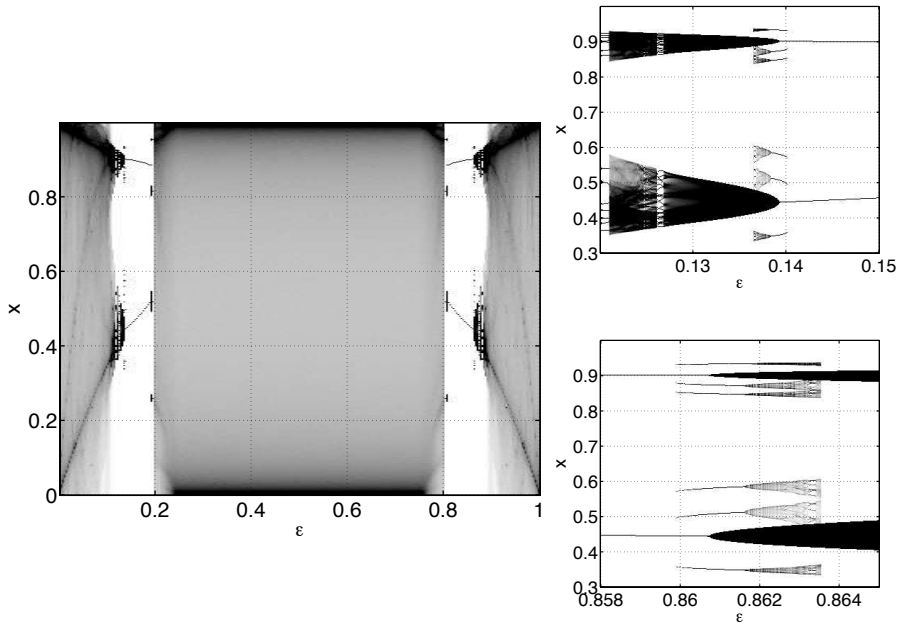

Fig. 6.9 Bifurcation diagrams as a function of ε for the system of two coupled fully-chaotic logistic maps (C.3). The right panels show details of the full bifurcation diagram.

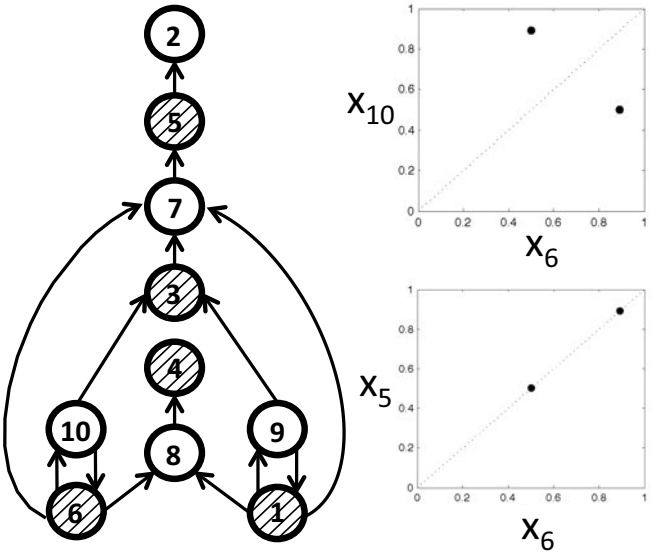

Fig. 6.10 Example of polysynchronous network for $\varepsilon = 0.18$. Nodes filled with the same pattern are synchronous. The dynamics of the synchrony classes is periodic with period 2. Nodes in different classes oscillate in antiphase.

esting to note that nodes in classes $\{4,5\}$ and $\{1,3,8,9\}$ all receive the same input (from class $\{6,10\}$) but show different dynamics. This illustrates that having equivalent inputs is only a necessary but not sufficient condition to be in the same synchrony class [109].

This particular case is more involved because we find here an instance of route-to-chaos in an open flow similar to that described in [110, 111, 112, 113]. In Fig. 6.13 we observe the prototypical open flow system, consisting of a chain of unidirectionally coupled maps. In this case the system is closed on one side by a strongly connected pair. The period-2 orbit of the pair for $\varepsilon = 0.14$ is fed into the chain as a fixed boundary con-

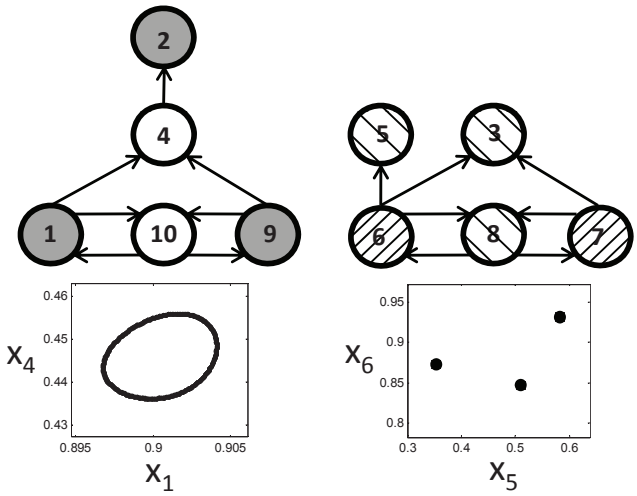

Fig. 6.11 Example of polysynchronous network for $\varepsilon = 0.861$. Nodes filled with the same pattern are synchronous. The nodes in the left cluster follow quasiperiodic orbits while the nodes in the right cluster follow period-3 orbits.

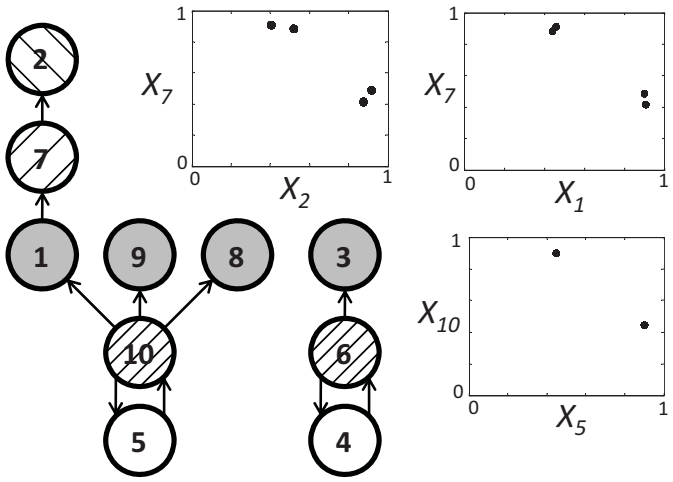

Fig. 6.12 Example of polysynchronous network for $\varepsilon = 0.14$. Nodes filled with the same pattern are synchronous. In this case there are 4 different synchrony classes showing 2 different dynamical behaviours: $\{4,5\}$ and $\{6,10\}$ are synchronized in a period-2 cycle while $\{2\}$,$\{7\}$ and $\{1,3,8,9\}$ show period-4 dynamics.

dition and we observe a spatial period-doubling bifurcation. Therefore, what we observe in Fig. 6.12 is merely the beginning of this route-to-chaos.

Fig. 6.14 shows an example of polysynchronous network for $\varepsilon = 0.78$ where the dynamics of the nodes is chaotic. It is important to note that the synchronized trajectories do not correspond to trajectories of the uncoupled logistic map. If this were the case, as we have explained before nodes 7 and 9 would synchronize to nodes 2 and 3 since the synchronous state of the unidirectional coupling is stable for $\varepsilon > 0.5$.

In Fig. 6.15 we show the probability of finding polysynchrony in the network as a function of the coupling constant ε. As we have already detected in the study of synchrony in Fig. 6.5, there are two intervals of coupling strength values for which polysynchrony is possible.

The regions of polysynchrony in Fig. 6.15 can be better understood by studying the stability of the different polysynchronous dynamics. In Appendix D we study the sta-

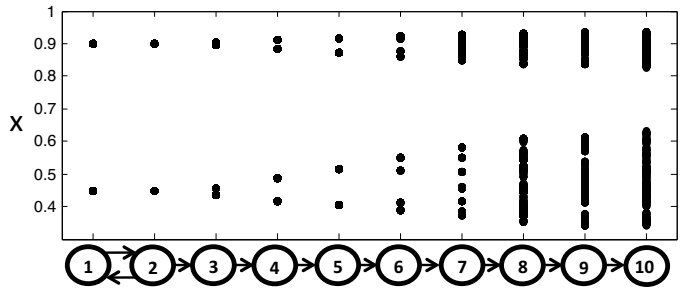

Fig. 6.13 Example of network similar to an open flow system with a strongly connected pair at one end that forces the system with a period-2 orbit. We can see how the dynamics of the nodes follow a spatial route-to-chaos along the chain. In this example $\varepsilon = 0.14$.

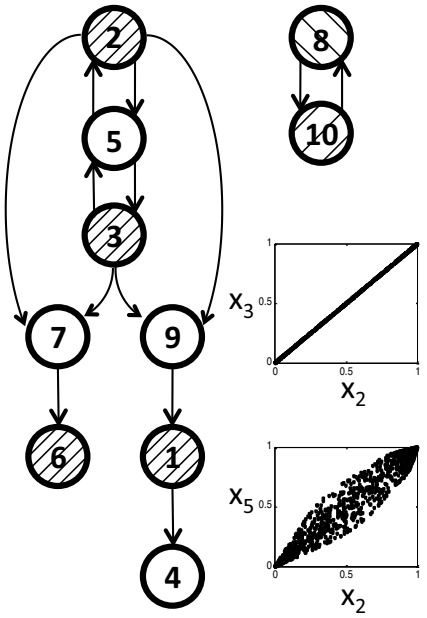

Fig. 6.14 Example of polysynchronous network for $\varepsilon = 0.78$. Nodes filled with the same pattern are synchronous. The dynamics of both synchrony classes is chaotic in this case.

bility of the simplest (and more common) polysynchronous states in the triplet with transposition symmetry which is one of the smallest structures that can show polysynchrony. As explained in the appendix, the obtained results are independent of the value of m' (see Fig. 6.6 **B.**) and therefore, are also valid for the case of a strongly connected pair with a third node unidirectionally coupled to one of the nodes in the pair ($m' = m$ or $m' = 0$). The polysynchrony in the interval $0.12 \lesssim \varepsilon \lesssim 0.20$ is mainly explained by the stability of the period-2 polysynchronous state. This state is stable in the range $0.140375 \lesssim \varepsilon \lesssim 0.193814$. Although this state occupies most of the interval, quasiperiodic polysynchronous states and periodic polysynchronous states of higher period can be numerically witnessed since these attractors coexist with the period-2 attractor in the dynamics of the strongly connected pair. As we have also determined analytically, chaotic polysynchrony with coupled fully-chaotic logistic maps ($\lambda = \ln 2$) is only possible for $\varepsilon > 0.75$. This fact, together with the stability of the fixed-point polysynchronous state in the range $0.806186 \lesssim \varepsilon \lesssim 0.86$ accounts for most of the polysynchrony found in

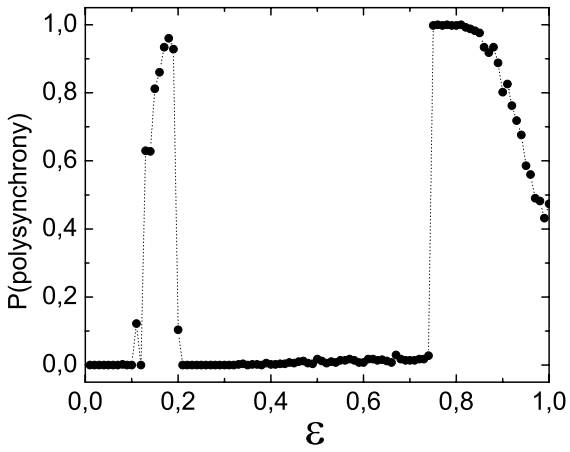

Fig. 6.15 Percentage of final network topologies of size $N = 10$ showing polysynchronous patterns calculated over 500 realizations of the system as a function of ε.

$\varepsilon > 0.75$. However, as before, other periodic and quasiperiodic polysynchronous states can be found in this range of parameters.

6.6 Discussion

In this chapter we have studied the dynamics of a single adaptive network model as a function of the coupling parameter. We have shown that the network reaches a frozen state where the rewiring stops. Moreover, we have shown that the final topologies are usually hierarchical and that polysynchronous dynamics appear in the frozen networks for certain parameter values. The hierarchical structure of the networks facilitates the appearance of polysynchrony as a stable attractor of the dynamics by making it easier to establish a balanced equivalence relation on the nodes. The stability study of different polysynchronous states accounts for the concrete coupling parameter ranges for which polysynchrony can be observed.

The emergence of polysynchrony in networks of undifferentiated nodes operating with a simple homophilic dynamic evolution suggests natural mechanisms for the emergence of polysynchrony in nature. In terms of applications or future work, combining this with an additional slow timescale dynamics to describe the evolution of differentiated polysynchronous states over time would provide a way of locking in the polysynchronous pattern making it more stable to perturbation, or alternatively the evolutionary dynamics could select the appropriate polysynchronous patterns if only some subset of the possible patterns is advantageous to the system. The hierarchical nature of the asymptotic networks imply that they could operate as motifs [114], with a well defined input and output level, so in this case our model may provide a mechanism for functional differentiation. Models similar to the one proposed here are used to describe metapopulations [115] so there may also be applications in this area.

Appendix C
Synchronization dynamics of strongly connected components

To study the stability of the synchronized state of the different strongly connected components we will follow the approach exposed in [72]. In all the cases we study the coupling is linear and can be written, in general, as

$$x^i_{n+1} = \sum_{j=1}^{N} L^{ij} f(x^j_n), \tag{C.1}$$

where L is the linear coupling operator.

For this simple case it is known that the synchronous state exists if the operator L has an eigenvalue $\sigma_1 = 1$ corresponding to the eigenvector $\mathbf{e}_1 = (1,1,\ldots,1)$. Since our coupling is dissipative, the rest of the eigenvalues of the coupling operator are in modulus less than one. The stability of the synchronized state is then given by the condition

$$\lambda_\perp = \lambda + \ln|\sigma_2| < 0, \tag{C.2}$$

where $\lambda_\perp$ is the transverse lyapunov exponent, λ is the lyapunov exponent of the uncoupled map and σ_2 is the second largest eigenvalue of the coupling operator.

C.1 Dynamics of the strongly connected pair

The strongly connected pair (Fig. 6.6**A.**) forms a system of two coupled logistic maps of the form

$$\begin{pmatrix} x^i_{n+1} \\ x^j_{n+1} \end{pmatrix} = \begin{pmatrix} 1-\varepsilon & \varepsilon \\ \varepsilon & 1-\varepsilon \end{pmatrix} \begin{pmatrix} f(x^i_n) \\ f(x^j_n) \end{pmatrix}. \tag{C.3}$$

This system has been thoroughly studied as a model of population dynamics in [116, 117, 118].

In this case the linear operator has eigenvalues $\sigma_1 = 1$ ($\mathbf{e}_1 = (1,1)$) and $\sigma_2 = 1-2\varepsilon$ ($\mathbf{e}_2 = (-1,1)$). Thus the stability condition reads

$$\lambda_\perp < 0 \rightarrow \begin{cases} \lambda + \ln(1-2\varepsilon) < 0, \, \varepsilon < \frac{1}{2}, \\ \lambda + \ln(2\varepsilon - 1) < 0, \, \varepsilon > \frac{1}{2}. \end{cases} \tag{C.4}$$

Therefore, the synchronization of the pair is stable when

$$\frac{1-e^{-\lambda}}{2} < \varepsilon < \frac{1+e^{-\lambda}}{2}. \tag{C.5}$$

C.2 Dynamics of the triplet with transposition symmetry

The linear operator in the case of the triplet with transposition symmetry (Fig. 6.6**B.**) is given by

$$L = \begin{pmatrix} 1-\varepsilon & \varepsilon & 0 \\ \varepsilon\frac{m'}{m} & 1-\varepsilon & \varepsilon\frac{m-m'}{m} \\ 0 & \varepsilon & 1-\varepsilon \end{pmatrix}, \tag{C.6}$$

with eigenvalues

$$\begin{aligned} \sigma_1 &= 1, \\ \sigma_2 &= 1-\varepsilon, \\ \sigma_3 &= 1-2\varepsilon, \end{aligned}$$

corresponding to the eigenvectors $\mathbf{e}_1 = (1,1,1)$, $\mathbf{e}_2 = (\frac{m'-m}{m'},0,1)$, $\mathbf{e}_3 = (1,-1,1)$.

We should note that which eigenvalue has the second largest modulus depends on the value of ε and the stability condition has to be evaluated for both σ_2 and σ_3. It is an easy calculation to deduce that the synchronized chaotic state will be stable in the range

$$1-e^{-\lambda} < \varepsilon < \frac{1+e^{-\lambda}}{2}. \tag{C.7}$$

C.3 Dynamics of the 3-cycle

The linear operator of the 3-cycle (Fig. 6.6**C.**) reads

$$L = \begin{pmatrix} 1-\varepsilon & \varepsilon & 0 \\ 0 & 1-\varepsilon & \varepsilon \\ \varepsilon & 0 & 1-\varepsilon \end{pmatrix}, \tag{C.8}$$

and has eigenvalues

$$\begin{aligned} \sigma_1 &= 1, \\ \sigma_2 &= \frac{1}{2}(2-3\varepsilon+i\varepsilon\sqrt{3}), \\ \sigma_3 &= \frac{1}{2}(2-3\varepsilon-i\varepsilon\sqrt{3}). \end{aligned}$$

Thus, the stability condition of the synchronous state reduces to

$$\lambda + \ln|\sigma_2| < 0 \rightarrow \lambda + \ln\sqrt{1-3\varepsilon+3\varepsilon^2} < 0. \tag{C.9}$$

Solving this for ε provides us with the condition

$$\frac{1}{2} - B < \varepsilon < \frac{1}{2} + B, \tag{C.10}$$

where

$$B = \frac{1}{2\sqrt{3}} e^{-2\lambda}\sqrt{-e^{2\lambda}(e^{2\lambda}-4)}. \tag{C.11}$$

Therefore, the stability region for the synchronous state of the 3-cycle is an interval centered around $\varepsilon = 0.5$ of a width depending on the lyapunov exponent λ of the map. Notice that when $\lambda = \ln 2$, B vanishes and the synchronous state becomes unstable for all ε.

C.4 Dynamics of the unidirectional coupling

Apart from the dynamics of the strongly connected components, it is necessary to study the case where a node is influenced by a single neighbour following an orbit of the uncoupled logistic map or, equivalently, by a fully synchronized neighbourhood. In both cases the dynamics is given by

$$\begin{pmatrix} x_{n+1} \\ y_{n+1} \end{pmatrix} = \begin{pmatrix} 1-\varepsilon & \varepsilon \\ 0 & 1 \end{pmatrix} \begin{pmatrix} f(x_n) \\ f(y_n) \end{pmatrix}, \tag{C.12}$$

where x_n is the variable of the node being influenced and y_n the trajectory of the synchronized neighbourhood. Note that it is implied in the equation that the input is a trajectory of the uncoupled map ($y_{n+1} = f(y_n)$). If this were not the case we could not perform this analysis.

The eigenvalues of the linear operator are $\sigma_1 = 1$ ($\mathbf{e}_1 = (1,1)$) and $\sigma_2 = 1-\varepsilon$ ($\mathbf{e}_2 = (1,0)$). Therefore, the influenced node will synchronize to its input if

$$\varepsilon > 1 - e^{-\lambda}. \tag{C.13}$$

Appendix D
Stability of the polysynchronous states

We study in this appendix the stability of different polysynchronous states in the simplest structure capable of showing polysynchrony: the triplet with transposition symmetry. In this case polysynchrony means full synchronization of nodes i and k. Thus, the quotient system of the triplet is a completely connected pair and the possible polysynchronous dynamics are therefore attractors of the completely connected pair.

D.1 Fixed point polysynchronous state

The completely connected pair has two fixed points (c_1, c_2) and (c_2, c_1) with

$$c_1 = \frac{1}{8(2\varepsilon-1)}(8\varepsilon - 3 + \sqrt{9-4\varepsilon(9-8\varepsilon)}),$$
$$c_2 = \frac{1}{8(2\varepsilon-1)}(8\varepsilon - 3 - \sqrt{9-4\varepsilon(9-8\varepsilon)}),$$

that are stable in the range $0.806186 \lesssim \varepsilon \lesssim 0.86$. These allow the triplet to have two possible polysynchronous fixed point states: (c_1, c_2, c_1) or (c_2, c_1, c_2). The stability of this states can be evaluated as the stability of a fixed point of a three dimensional system by studying the absolute value of the eigenvalues of the jacobian matrix at the fixed point. The jacobian matrix for the triplet with transposition symmetry reads

$$J(x^i, x^j, x^k) = \begin{pmatrix} (1-\varepsilon) f'(x^i) & \varepsilon f'(x^j) & 0 \\ \varepsilon \frac{m'}{m} f'(x^i) & (1-\varepsilon) f'(x^j) & \varepsilon \frac{m-m'}{m} f'(x^k) \\ 0 & \varepsilon f'(x^j) & (1-\varepsilon) f'(x^k) \end{pmatrix},$$

In Fig. D.1 we represent the absolute value of the eigenvalues of $J(c_1, c_2, c_1)$ as a function of ε and we observe that the polysynchronous state is stable in all the stability range of the fixed points.

It is very interesting to note that the eigenvalues are independent of m' and therefore our conclusions are also valid for a completely connected pair with an outgoing link to a third node (as in the 3-node subsystem of Fig. 6.3.**e.**).

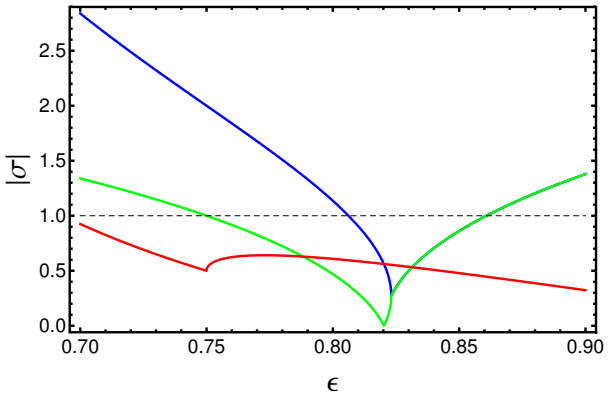

Fig. D.1 Eigenvalues of J evaluated at the fixed point (c_1, c_2, c_1) as a function of ε. The three eigenvalues have modulus less than unity in the range $0.806186 \lesssim \varepsilon \lesssim 0.86$.

D.2 Period-2 polysynchronous state

As described in [116], the period-2 orbit of the completely connected pair has as its elements

$$\begin{aligned}(z_1, z_2) &= (\frac{u+v+1}{2}, \frac{u-v+1}{2}),\\ u &:= \frac{1}{4g},\\ v &:= \frac{\sqrt{8g^2-2g-1}}{4g},\\ g &:= 1-2\varepsilon.\end{aligned}$$

This period-2 dynamics is stable in the range $0.13925 \lesssim \varepsilon \lesssim 0.193814$.

Similarly to the fixed-point case, the stability of the period-2 polysychronous state can be studied as the stability of a period-2 orbit of a three dimensional system. Therefore, we should observe the eigenvalues of the jacobian matrix

$$J_2(z_1, z_2) = J(z_1, z_2, z_1) \cdot J(z_2, z_1, z_2). \tag{D.1}$$

The eigenvalues of J_2 have been graphed in Fig. D.2 as a function of the coupling strength. From this figure we see that the period-2 polysynchronous state is stable when $0.140375 \lesssim \varepsilon \lesssim 0.193814$.

Interestingly, and contrary to the fixed-point case, there is an interval of coupling strengths ($0.13925 \lesssim \varepsilon \lesssim 0.140375$) where the period-2 orbit is stable in the pair but the period-2 polysynchronous state of the triplet is unstable. It is in this interval of values where the spatial period-doubling phenomena appears (see Fig. 6.13 and description in the text).

D.3 Chaotic polysynchronous state

To study the stability of the chaotic polysynchronous states we start by making the following change of variable

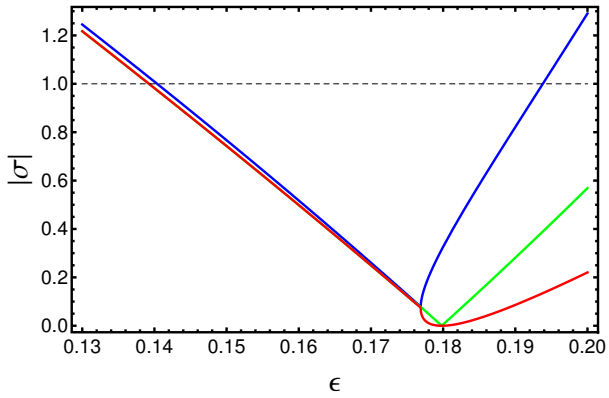

Fig. D.2 Eigenvalues of J_2 as a function of ε. The three eigenvalues have modulus less than unity in the range $0.140375 \lesssim \varepsilon \lesssim 0.193814$.

$$U = \frac{x^i + x^k}{2},$$
$$V = x^j,$$
$$W = \frac{x^k - x^i}{2}.$$

In these new variables, the dynamics is given by

$$U_{n+1} = \frac{1}{2}[(1-\varepsilon)(f(U_n - W_n) + f(U_n + W_n))] + \varepsilon f(V_n),$$
$$V_{n+1} = \varepsilon \frac{m'}{m} f(U_n - W_n) + (1-\varepsilon) f(V_n) + \varepsilon \frac{m' - m}{m} f(U_n + V_n),$$
$$W_{n+1} = \frac{(1-\varepsilon)}{2}[f(U_n + W_n) - f(U_n - W_n)].$$

The polysynchronous chaotic state corresponds to the case $W_n = 0 \forall n$ with U_n and V_n following a non-synchronous chaotic orbit that we denote U^*,V^*. By expanding the equation for W_{n+1} around $(U^*, V^*, 0)$ we obtain

$$W_{n+1} \approx -2(1-\varepsilon) U_n^* W_n. \tag{D.2}$$

Assuming ergodicity, the transverse Lyapunov exponent (transverse to the surface of $\mathbb{R}^3$ where the polysynchronous orbit lies) can be written as [72]

$$\lambda_\top = \ln|-2(1-\varepsilon)| + \lambda^*, \tag{D.3}$$

where λ^* is the average Lyapunov exponent of the orbit U_n^* and has the upper bound $\ln 2$, that would correspond to the complete synchronization of U_n and V_n (or equivalently, x^i and x^j). We need $\lambda_\top < 0$ for the polysynchronous chaotic state to be stable. This condition provides us with a relation between the Lyapunov exponent of the chaotic orbit of U^* and the minimum coupling strength necessary for polysynchrony to be stable

$$\varepsilon_{min} = 1 - \frac{e^{-\lambda^*}}{2}. \tag{D.4}$$

It is easy to see that ε_{min} is always greater than 0.5 for $\lambda^* \leq \ln 2$. This is in agreement with the numerical experiments, which do not witness chaotic polysynchrony for $\varepsilon < 0.5$.

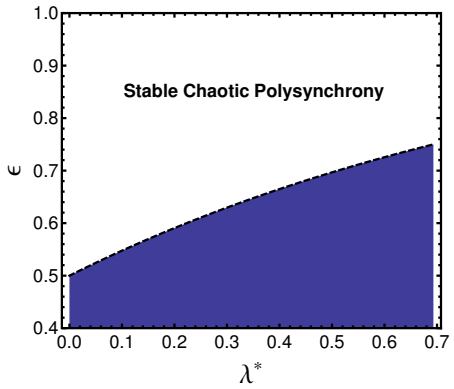

Fig. D.3 Region of stability of the chaotic polysynchronous state as a function of the Lyapunov exponent of the chaotic orbit. The dashed line corresponds to ε_{min}.

Part III
Analysing real-world complex dynamics: The sleep slow waves

Chapter 7
Introducció: dinàmiques complexes de l'activitat elèctrica cerebral

> [...] I soon appreciated that to understand how the brain functions, I would have to learn how to listen to neurons, to interpret the electrical signals that underlie all mental life. Electrical signaling represents the language of mind, the means whereby nerve cells, the building blocks of the brain, communicate with one another over great distances. Listening in on those conversations and recording neuronal activity was, so to speak, objective introspection.
>
> Eric Kandel *In search of memory*

7.1 Introducció

En aquesta part de la tesi ens acostarem a la complexa activitat elèctrica cerebral a través de l'estudi de la dinàmica cortical de les ones lentes cerebrals, un patró electroencefalogràfic característic que apareix durant les fases més profundes del son. Abans, però, sembla convenient motivar i situar aquest estudi en el context de la tesi explicant, entre altres coses, per què entenem el cervell com un sistema complex. A més a més, cal que introduïm alguns conceptes bàsics de neurociències que s'empraran en el capítol següent. Per començar farem una breu descripció de la fisiologia de la neurona a través de la història dels principals descobriments en aquest camp. Després descriurem breument l'anatomia del còrtex cerebral i d'algunes estructures subcorticals. Per acabar, explicarem què és l'electroencefalografia, quina informació ens aporta i com la podem emprar per a l'estudi del son.

7.2 Història de l'estudi de l'activitat elèctrica cerebral

Els primers indicis que l'electricitat jugava un paper en la fisiologia animal els trobem als famosos experiments amb granotes de Luigi Aloisio Galvani (*De viribus electricitatis in motu musculari commentarius*, 1791). Galvani proposà que l'electricitat era segregada pel cervell i que aquesta fluïa fins els músculs a través dels nervis. Si bé aquest símil de l'electricitat com a fluid no era encertat, Galvani sí encertà en dir que els nervis havien d'estar envoltats per una substància aïllant per tal que es produïra la propagació de l'electricitat de manera eficient.

Uns setanta anys més tard, Hermann von Helmholtz (1821-1894), físic i metge alemany, mesurava la velocitat de propagació d'un senyal elèctric a través d'una fibra nerviosa viva i comprovava que aquesta propagació és diferent a la d'un corrent elèctric en un fil metàl·lic [119]. Al contrari del que passa en un fil de coure, la propagació en la fibra nerviosa, si bé més lenta, perd menys intensitat en el recorregut. Aquestes primeres ob-

servacions es realitzaven a escala macroscòpica però la transmissió de senyals elèctrics pel teixit nerviós requeria d'una explicació en termes de l'estructura microscòpica d'aquest teixit.

Santiago Ramón y Cajal (1852-1934), premi Nobel de fisiologia o medicina en 1906, fou el primer, gràcies en gran part a la seua perícia experimental, en interpretar correctament allò que veia a través del microscòpi quan examinava mostres de teixit cerebral [120]. Cajal va descriure la neurona com un cèl·lula aïllada composada pel cos cel·lular, un axó i multitud de dendrites (Figura 7.1). Més enllà de la descripció anatòmica, Cajal va proposar diversos principis sobre el funcionament de les neurones i el seu paper en el sistema nerviós. Va determinar que la neurona era la unitat fonamental, tant estructural com funcional, del cervell. També va deduir que la neurona rep informació a través de les dendrites i la transmet mitjançant l'axó, de manera que el flux d'informació té un sentit ben definit i únic. Li devem també a ell la descripció de la sinapsi com el lloc on les terminals de l'axó d'una neurona es comuniquen amb les dendrites d'una altra sense arribar a tocar-se.

Ara sabem que les neurones es comuniquen entre elles mitjançant els potencials d'acció, un impuls de potencial elèctric d'uns pocs milisegons de durada que viatja a través de l'axó de la neurona a una velocitat d'uns 120 m/s.

El potencial d'acció d'una sola neurona fou enregistrat per primera vegada per Edgar Douglas Adrian (1889-1977) [121]. Adrian va comprovar que aquests potencials tenien sempre la mateixa forma (Figura 7.1) i va deduir que la intensitat d'un estímul o percepció era proporcional a la freqüència d'emissió dels potencials d'acció i no a la seva amplitud.

Charles Sherrington (1857-1952), gran admirador de Ramón y Cajal, descobrí mitjançant l'estudi de comportaments reflexos que no tots els potencials d'acció tenen com a resultat excitar la neurona postsinàptica sinó que hi existeixen neurones inhibidores que actuen per evitar que la neurona postsinàptica emeta un potencial d'acció (*The integrative action of the nervous system*, 1906). Pels seus treballs Sherrington i Adrian compartiren el Premi Nobel de fisiologia o medicina l'any 1932.

Però, com es genera un potencial d'acció? Julius Bernstein (1839-1917) havia formulat una hipòtesi el 1902 sobre el mecanisme de generació del potencial d'acció. L'anomenada hipòtesi de la membrana de Bernstein es basa en la permeabilitat selectiva de la membrana cel·lular a determinats ions. En concret, Berstein explicà que a l'interior de la neurona s'estableix un equilibri entre proteïnes carregades negativament i ions positius K^+. Al fluid extracel·lular l'equilibri l'estableixen uns ions distints, en concret Na^+ i Cl^-. Segons Bernstein, la membrana en repòs és sols permeable als ions potassi K^+ que, degut al gradient de concentracions establert entre l'interior i l'exterior de la cèl·lula, surten a l'exterior i romanen pegats a la part exterior de la membrana degut a la càrrega negativa neta que queda dins la cèl·lula. Aquest mecanisme explicaria el potencial en repòs de la membrana, que es va mesurar en -70 mV. Bernstein també proposa un mecanisme per a la generació del potencial d'acció considerant que, en ser suficientment excitada, la membrana perdia la permeabilitat selectiva i els ions de tot tipus podien circular lliurement, duent temporalment la diferència de potencial de -70 mV a 0 mV.

Tanmateix, aquesta última conclusió de Bernstein fou errada i el vertader mecanisme del potencial d'acció hagué d'esperar als treballs d'Alan Hodgkin (1914-1998) i Andrew Huxley (1917-) sobre l'axó gegant del calamar que els valgueren el premi Nobel de fisiologia o medicina l'any 1973 (junt amb John Eccles pels seus treballs sobre la sinapsi) [122]. El tamany de l'axó gegant del calamar, que fa quasi 1 mm de diàmetre i es pot observar a ull nu, va permetre a Hodgkin i Huxley enregistrar el potencial elèctric dins

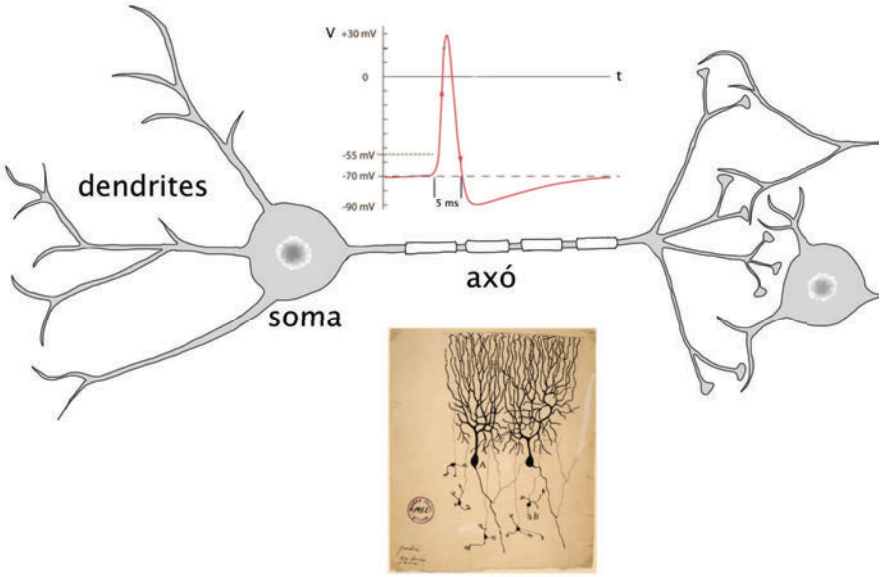

Figura 7.1 Dibuix esquemàtic d'una neurona. S'observa el cos neuronal o soma, les dendrites i l'axó. A la dreta s'han representat també les connexions sinàptiques amb una altra neurona. Dalt s'observa un potencial d'acció estàndard i baix es mostra una il·lustració d'unes neurones del cerebel d'un colom realitzada per Santiago Ramón y Cajal (1889, Instituto Santiago Ramón y Cajal, Madrid).

i fòra de la cèl·lula. Comprovaren que, efectivament, el potencial en repòs de la membrana és d'uns -70 mV i que aquest està causat pel moviment dels ions K^+. No obstant, enregistraren una amplitud de 110 mV per al potencial d'acció (40 mV més del predit per Bernstein) i varen concloure que durant el potencial d'acció la membrana continua seleccionant de manera activa el trànsit d'ions. El que realment passa és que la membrana es fa permeable de manera alternada als ions Na^+ i K^+. És a dir, quan la membrana és suficientment excitada, esdevé permeable als ions Na^+ que es troben en gran concentració en el fluid extracel·lular. El gradient de concentració mou Na^+ cap a l'interior de la cèl·lula fent passar el potencial de -70 mV a +40 mV. Açò correspon a la pujada del potencial d'acció. Immediatament després canvia de nou la permeabilitat de la membrana, fent-se de nou permeable als ions K^+, la sortida dels quals retorna el potencial a -70 mV.

A més a més, Hodgkin i Huxley identificaren en la membrana cel·lular els canals iònics que permeten aquest mecanisme i que estan regulats pel voltatge de la membrana - en contraposició als canals identificats per Bernstein per al potassi que no són regulats pel voltatge. Una vegada la neurona ha emès un potencial d'acció, una proteïna s'encarrega de restablir les concentracions inicials d'ions a l'interior i l'exterior de la cèl·lula.

La història de la comprensió del funcionament de la neurona no acaba ací. La transmissió d'informació a través de la sinapsi, per exemple, fou un misteri i una important font de controvèrsia durant molts anys fins el descobriment dels neurotransmissors químics. Una història detallada dels principals descobriments sobre la fisiologia i dinàmica del sistema nerviós es pot trobar a [123, 124].

Com hem vist, avui en dia la neurona i la comunicació interneuronal són relativament ben conegudes. Malgrat açò però, estem encara molt lluny d'una comprensió real de tota la complexitat dinàmica que es genera quan grans poblacions de neurones interaccionen entre elles.

El cervell com a sistema complex

Com diu la cita que obri aquest capítol, nosaltres som el resultat de la interacció neuronal. Els nostres records, el llenguatge, el pensament matemàtic o la nostra consciència emergeixen de la comunicació elèctrica entre bilions d'aquestes petites cèl·lules.

El cervell és un exemple paradigmàtic de sistema complex tal i com s'ha definit aquest concepte en la part anterior de la tesi. A més a més l'activitat cerebral es desenvolupa en diferents escales, tant espacials com temporals, sense que existisca una clara divisió entre elles [125, 126]. La memòria és un bon exemple de fenomen multiescala. Els records poden durar des d'uns pocs segons fins anys i dècades. La seva formació i la seva recuperació no obstant, depenen de processos elèctrics i moleculars que duren des d'uns pocs milisegons a unes quantes hores. En termes espacials sabem que diferents estructures macroscòpiques, com l'hipocamp, estan involucrades en la consolidació de la memòria però aquesta pot finalment dependre de xarxes neuronals d'unes poques neurones.

Segurament l'aproximació al problema d'estudiar la dinàmica cerebral que més atenció ha rebut en els últims anys ha sigut la que ha vingut del camp de les xarxes complexes (veure [127] i referències allí citades). El cervell es deixa interpretar bastant fàcilment com una xarxa complexa amb les neurones actuant com a nodes. Aquesta xarxa és, a més, adaptativa, donat que les sinapsi entre neurones varien amb el temps. La dinàmica de comunicacions nervioses en aquesta xarxa complexa dóna lloc a fenòmens emergents com la consciència o la memòria. Aiximateix, també és poden definir xarxes de connectivitat entre regions senceres del còrtex cerebral i fer un estudi de la connectivitat a escala de poblacions de neurones [128]. En aquest capítol estudiarem la propagació de les ones lentes en el còrtex fent ús del concepte de xarxa.

7.3 Breu descripció anatòmica del cervell

Des d'un punt de vista anatòmic, el cervell forma part del sistema nerviós central que està composat, a més, pel tronc de l'encèfal, el cerebel i la medul·la espinal. El cervell en concret no és una massa uniforme de neurones sinó que té una gran estructura interna. Una descripció exhaustiva de l'anatomia cerebral està fora dels objectius d'aquesta introducció però sembla convenient introduir una breu descripció d'algunes regions anatòmiques del cervell a les quals es farà menció en aquesta part de la tesi. Per a un estudi més profund sobre aquest tema recomanem [129].

Còrtex

El còrtex o escorça cerebral és la capa més externa del cervell. També és la part més evolucionada i té al seu càrrec les funcions cognitives de més alt nivell. El còrtex està format bàsicament per cossos neuronals amb els seus corresponents axons i dendrites. Açò fa que adquirisca un color gris quan es prepara el teixit amb una certa tintura per al seu estudi. Aquest és l'origen del nom de matèria gris per al còrtex. Part de les neurones del còrtex emeten els seus axons cap a l'interior del cervell. Aquests axons formen fibres i constitueixen el que es coneix com matèria blanca. El còrtex té un espessor de 2 a 4 mm i s'estructura en capes, cadascuna d'elles amb una composició neuronal característica.

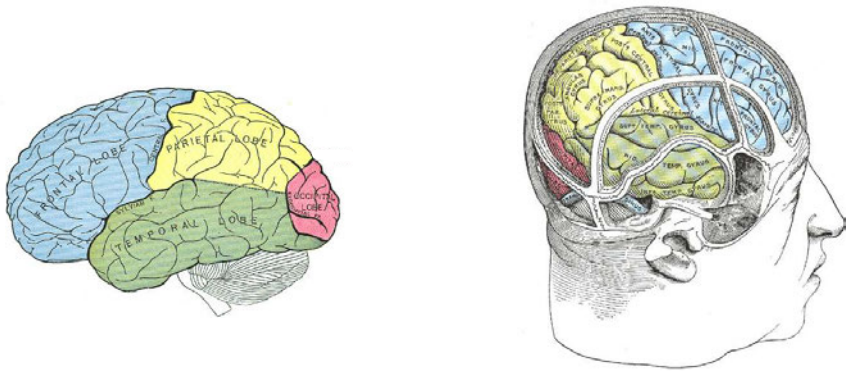

Figura 7.2 A l'esquerra observem els lòbuls frontal (blau), parietal (groc), temporal (verd) i occipital (roig). També s'aprecia el cerebel i part del tronc de l'encèfal. A la dreta podem veure una il·lustració de la posició dels diferents lòbuls adins del crani. (Font: Henry Gray, Anatomy of the human body, 1918, 20a Edició.)

A nivell macroscòpic s'aprecia com una superfície fortament convolucionada que es divideix en 5 regions o lòbuls: frontal, temporal, parietal, occipital i ínsula (veure les Figures 7.2 i 7.3).

El lòbul frontal es situa en la part anterior del cervell i és l'encarregat de les funcions cognitives de més alt nivell com ara la presa de decisions, el llenguatge (tasca compartida amb els lòbuls parietal i temporal), la conducta social o els aspectes morals del comportament. També està involucrat en la memòria a llarg termini.

El lòbul temporal se situa en la part lateral inferior dels hemisferis cerebrals per sota de l'anomenada fissura lateral. En el lòbul temporal es processa la informació auditiva i està involucrat per tant en tasques de comprensió del llenguatge i en l'equilibri. També col·labora en el processament d'informació visual i es clau en la consolidació de la memòria.

El lòbul parietal es troba en la part superior posterior del cervell, per darrere del lòbul frontal. Aquest lòbul integra la informació dels sentits i és l'encarregat de la visió espacial. Aiximateix, és el responsable del pensament numèric i matemàtic.

El lòbul occipital es troba a la part posterior del cervell i la seva funció essencial és el processament de la informació visual.

L'ínsula està situada adins de la cissura de Silvio, en la separació entre els lòbuls temporal i parietal. Aquesta regió cortical està relacionada amb el sistema límbic i per tant està involucrada en el processament d'emocions i les reaccions fisiològiques a aquestes.

Tàlem

El tàlem és una estructura interna del cervell (Figura 7.3) composada majoritariament de matèria gris. Està connectat amb multitud d'estructures subcorticals i corticals i funciona com una mena d'administrador d'informació. Per exemple, la informació de tots els sentits, excepte l'olfacte, passa pel tàlem abans d'anar a l'àrea cortical encarregada de processar-la. A més a més, el tàlem està involucrat en la regulació de les fases del son i del nostre nivell d'atenció i activitat.

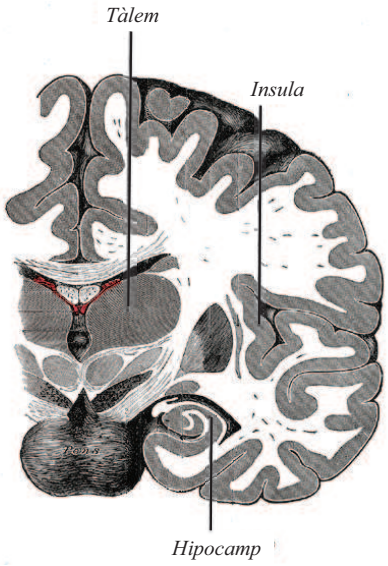

Figura 7.3 Detall anatòmic d'una secció del cervell humà on s'aprecien la distinció entre la matèria gris (còrtex) i la matèria blanca. S'han assenyalat també estructures internes com el tàlem, l'ínsula i l'hipocamp (Font: Henry Gray, Anatomy of the human body, 1918, 20a Edició).

Hipocamp

Aquesta estructura es troba a l'interior dels lòbuls temporals (Figura 7.4), es composa de matèria gris i deu el seu nom a la seva semblança amb el cavallet de mar (gènere *Hippocampus*). Entre altres coses, l'hipocamp i les regions corticals associades s'encarreguen de la consolidació de records. Lesions en ambdós hipocamps poden fer que una persona no siga capaç de generar nous records, sense afectar però a la memòria ja consolidada.

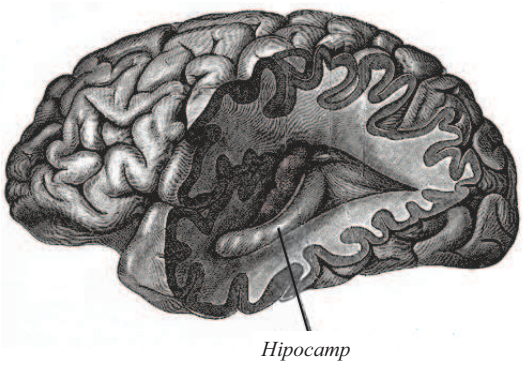

Figura 7.4 Detall de la situació exacta de l'hipocamp a l'interior del cervell (Font: Henry Gray, Anatomy of the human body, 1918, 20a Edició).

Amígdala

L'amígdala és una estructura amb una forma i grandària semblant a la d'una ametlla (d'ahí el seu nom) que es troba a l'interior del lòbul temporal, molt pròxima a la part anterior de l'hipocamp. L'amígdala, igual que l'hipocamp, ajuda a consolidar la memòria

però es dedica específicament a avaluar la resposta emocional a una certa experiència o estímul per tal de modular, en conseqüència, la consolidació del record.

7.4 Electroencefalografia i estudi del son

L'electroencefalografia és l'amplificació i enregistrament de diferències de potencial resultants de l'activitat elèctrica cerebral. Aquestes diferències de potencial es mesuren amb elèctrodes que poden situar-se en la superfície del crani (*scalp* EEG) o poden introduir-se quirúrgicament adins del crani en la superfície o a l'interior del còrtex. En ambdós casos la resolució temporal de la mesura és de l'ordre de 10^{-3} s, sent aquesta la major de totes les tècniques de mesura de la dinàmica cerebral. La resolució espacial és major en el cas dels microelèctrodes de profunditat que en els elèctrodes de superfície. Cal tindre en compte que els elèctrodes de superfície integren la informació d'uns pocs centímetres quadrats de superfície i que s'estima que en 1 mm^2 de còrtex hi ha unes 10^5 neurones. L'EEG de superfície és per tant una mesura de la diferència de potencial promedi resultant de l'activitat d'un gran nombre de neurones [130].

En el cas dels microelèctrodes de profunditat hi ha dues contribucions ben diferenciades a l'EEG. Per una banda s'enregistren els potencials d'acció de les neurones properes a l'elèctrode i per una altra banda l'anomenat potencial de camp local (*local field potential*, LFP, en anglès). El LFP té una freqüència i amplitud molt menor que els ràpids potencials d'acció, i es creu que està produït pels potencials sinàptics i els potencials d'acció de neurones més llunyanes [131].

El naixement de l'electroencefalografia sol fixar-se en la segona meitat del s. XIX quan Richard Caton (1842-1926) enregistrà l'activitat elèctrica cerebral de conills, gats i mones [132]. Entre altres apreciacions sobre aquests senyals, Caton va notar que la dinàmica enregistrada dels corrents elèctrics cerebrals dels conills amb els quals experimentava eren diferents segons si aquests estaven desperts o dormien. Una llista bastant completa de les fites històriques de l'electroencefalografia es pot consultar en [133].

7.4.1 Espectre de les ones cerebrals

El primer EEG d'un humà fou obtingut per Hans Berger (1873-1941) en els anys 20 del s. XX. Berger anomenà ritme alfa (α) les oscil·lacions de gran amplitud i uns 10 Hz de freqüència que observava quan el subjecte tenia els ulls tancats. Anomenà beta (β) aquelles més ràpides i de menor amplitud que apareixien quan els ulls estaven oberts. Per altra banda, les ones theta (θ), de menor freqüència que les ones alfa, foren observades per primera vegada en conills anestesiats i foren les primeres a les quals se'ls va poder atribuir una funció cognitiva en trobar una relació amb el reflex de l'orientació en felins [134]. Seguint aquesta tradició, altres bandes de freqüència foren designades també amb lletres gregues i s'establiren divisions entre elles de manera quasi totalment arbitraria (Figura 7.5). Una classificació en bandes de freqüència de l'activitat EEG, més recent i més coherent amb els aspectes funcionals i cognitius, es pot trobar a [134, 135].

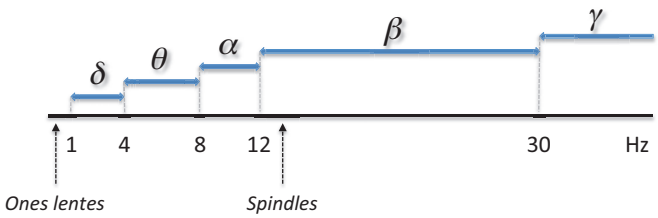

Figura 7.5 Nomenclatura de les oscil·lacions de l'EEG segons la banda de freqüències

7.4.2 Fases del son

Les fases del son foren identificades per primera vegada per Alfred Lee Loomis (1887-1975) l'any 1937 [136]. La primera classificació estandarditzada d'aquestes fases és la de Rechtschaffen i Kales de l'any 1968 [137]. L'any 2007 l'American Academy of Sleep Medicine (AASM) publicà una actualització d'aquesta classificació [138]. Es distingeixen actualment 4 fases del son, sense contar la vigília. Aquestes són: Fase I, Fase II, Fase III/IV (SWS) i REM [139, 140] (veure Figura 7.6).

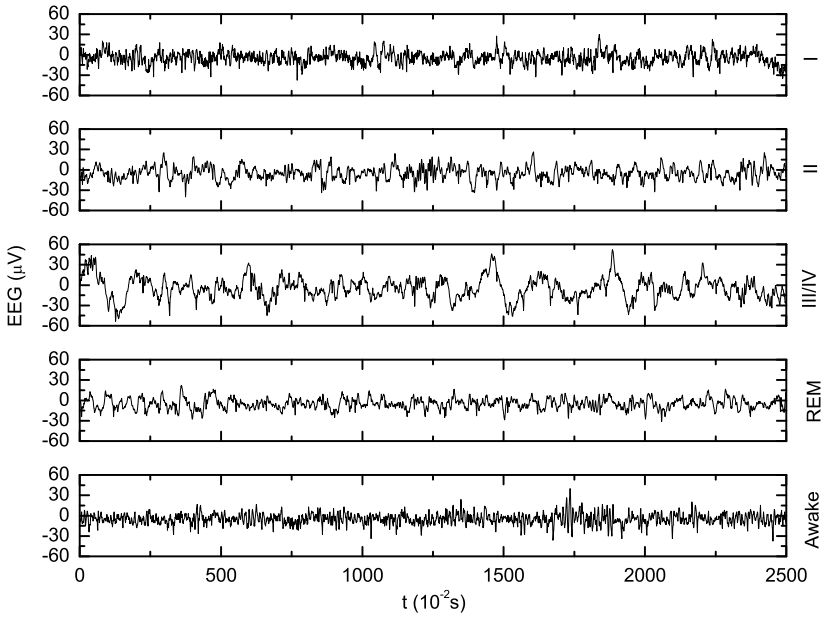

Figura 7.6 Exemples de registre EEG de les diferents fases del son i d'un estat de vigília.

La fase I és la fase de somnolència o son lleuger. La freqüència de l'activitat descendeix del rang alfa (8-12 Hz) pròpi de la vigília al rang theta (4-8 Hz). Es tracta d'oscil·lacions de baixa amplitud i no s'observen ni K-complex ni spindles (veure 7.4.3). La fase II es caracteritza per l'aparició dels spindles i els K-complex de manera regular. L'activitat de 7 Hz es fa més predominant, síncrona i bilateral i desapareix l'activitat beta. La fase II representa d'un 45% a un 55% del son en adults. En la fase III/IV o de son profund, predomina l'activitat delta i apareixen les ones lentes. És una activitat de gran amplitud ($> 75\ \mu V$) i poden aparèixer tant K-complex com spindles. Per últim,

en la fase REM trobem una activitat de baixa amplitud semblant a la de la vigília. No s'observen ones lentes ni spindles o K-complex. El to muscular pràcticament desapareix i s'observen moviments oculars ràpids de manera episòdica i irregular. En adults la fase REM representa aproximadament un 25 % del son.

7.4.3 Alguns patrons característics de l'EEG de son

A banda de les oscil·lacions sostingudes d'una certa freqüència o ones cerebrals que hem descrit abans, també s'han identificat patrons de curta durada que són recurrents i universals en els EEG de son. Aquests patrons no sols ens ajuden a distingir entre les diferents fases del son com acabem de veure sinó que es creu que compleixen determinades funcions, algunes de les quals encara s'estan investigant.

Spindles i K-complex

Els spindles són curts períodes d'activitat (0.5 - 1.5 s) en els quals augmenta la freqüència de l'EEG fins el rang 12-14 Hz (veure Figura 7.7). Els spindles apareixen de manera simètrica i bilateral en ambdós hemisferis cerebrals. Entre altres coses, es creu que els spindles generats al tàlem prevenen la disrupció del son per estímuls auditius externs.

Els spindles poden anar precedits pel patró anomenat K-complex, un pic negatiu d'alt voltatge seguit d'un pic positiu que dura en total 0.5 s aproximadament.

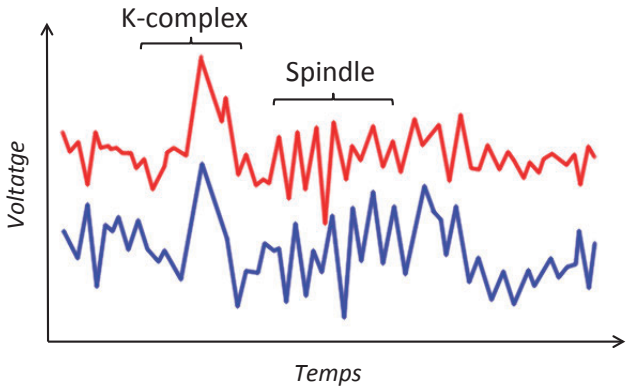

Figura 7.7 Exemple de spindle i K-complex. Les senyals corresponen a dos elèctrodes EEG de superfície (C3-A2 i C4-A1).

Ones lentes ($<$ 1 Hz)

El patró d'ona o oscil·lació lenta fou descrit per primera vegada per Mircea Steriade (1924-2006) i els seus col·laboradors l'any 1993 [141]. És una oscil·lació de gran amplitud ($>$ 140 μV) i baixa freqüència ($\lesssim$ 1 Hz) resultat de la sincronització de grans poblacions de neurones en el còrtex (Figura 7.8). Primer les neurones es sincronitzen en un estat hiperpolaritzat en el qual no es disparen potencials d'acció. Aquest estat si-

lent acaba amb les neurones disparant potencials d'acció de manera síncrona en el que s'anomena fase de despolarització.

Les ones lentes apareixen sols en la fase III/IV del son i es creu que juguen un paper fonamental en els processos d'aprenentatge i consolidació de la memòria [142, 143]. A més a més, s'ha observat que aquestes oscil·lacions viatgen a través del còrtex (d'ahí el nom d'ona) amb uns complexos patrons de propagació [144, 145, 146].

En aquesta part de la tesi presentarem alguns resultats sobre la dinàmica i la propagació d'aquestes ones lentes a partir de l'anàlisi de dades EEG intracranials. Més concretament, mostrem el descobriment de distribucions bimodals per als temps de despolarització i hiperpolarització de les ones lentes. Correlacionant aquestes distribucions amb l'activitat en la banda de freqüències dels spindles hem trobat que una possible causa de la bimodalitat pot ser el diferent paper jugat pel tàlem en la generació de segons quines ones lentes. A més a més, a partir de ressonàncies magnètiques obtingudes per a cada subjecte hem pogut reconstruir tridimensionalment la posició dels elèctrodes de registre adins del crani i açò ens ha permès estudiar la propagació de les ones lentes i fer una estimació de la seua velocitat.

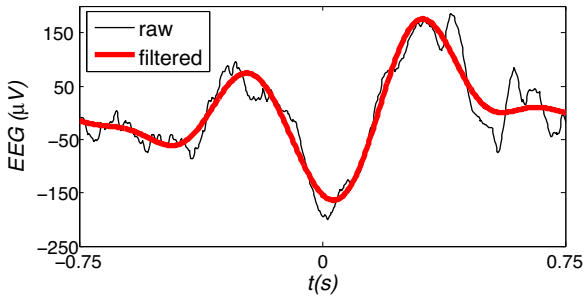

Figura 7.8 Exemple d'ona lenta. En negre, el senyal original i en roig, el senyal filtrat en el rang 0.1-4 Hz.

Chapter 8
Large-scale cortical dynamics of sleep slow waves

8.1 Introduction

Slow waves are the most prominent electroencephalographic (EEG) feature of sleep, consisting of alternating periods of activity and silence in cortical networks [141, 147]. As confirmed by in vivo [148] and in vitro [149] intracellular recordings in animals, the active states are associated with synaptically mediated depolarization and intense cellular firing whereas, during the silence states, neurons are hyperpolarized with a cessation of synaptic and firing activity. This slow rhythmical activity is generated intrinsically in the neocortex [149, 150], synchronizes cortical regions with high temporal precision [151] and can recruit multiple subcortical targets [152, 153]. This alternation of active and silent states in cortical neurons is thought to be involved in memory consolidation [154, 155, 156], synaptic homeostasis [157] and the restorative functions of sleep [158].

Nevertheless, despite considerable understanding of the cellular/synaptic mechanisms underlying these waves [153, 159], the spatial and temporal dynamics that generate these particular EEG elements in the human brain remain poorly specified [160, 161]. Scalp-level high-density EEG recordings have indicated that slow waves in humans have a non-uniform cortical distribution, suggesting that areas of the cortex are differently involved in slow waves [144]. Furthermore, recent observations reported that most sleep slow waves are in fact confined to local regions that are unevenly distributed across cortex [161]. In addition, consistent with recent imaging data of the mouse cortex [146], their propagations are composed of complex local paths with several points of origin [145].

Indubitably, scalp recorded EEG is insufficient to fully characterize their complex large-scale dynamics due to unavoidable effects of linear summations of current sources over large cortical territories and the considerable distances from recording sites to deep generators. These drawbacks can nevertheless be surmounted with the use of intracranial recordings [160, 161] which furthermore allow the analysis of short-range spatially coherent activities that are not promptly available with scalp recordings. In addition, the number of studies simultaneously analyzing local field potential (LFP) and scalp EEG signals both in animals and humans is rather small and therefore joint analyses at mesoscopic (e.g., LFPs) and macroscopic (e.g., scalp EEG) levels will provide valuable new data in this domain. In the present study, we examined slow wave cortical activity during polysomnographically defined sleep-wake states using simultaneous scalp EEG and intracranial recordings in 10 subjects who required a clinical invasive evaluation for the treatment of their epilepsy. Thanks to this relatively large sample size as well as to a broad spatial sampling (with a total of 417 investigated intracranial electrode sites) we were able to examine intracranially the characteristic morphologies, durations and

spatial propagations of slow waves over a comprehensive extent of the human cerebral cortex.

8.2 Bimodal distributions of the depolarization and hyperpolarization times

A group of 10 subjects with medically-refractory epilepsy were included in this study. Intracranial LFPs were recorded from the surface of the cortex (subdurally) or from depth electrodes implanted stereotactically in deeper cortical structures. Intracranial contacts sampled medial, lateral and basal frontal and temporal cortices, as well as medial and lateral parietal and occipital cortices (see Table 8.1 for further detail). All subjects had 2-3 selected overnight recordings. Slow waves were automatically identified from a single scalp electrode and only from segments of slow wave sleep using previous methodology [144] (see Materials and Methods section for further detail).

Following previous works [144, 151], the onset of each wave was positioned at the maximum negativity of the waves, as this is considered to reflect the transition to the depolarizing phase of the intracellularly defined slow oscillation. We assumed that the first process, which leads up to the synchronization of populations of neurons in a silent hyperpolarization phase, starts at the first maximum before the central minimum of the slow oscillation (hyperpolarization onset) and finishes at the subsequent minimum (depolarization onset). We called T_h the time span of this phase [162] (see Fig. 8.1**A**). At the depolarization onset, a second process starts where neurons are recruited to fire, leading to a global depolarization phase. We assumed that this phase ends at the first maximum after the onset of the depolarization and we called T_d its time span (Fig. 8.1**A**).

The analysis of intracranial recordings acquired simultaneously allowed us to directly characterize these different processes associated with scalp slow waves. In most cases, intracranial slow wave activities showed a reversed polarity with respect to the scalp EEG, confirming what has been previously shown in animal [150] and human studies [159]. Thus, the intracranial hyperpolarization phase was here considered to start at the first minimum and the depolarization onset was located at the maximum positivity peak (Fig. 8.1**A**).

We first analyzed the intracranial distributions for T_h and T_d measured over all detected slow waves ($n = 33442$) on all intracranial contacts ($n = 417$) (Fig. 8.1**B**). For every recorded subject, we found a bimodal distribution for the depolarization and hyperpolarization time spans. We designate the characteristic times as and for the fast and slow hyperpolarization times and likewise,stand for the fast and slow depolarization times respectively (Fig. 8.1**C**). The positions of the peaks, i.e. the values of the characteristic times, were remarkably consistent across all subjects (average ($\pm$s.d.) over all subjects of the positions of the peaks: $\langle T_h^f \rangle = 0.22 \pm 0.01$ s, $\langle T_h^s \rangle = 0.44 \pm 0.01$ s, $\langle T_d^f \rangle = 0.24 \pm 0.01$ s, $\langle T_d^s \rangle = 0.43 \pm 0.02$ s) (Fig. 8.2). Over multiple intracranial contacts, when analyzed one by one, we found exactly the same two peaks in the distributions of T_h and T_d, suggesting that the bimodality cannot be simply explained by regional specificities of different cortical regions (Fig. 8.3). As indicated by the visual inspection of several successive events (Fig. 8.1**B**), the explanation of this bimodality lies in the coexistence of two different types of slow wave events (Fig. 8.4). Examples of scalp EEG signals associated with fast/slow hyperpolarization/depolarization slow wave events are shown in Fig. 8.5.

To confirm these results in a quantitative way, we determined the mode T_h and T_d of each event and obtained its statistical distribution over the whole night. For this purpose we used the Parzen's window method, also known as Kernel density estimation (henceforth referred to as KDE; see Materials and Methods). This method allows to estimate the probability density function, and associated quantities such as the mode, of a certain variable given a finite (and possibly sparse) data sample. In the study of the distributions of modes, two peaks appeared, confirming that there is one slow ($\check{T}^s$) and one fast ($\check{T}^f$) characteristic times for both the hyperpolarization and depolarization processes of a slow wave event: $\langle \check{T}_h^f \rangle = 0.23 \pm 0.01$ s, $\langle \check{T}_h^s \rangle = 0.43 \pm 0.01$ s, $\langle \check{T}_d^f \rangle = 0.26 \pm 0.01$ s, $\langle \check{T}_d^s \rangle = 0.42 \pm 0.02$ s (Fig. 8.6**A**). Furthermore, all these characteristic times were homogenously identified over the course of an entire night of sleep (Fig. 8.6**A**), suggesting that they were not reflecting state-dependent wave shapes (e.g. K-complexes of stage 2 and delta oscillations of stages 3-4) or the effect of the sleep pressure at the beginning of sleep [163]. However, complex laminar propagations of regional slow waves can implicate variable sources located along the cortical layers and may generate fluctuating wave polarities, depending on the spatial relationship between the intracranial electrode and the source of the oscillation [160]. These phase fluctuations could induce missing or double cycles in the slow oscillation that may explain our bimodality. To examine this possibility, we characterized the cortical involvement in the fast/slow hyperpolarization/depolarization events by counting the total number of implicated intracranial contacts. As reported in Fig. 8.7, we found no differences in the average number of contacts during fast and slow events, reflecting in both cases a similar involvement of a large number of cortical sites. This suggests that the bimodality and, in particular, the slow hyperpolarization/depolarization events are not a spurious effect of changing slow waves polarities due to complex propagation pathways of local slow waves.

In order to further study whether slow and fast hyperpolarization/depolarization events reflect different physiological phenomena, we analyzed whether they were associated with differences in the power/amplitude of thalamically-generated spindles (8-18Hz) (Fig. 8.8). For 3 subjects with a good number of slow wave detections we observed that the amplitude of spindle activity after the slow wave minimum was significantly larger during slow-depolarization events, suggesting an implication of the thalamus in these events.

Finally, the present results were obtained in individuals with epilepsy, who may have abnormal synchrony during seizure-free periods in their global activity patterns. In order to confirm the universality of the distributions of T_h and T_d, scalp EEG recordings from 5 healthy subjects were analyzed. In every case, although the two modes were less clearly separated, a bimodal distribution was also observed with very similar peak values to those identified in intracranial data (Fig. 8.9), confirming that epilepsy is unlikely to be the main source of the observed phenomenon.

We examined the existence of temporal relationships between consecutive fast and slow hyperpolarization or depolarization phases via a linear correlation analysis. We found a very weak correlation between T_h and T_d (mean correlation coefficient over all subjects:$\langle \rho \rangle = 0.17 \pm 0.06$, $p < 0.05$) analysing the whole set of intracranial contacts, or between mode T_h and mode T_d ($\langle \rho \rangle = 0.2 \pm 0.1$, $p < 0.05$) of the slow wave events. This weak correlation is clearly observed in Fig. 8.6**B** where T_d is plotted versus T_h and mode T_d versus mode T_h for all the slow wave events of a representative subject. Even though fast hyperpolarization is more frequent, every possible combination of fast/slow hyperpolarization/depolarization can be identified in a slow wave event. In the same way, Fig. 8.6**C** shows the distributions of the total time span $T_h + T_d$ and mode T_h + mode

T_d. The weak correlation is again confirmed by the presence of three peaks representing all possible combinations between fast/slow hyperpolarization/depolarization events. In addition, we found no correlations over groups of temporally adjacent slow wave events. In this case we studied the correlation between the mode hyperpolarization times ($\langle\rho\rangle = 0.24 \pm 0.09$, $p < 0.05$), between the mode depolarization times $\langle\rho\rangle = 0.2 \pm 0.1$, $p < 0.05$) as well as the correlation between the depolarization time of one event and the hyperpolarization time of the following one ($\langle\rho\rangle = 0.14 \pm 0.09$, $p < 0.05$). The observed weak linear correlation suggests that bursts of adjacent fast/slow hyperpolarization/depolarization waves appear in complex sequences during the same sleep stage.

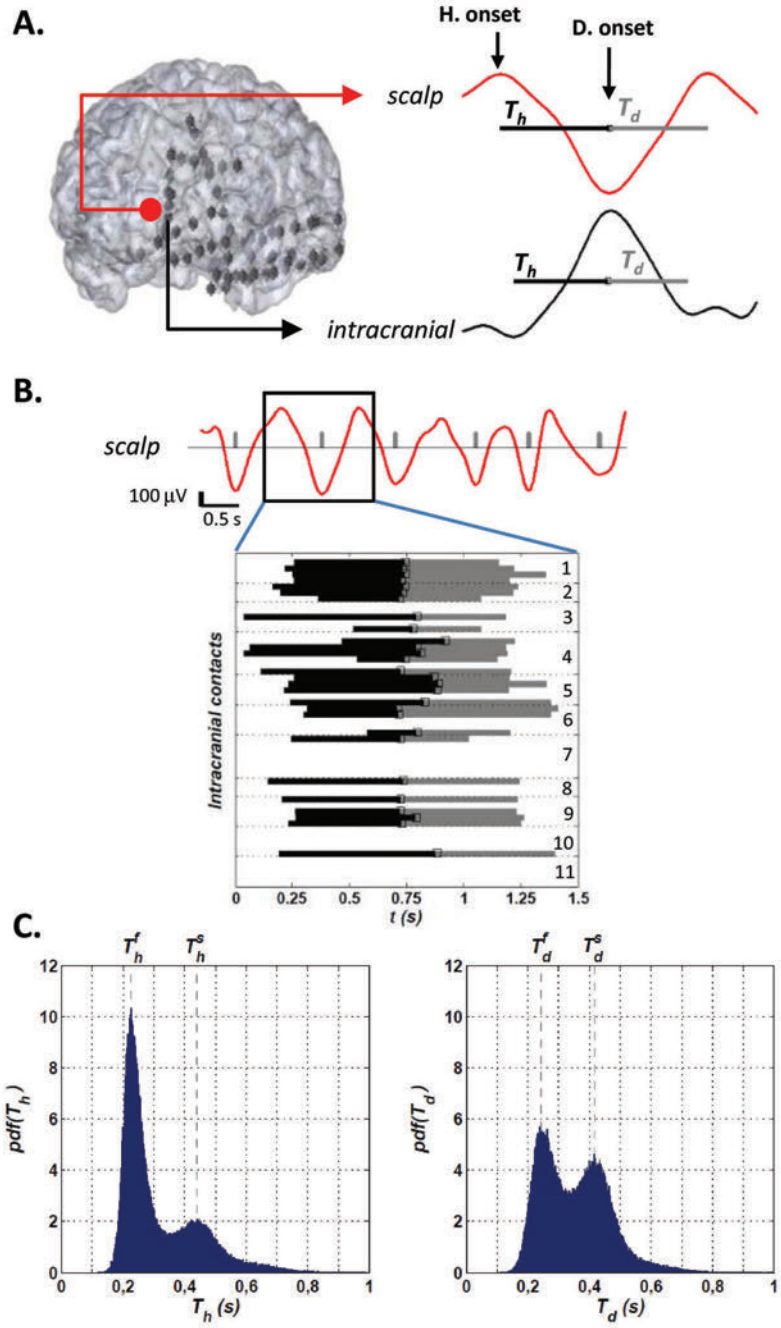

Fig. 8.1 Illustration of the slow wave events detection method and example of T_h/T_d distributions. **A**. Left: 3D reconstructed implantation of one subject. The red circle marks the approximate position of the scalp reference contact. Right: Example of scalp slow oscillation and one of its intracranial correlates (note the polarity inversion of the intracranial signal with respect to scalp). All signals are filtered in the band 0.1-4.0 Hz. The hyperpolarization and depolarization onsets have been marked for the scalp signal. The duration of the hyperpolarization (T_h) and depolarization (T_d) phases of each oscillations is shown as well (black and gray horizontal lines, respectively). **B**. Segment of scalp signal presenting six detected slow waves. For the second detection, the T_h and T_d of the detected intracranial correlates have been plotted. The numbers stand for contacts of the same electrode. This particular implantation consisted of 55 contacts distributed in 11 electrodes. 6 electrodes (n.1-6, 30 contacts) in the left frontal lobe and 5 (n.7-11, 25 contacts) in the left temporal lobe. The contacts in the frontal lobe cover from the F1, F2 and orbital regions to interior regions like the anterior part of the cingulated gyrus, the insula and the cortex subcallosum. The electrodes in the temporal lobe cover different cortical and white matter regions as well as deeper structures like the amygdala and the hippocampus. **C**. Examples of typical Probability Density Functions of T_h and T_d obtained for a single subject. For the construction of the pdfs only the intracranially measured T_h and T_d were taken into account. $T_{h/d}^{f/s}$ mark the position of the fast/slow hyperpolarization/depolarization times of the subject.

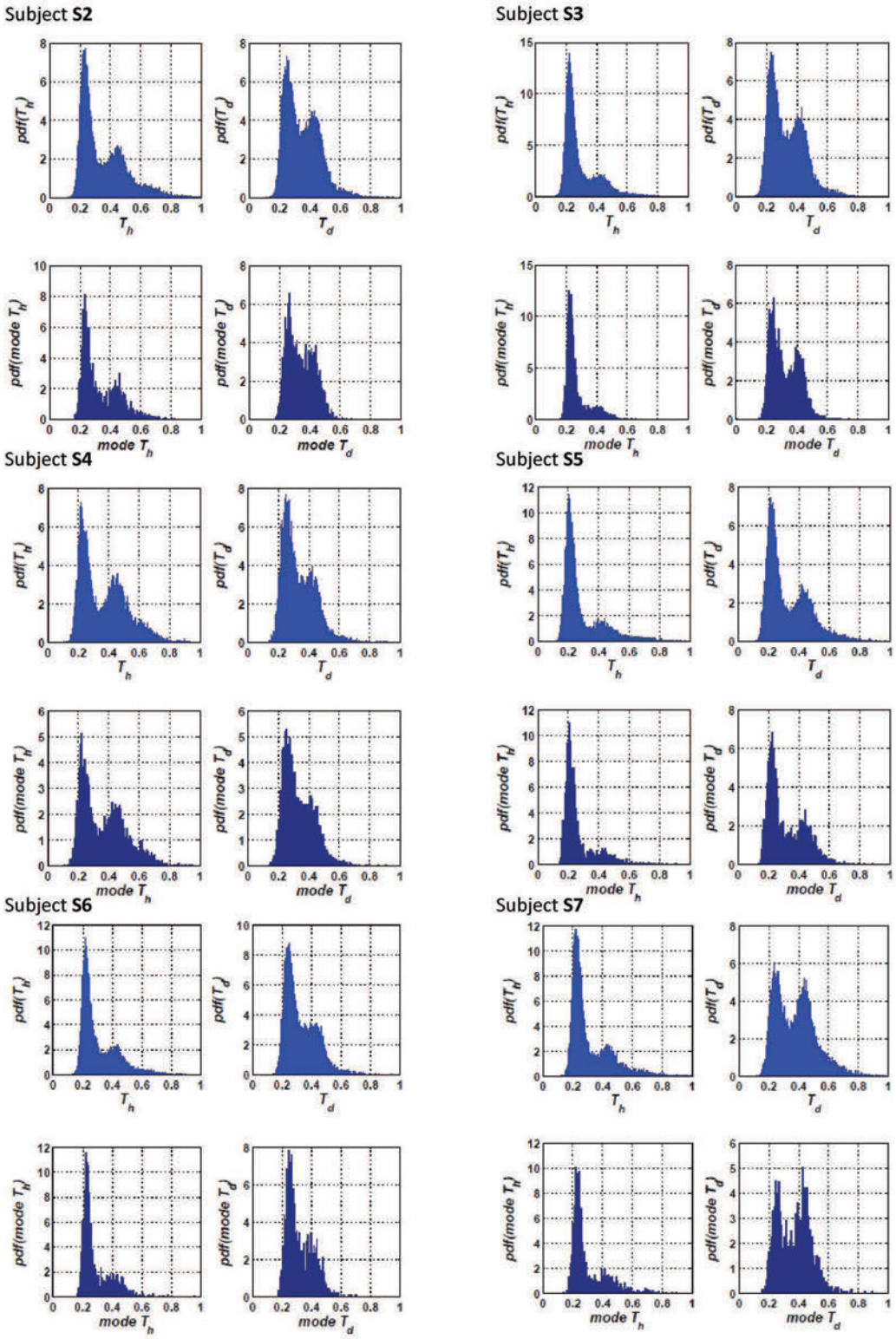

Fig. 8.2 Examples of T_h/T_d and mode T_h/mode T_d distributions. In this figure distributions of T_h/T_d and mode T_h/mode T_d for 6 subjects (S2 to S7) with intracranial electrode implantations (See Table 8.1 for further detail) are shown.

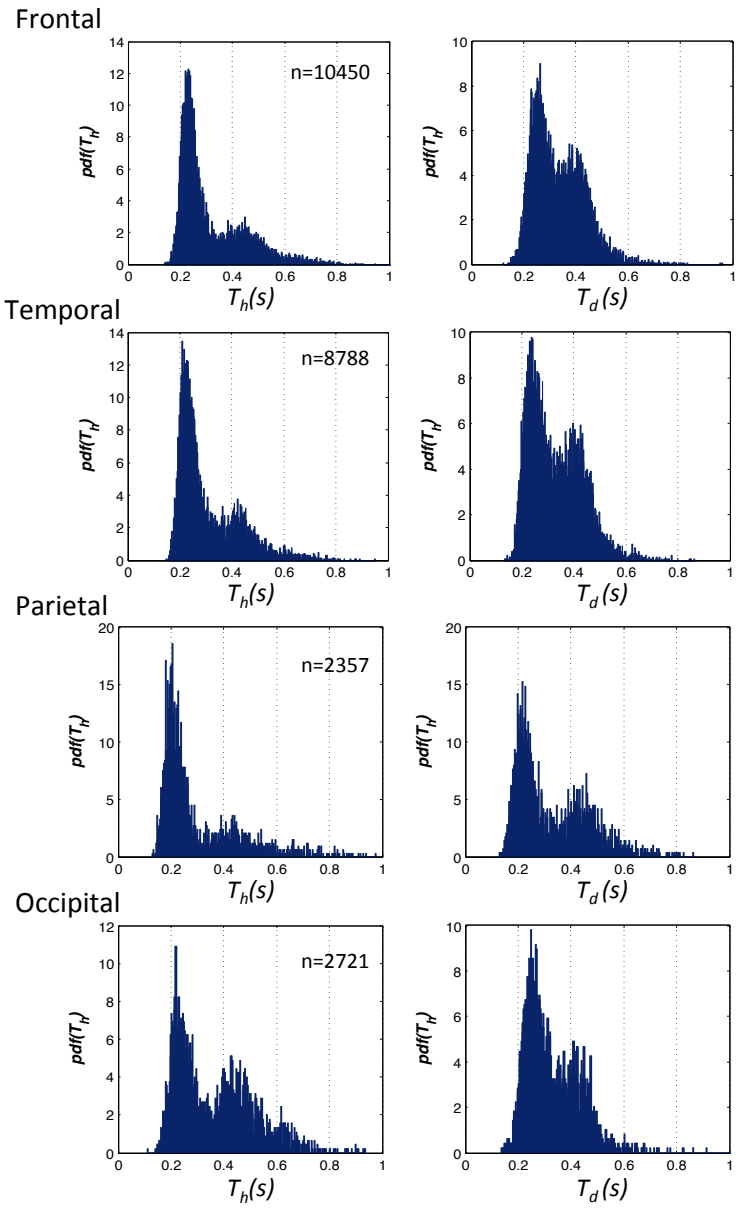

Fig. 8.3 Statistics of T_h and T_d for single intracranial contacts. Histograms of T_h and T_d for four different recording contacts. The first one is situated in the frontal superior cortex, the second in the temporal T1 cortex, the third in the parietal cortex close to the lateral sulcus and the fourth in the occipital O2 cortex. The frontal and temporal contacts correspond to subject S1 (see Table 8.1), the parietal contact to subject S5 and the occipital contact to subject S4.

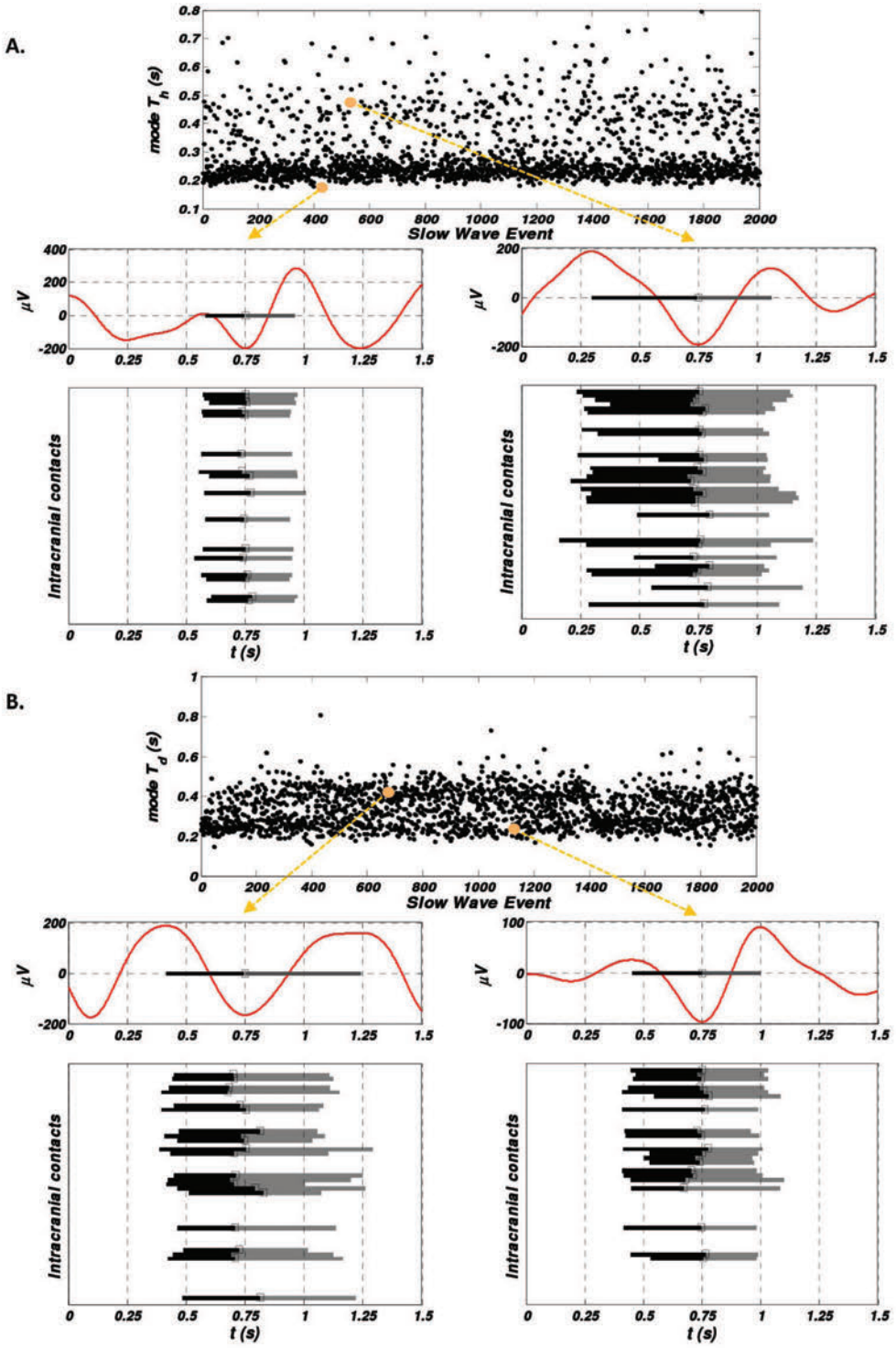

Fig. 8.4 Examples of SW events with different characteristic hyperpolarization and depolarization times. **A**. *Left*: example of a characteristic fast hyperpolarization event. *Right*: Example of a characteristic slow hyperpolarization event. The position of the mode T_h of the events in the probability distribution has been marked in the upper graph. **B**. *Left*: Example of a characteristic slow depolarization event. *Right*: Example of a characteristic fast depolarization event. The position of the mode T_d of the events in the probability distribution has been marked in the upper graph.

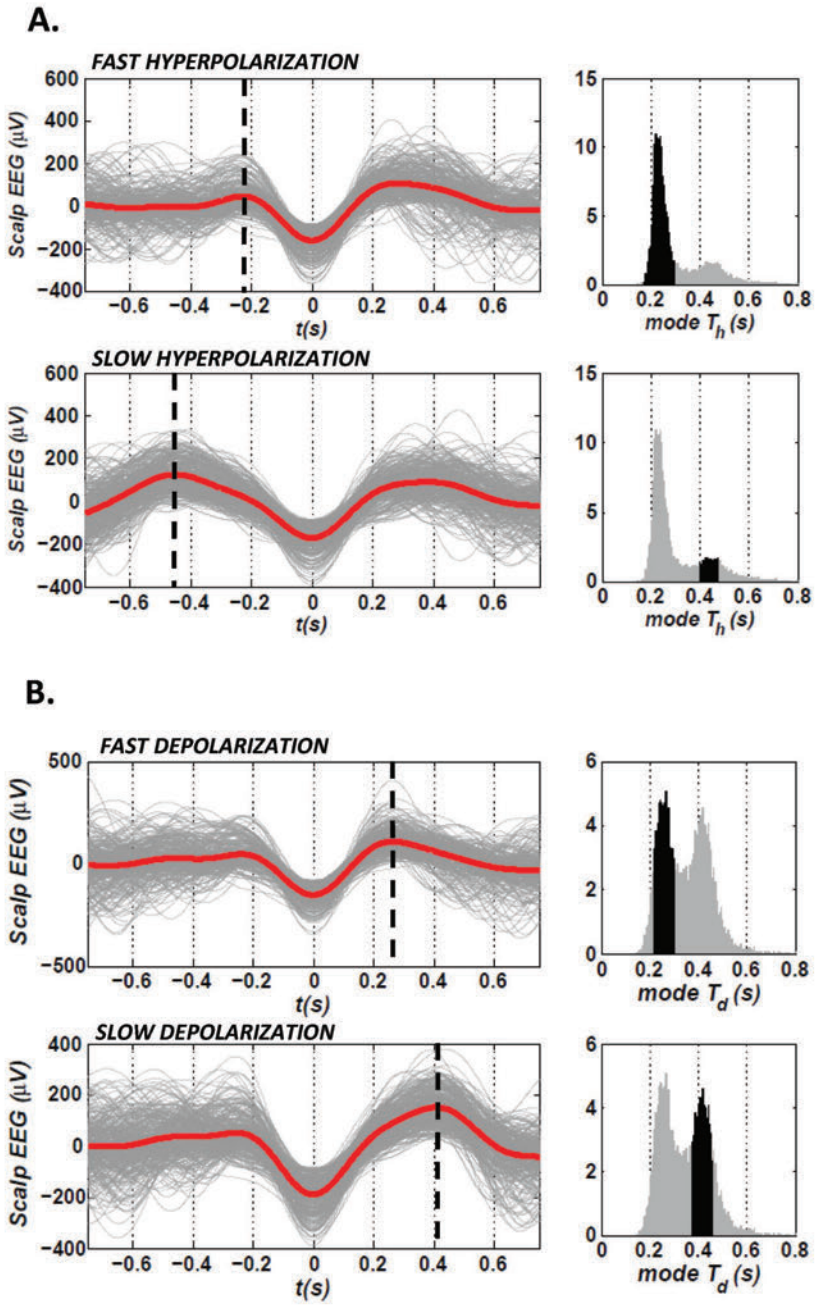

Fig. 8.5 Examples of fast/slow hyperpolarization/depolarization slow waves. **A**. Superposition of filtered signals (0.1-4 Hz) of scalp EEG recordings (FP1) corresponding to 300 slow waves showing fast hyperpolarization (top) and 300 slow waves showing slow hyperpolarization (bottom) of a single subject (S1). The thick red line is the average profile of the shown filtered signals. A vertical dashed line marks the position of the hyperpolarization onset of the average signal. The graphs in the right panels indicate the region in the mode T_h distribution from which the events in the figures have been drawn. **B**. Superposition of filtered signals (0.1-4 Hz) of scalp EEG recordings (FP1) corresponding to 300 slow waves showing fast depolarization (top) and 300 slow waves showing slow depolarization (bottom) of subject S1. The thick red line is the average profile of the shown filtered signals. The vertical dashed line marks the end of the depolarization (as has been defined in the text). The graphs in the right panels indicate the region in the mode T_d distribution from which the events in the figure have been drawn.

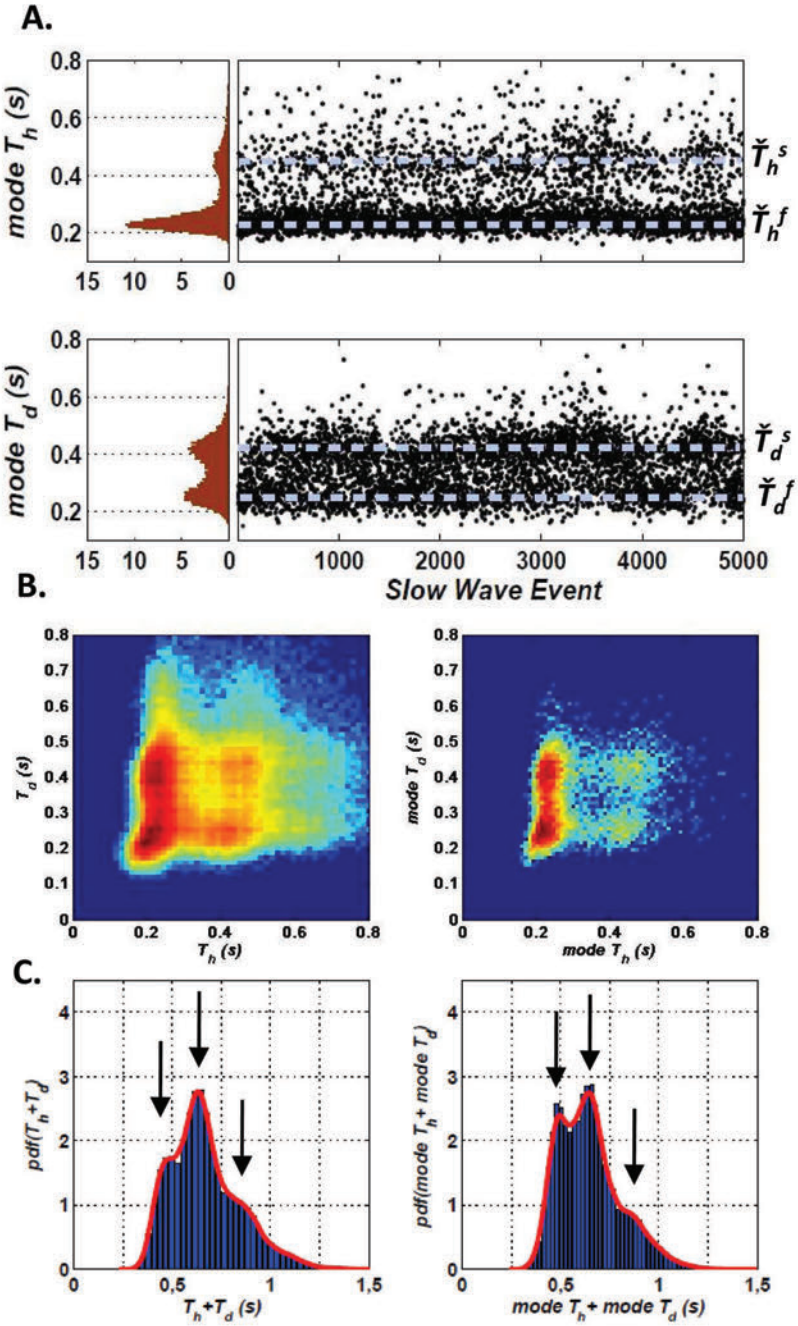

Fig. 8.6 Distributions of mode $T_{h/d}$ and study of the correlation between hyperpolarization and depolarization times. **A**. Mode $T_{h/d}$ Probability Density Functions of a subject and mode $T_{h/d}$ for each of the events detected in a whole night of sleep (5685 events were detected in that particular night of which only the first 5000 are shown). mark the position of the typical fast/slow hyperpolarization/depolarization mode times of the events of the subject. **B**. Left: T_d vs. T_h for a single subject. Right: mode T_d vs. mode T_h for a single subject. (A logarithmic scale has been used in both cases for the density color coding).**C**. Probability Density Function of $(T_h + T_d)$ and (mode T_h + mode T_d). The continuous lines correspond to the estimated PDF using KDE (See Materials and Methods).

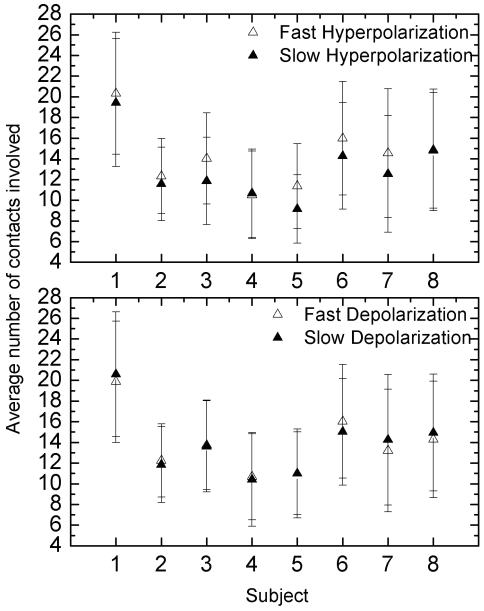

Fig. 8.7 Average number of intracranial contacts involved in the detection of fast/slow hyperpolarization/depolarization events. The averages shown were calculated for eight subjects (S1 to S8 in Table 8.1) for their fast/slow hyperpolarization (upper panel) and depolarization (lower panel) events.

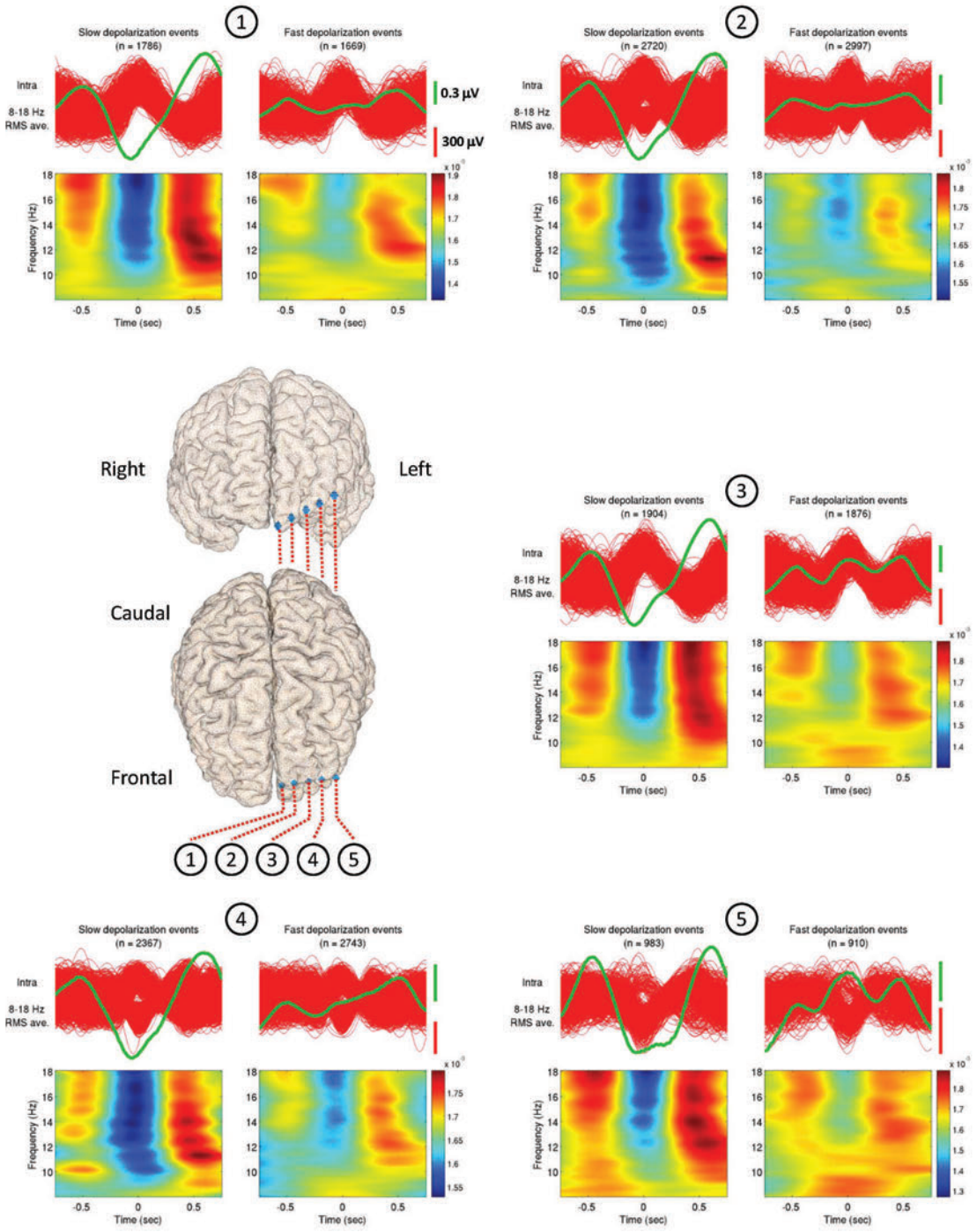

Fig. 8.8 Analysis of thalamically-generated spindles during fast and slow depolarization events. Each panel (from 1 to 5) corresponds to one contact of an intracranial electrode (blue dots in the anatomical figure). Fast and slow depolarization events are studied separately. In each panel from top to bottom : Filtered signals (0.1 - 4 Hz) of the detected slow waves aligned around their central peak (red) with the average RMS activity (green line) in the band 8-18 Hz; Average of their time-frequency representations.

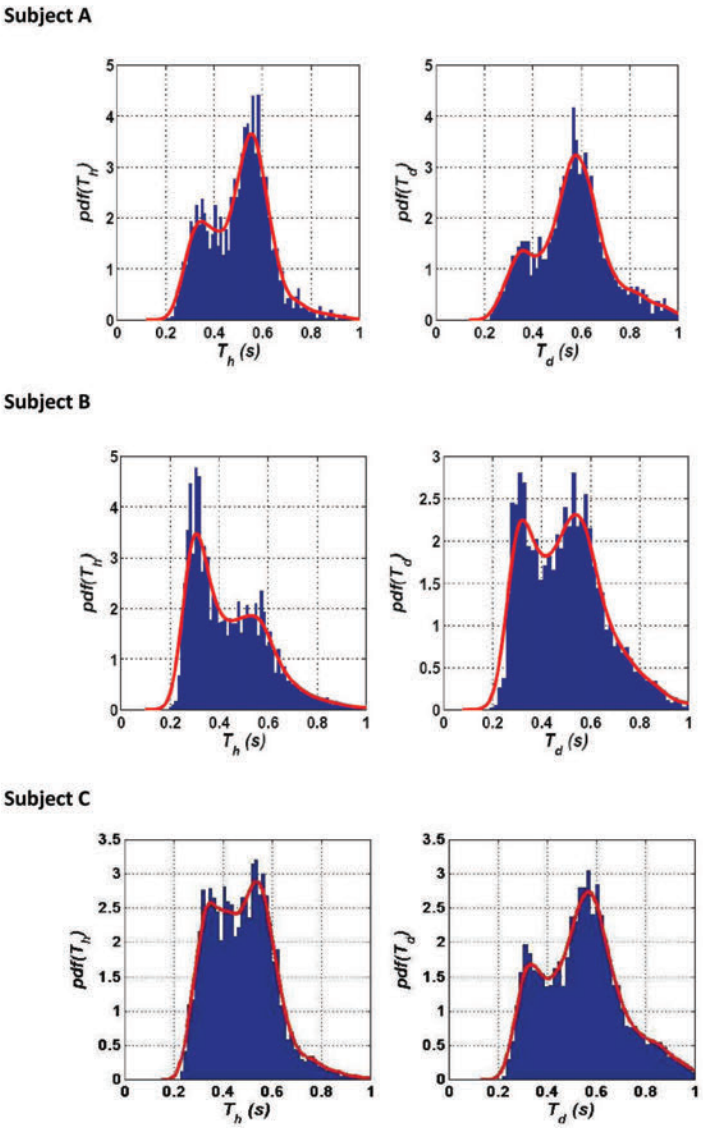

Fig. 8.9 Examples of T_h and T_d distributions for three healthy patients. These distributions have been obtained from the analysis of 3 nights of sleep scalp-EEG recordings for each patient.

8.3 Hyperpolarization and depolarization propagation velocity

Traditionally, the propagation of slow waves (Fig. 8.10) has been studied as the propagation of a depolarization wave (D-wave) [144]. We have indeed observed this propagation in our intracranial data. Fig. 8.10 illustrates the propagation of a global slow wave event and three local propagation patterns. In this work we have also taken into account the hyperpolarization process that precedes the depolarization onset and considered the hyperpolarization as a traveling wave phenomenon (H-wave). The propagation velocity of both waves has been estimated with two methods.

The first method consisted in the calculation of the instantaneous velocity of the slow wave. Given two consecutive detections of the same slow wave event, the speed was calculated from the distance between two contact locations, normalized to Talairach coordinate space [164], and the known time delay between the corresponding detections. This method assumes linear propagation of the waves and does not take into account particular characteristics of the cerebral cortex such as its convoluted surface. In order to reduce the error in the estimation of the speed we imposed a maximum distance threshold (40 mm) between the detection contacts. Histograms of the instantaneous speed were obtained for each subject and each type of wave. All histograms showed a clear mode peak, the exact value of which was estimated using KDE (an example can be seen in Fig. 8.8). The mode velocity of the H-wave ranged from 0.35 to 0.56 m/s across subjects with a grand average of 0.5 ± 0.1 m/s. For the D-wave, the mode velocity was inside the range 0.8-1.5 m/s and provided a grand average of 1.0 ± 0.2 m/s. As we already mentioned, this method may provide underestimations of the traveling speeds due to the assumption of rectilinear propagation of the slow wave between the contacts.

To further reduce the effect of these assumptions, we performed a second estimation. In this case we selected, for different subjects, pairs of close intracranial contacts (separation less than 15 mm) with a good percentage of detections. We then estimated the mean contact-to-contact velocity for each pair. A total number of 10 pairs of 7 different subjects were studied. The mean H-wave velocity ranged from 0.7 to 1.6 m/s with a grand average of 1.0 ± 0.3 m/s. The D-wave mean speed ranged from 0.9 to 1.9 m/s with a grand average of 1.3 ± 0.4 m/s. As expected, this second method provided larger estimates for the velocities.

Using both estimations, we were not able to find any differences in the propagation velocities between fast- and slow-depolarization waves. A more refined description of their anatomical pathways is here needed to study subtle differences in their propagation speed.

8.4 Origin and Propagation paths in networks of hubs

Close inspection of our data confirmed that the dynamics of the traveling slow wave are very far from the simple dynamics of a plane or spherical wave with a point-like and stable origin [145]. In particular, each slow wave event is also unique in its origin and dynamics. Furthermore, our data confirmed that slow waves are not a global entrainment of all cortical regions via a single propagating wave but are often composed of complex local patterns with multiple points of origin.

In order to deal with this complexity, we identified for each subject the set of intracranial contacts that were statistically more involved in all detected events, i.e. contacts

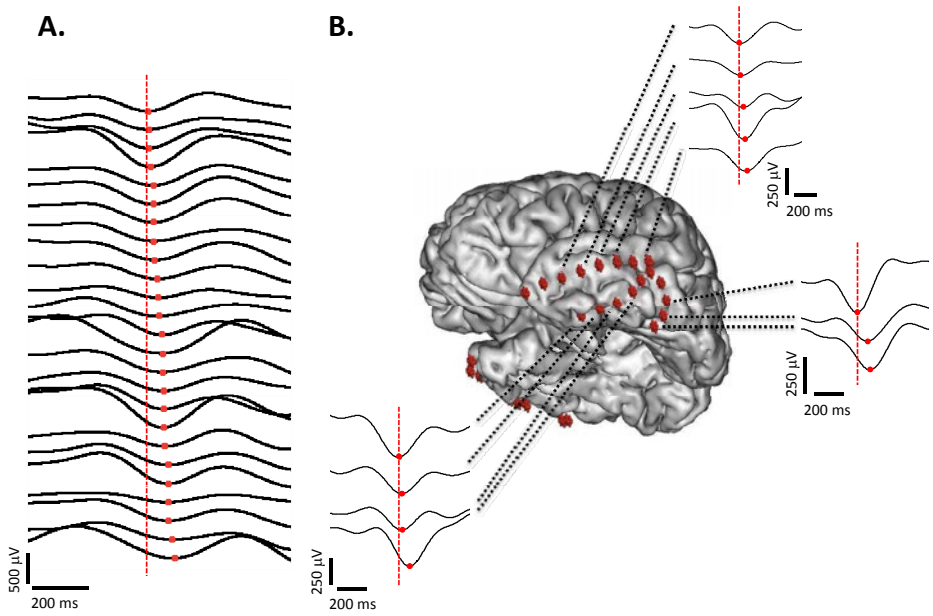

Fig. 8.10 **A**. Filtered (0.1-4 Hz) signals of intracranial EEG contacts of one global slow wave event ordered as a function of the position of the minimum (red dots). The vertical dashed line marks the position of the minimum of the first detection. **B**. Three examples of local propagation in the temporal lobe. Each example corresponds to a different slow wave event. In all cases the signals are linked to the position of the recording contacts in the brain, represented by red cubes.

with a number of detections of at least one standard deviation above the mean. Defined in the network of slow wave propagations (the intracranial contacts acting as nodes and the links being causally related detections), these contacts can be seen as hubs since they would be the most connected nodes.

We have studied the propagation by examining in which order each event visited these hubs. We have also calculated in which ordinal position (first, second, etc.) each hub was more likely to have been visited by analyzing the statistics over all the events. Finally, linking the first hubs with the second hubs, the second hubs with the third ones, etc., a directed graph could be constructed that established a causal relation between the hubs and hence a statistical propagation trend for each subject (Fig. 8.11).

In Fig. 8.12**A**, the first (blue spheres) and last hubs (red crosses) of all subjects have been superimposed on a single cortical reconstruction. We have found no major differences for the propagation of H- and D-waves. For both the H-wave and the D-wave we found 35 first hubs and only 15 last hubs of a total of 417 contacts. In our opinion, this is a sign of the greater heterogeneity of the starting location of the slow waves. The majority of the first hubs were located in the anterior parts of the brain while the last hubs seemed to prefer the posterior parts. In particular, for the H-wave, we found 17 first hubs in the frontal lobe, 3 in the cingulate cortex, 12.5 in the temporal lobe and 2.5 in the occipital lobe (consistently with Table 8.1, contacts between two adjacent regions are considered as half in each one). The last hubs, on the contrary, were more present in posterior parts of the brain with 7 in the temporal lobe, 3 in the occipital region, 1 in

the parietal lobe and only 4 situated in the frontal lobe. The results for the D-wave were similar with 20 of the 35 first hubs situated in the frontal lobe, 2 in the cingulate cortex, 11.5 in the temporal lobe and 1.5 in the occipital lobe. The last hubs of the D-wave were also more frequent in posterior regions with 7 in the temporal lob and 2 in the occipital cortex (the rest were located 4.5 in the frontal cortex, 1 in the parietal and 0.5 in the cingulate cortex) (Fig. 8.12**B**). Even though the origin of the slow wave events could be very unordered, we identified a last-hubs-free region in the frontal cortex where first hubs tended to concentrate (F1/F2 cortex involving the superior frontal gyrus and the superior frontal sulcus).

In Fig. 8.12**A** a certain lateralization can be observed with more first hubs in the left hemisphere but this can be explained by the inhomogeneous distribution of the intracranial contacts with 295 (71%) located in the left hemisphere and only 122 (29%) implanted in the right hemisphere. Studies with a larger number of subjects or with a better spatial resolution are needed to confirm these results.

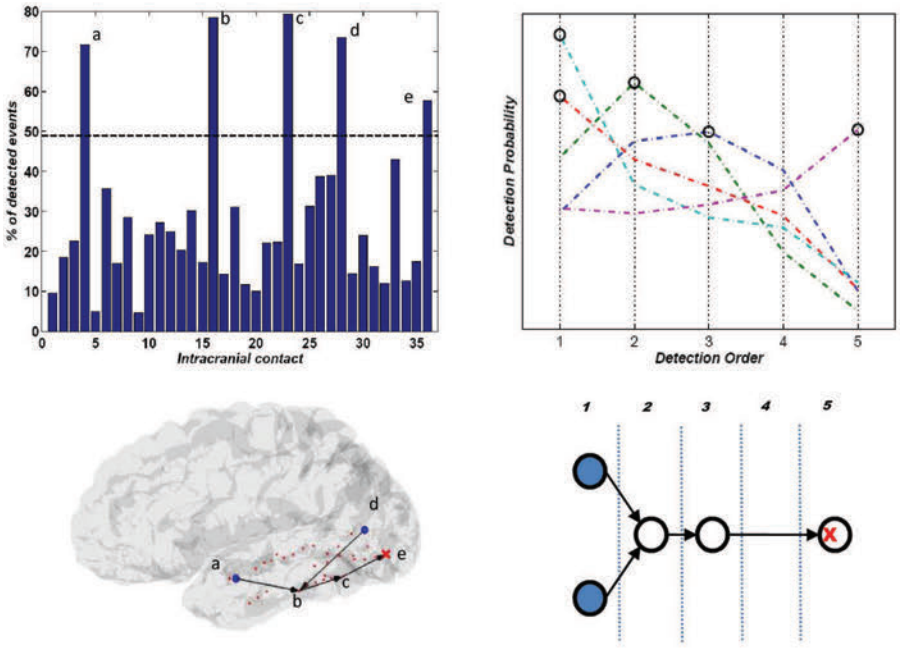

Fig. 8.11 Illustration of the method for the study of the propagation. *Top left*: Percentage of the total number of events of a subject (S5) detected by each of its intracranial contacts. The dashed line corresponds to the threshold of one standard deviation. *Top right*: Detection probability vs. order of detection for each hub. This probability has been calculated over all the events of the subject. The black circles point the position of maximum detection probability of each hub. *Bottom*: Reconstruction of the directed graph on the intracranial implantation (temporal implantation in this case) and a schematic representation of the graph construction procedure. The blue spheres mark the hubs that preferentially perform the first detection and the red crosses mark the hubs that preferentially perform the last ones.

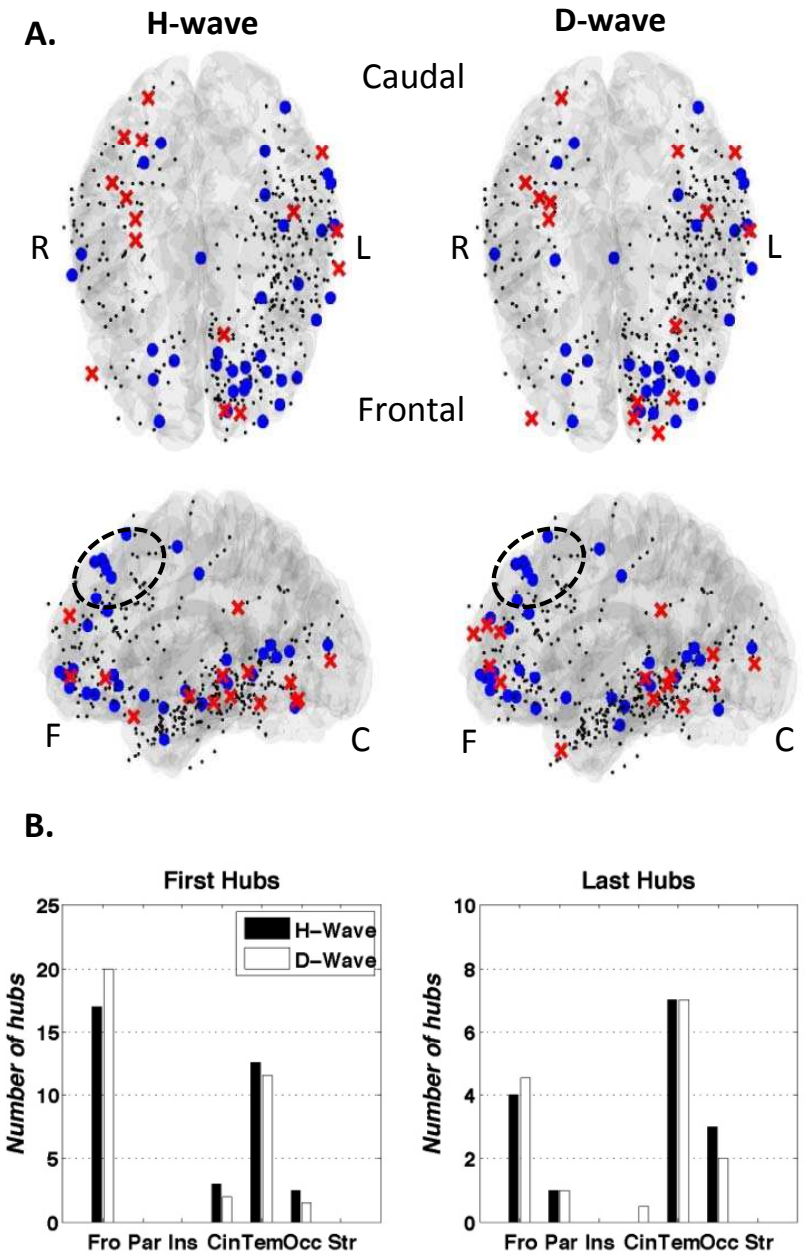

Fig. 8.12 Results of the propagation study. **A**. *Left*: First and last hubs of the H-wave propagation of all studied subjects superimposed on the same reference brain (Top and left views). *Right*: First and last hubs of the D-wave propagation of all studied subjects superimposed on the same reference brain (Top and left views). The little black dots correspond to the implanted contacts not presenting a first/last hub character. These are shown to illustrate the total coverage of the sum of the individual implantations. Please note the final coverage of the sum of all the implantations is not homogeneous with 295 (71%) contacts is the left hemisphere and 122 (29%) in the right hemisphere. **B**. Graphs of the percentages of first/last hubs found in each of the following regions: Frontal (Fro), Parietal(Par), Insula(Ins), Cingulate cortex(Cin), Temporal(Tem), Occipital(Occ) and Striatum(Str).

8.5 Discussion

In this chapter we have explored the large-scale dynamics of sleep slow waves in the human cortex using intracranial EEG recordings. We report the following observations: 1) The hyperpolarization and depolarization processes have two distinct characteristic times. 2) A weak linear correlation could be identified between consecutive fast/slow hyperpolarization or depolarization phases. 3) Using two complementary methods, we estimated the average speed of both traveling waves as approximately 0.5 ± 0.1 m/s (H-wave) and 1.0 ± 0.2 m/s (D-wave) (1.0 ± 0.3 m/s and 1.3 ± 0.4 m/s, respectively). 4) For both waves, preferential starting locations were located in the anterior parts of the brain while they have a tendency to end in the posterior and temporal regions.

Aside from descriptive statistics of slow waves, the first new finding of this work was the determination of two characteristic times for both the hyperpolarization and depolarization processes. These slow and fast processes were remarkably consistent across all subjects and did not show significant correlation with regional specificities of different cortical regions or different sleep stages (considering III and IV as separate stages). A strong support of the physiological existence of this phenomenon is given by our analysis of scalp slow waves of healthy subjects that also exhibit a bimodality of hyperpolarization and depolarization times. This suggests that the bimodality is not related to the epileptic condition of our intracranially recorded subjects. Moreover, the demonstration of the bimodality from scalp EEG recordings allows us to discard the possibility that this phenomenon might be caused by fluctuating wave polarities around the recording intracranial sites [160, 161] since the scalp electrodes are well over the cortical generators of slow waves. To further confirm this point we calculated the average number of contacts involved in the detection of fast and slow events. We found that both events involve a similar number of cortical sites, suggesting that the bimodality can not be explained by changing propagation pathways across the cortical layers giving rise to missing or double cycles in the recorded signal. Finally, we found a weak linear correlation between consecutive fast and slow hyperpolarization or depolarization phases, suggesting that these events appear in a mixed and complex way during the same sleep stage. We conjecture that nonlinear relations might exist between these two processes, particularly long-range temporal correlations at time scales of several minutes [165]. It is important to note that, in this study, the association of the up and down phases of the slow wave with the cellular hyperpolarization and depolarization processes is a hypothesis in nature since we have not correlated our data with intracellular recordings. As also assumed in other studies [144], this association is suggested by previous observations correlating cellular and EEG activity [141, 151]. However, further investigations at a cellular level in the human brain are necessary to validate these hypotheses [161].

The underlying causes of this novel bimodality of slow waves are still unclear. A possible explanation is that they could be related to the influences of subcortical regions on cortical synchrony. Indeed, although slow waves are generated within the cortex, as shown in animals with thalamic lesions [150] and confirmed in decorticated animals [166], recent data suggest a role of thalamic activity in triggering cortical slow waves through thalamocortical connections [153, 167, 168]. In particular, in cortical networks that lack thalamic input, i.e. cortical slabs [169] or slices [149], the hyperpolarization wave is considerably longer than if thalamic input is present. Furthermore, the mean duration of the depolarization phases increases with thalamic inputs [168], as also suggested by computational models [170]. Therefore, fast hyperpolarization or slow depolarization times could reflect the different implication of the thalamus. Preliminary anal-

yses of the amplitude of spindle activity (8-18Hz) around the slow wave minimum show differences in this frequency band between slow- and fast-depolarization slow wave events. In particular, for a small group of selected patients, we observed that slow depolarization events are accompanied by a strong and well-organized spindle activity ($\approx$12 – 16 Hz) coinciding with cortical up-states (see Fig. 8.8). On the contrary, fast depolarization events show a more diffuse spindle activity at cortical up-states but an alpha-like activity ($\approx$ 8 – 10 Hz) can be seen coinciding with the depolarization onset. This mixture of activities related to fast-depolarization waves could suggest a similarity of these types of events with K-Complexes or micro-awaking episodes occurring during the active phase of the Cycle Alternating Patterns (CAP) [171]. In the CAP K-Complexes as well as other faster activities, including spindles, are present. In our opinion, these differences concerning spindle activity between slow and fast-depolarization waves reinforce the hypothesis of a distinct implication of the thalamus in these two different events. However, further work in this direction is needed to fully clarify the role of the thalamus in each type of slow wave processes.

Our second result is the direct estimation of the propagation speed of hyperpolarization and depolarization waves on the cortex. Using two different methods, we estimated the typical speed of both waves as 1 m/s. Interestingly, although this speed is of the same order of magnitude as previous estimates from EEG (2.7 m/s in [144]; 2.2 m/s in [145]) and computer simulations [172], the obtained values are somewhat smaller than previously published estimates of the depolarization propagation speed in humans. Linear interactions of voltages inherent in scalp EEG recordings [144] or their overlapping in source modeling [145] are most likely responsible for an overestimation of the intracranial propagation speed. However, our reported propagations were faster than the average speed estimated to be around 0.1 m/s in multi-site recordings of different cortical areas of anesthetized cats [173]. Our higher speeds may reflect not only a slight overestimation due to obliquely propagating waves or volume conduction [144], but also a higher speed of propagation in the human cortex secondary to its widespread long-range connectivity. Indeed, the speed of propagation in ferret cortical slices is low, around 0.01 m/s, given that it relies exclusively on local connectivity [149].

Our data were recorded in medicated epilepsy patients in whom the propagation of slow waves may be affected by epileptic disturbances. Nevertheless, as several other sleep studies using intracranial data [160, 161], we believe that the effects of pathology on our results are minor for the following reasons. First, high epileptic activities were visually identified and removed from our data. Second, as imposed by our automatic detection, slow wave dynamics were within the expected normal range, including standard morphologies, durations, amplitudes and spatial extent. Third, from the total number of intracranial contacts, 83% were located outside the epileptogenic zone. Finally, interictal epileptic events have markedly different temporal dynamics with an extremely fast synchronization but more limited in their spatial extent. The propagations we describe here showed remarkable global dynamics, reproducible from one patient to another. In addition, there are clear parallels between the results of [145] and our data. In both studies, spontaneous slow waves were reported to propagate across the cortical area.

Nevertheless, a high spatial variability of the propagation was found. In particular, slow waves were composed of multiple propagation paths which can vary from one wave to another and with several points of origin [146]. This variable network of propagations may reflect the level of activity-dependent synchronization achieved in cortical neural ensembles, which depends on the local homeostatically regulated average synaptic strength [174]. In our work, we have chosen to reduce this complexity by only study-

ing the preferential trajectories between intracranial sites statistically more involved in slow waves. We found that, for both hyperpolarization and depolarization waves, the majority of the first hubs were localized in the anterior parts of the brain while the last hubs seemed to prefer the posterior parts. This further confirms the presence of cortical generators in the frontal cortex with enhanced intrinsic excitability, which could consistently generate slow waves during sleep.

Subject	Total implanted contacts							Contacts in the epileptic ictal zone							Contacts in the epileptic interictal zone						
	Fro	**Par**	**Occ**	**Tem**	**Cin**	**Ins**	**Str**	**Fro**	**Par**	**Occ**	**Tem**	**Cin**	**Ins**	**Str**	**Fro**	**Par**	**Occ**	**Tem**	**Cin**	**Ins**	**Str**
S1	18	0	0	25	9	1,5	1,5	2	0	0	2	4	1	1	3	0	0	10	0	0	0
S2	27	0	0	0	2	2	0	3	0	0	0	0	0	0	3	0	0	10	0	0	0
S3	24,5	0	0	13	2,5	1	0	6	0	0	1	0	1	0	6	0	0	11	0	0	0
S4	0	4,5	4,5	17	0	0	0	0	4,5	1,5	2	0	0	0	0	2	2,5	8,5	0	0	0
S5	17	6	0	3	2	3	0	0	0	0	2	0	1	0	3	0	0	0	0	2	0
S6	17,5	0	7	16	4	0,5	0	8,5	0	0	0	3,5	0	0	4	0	1	2	0	0	0
S7	0	1,5	0	48	0,5	0	0	0	0	0	5	0	0	0	0	0	0	17,5	0,5	0	0
S8	0	0	7,5	48,5	0	0	0	0	0	0	7	0	0	0	0	0	0	24	0	0	0
S9	0	0	0	36	0	0	0	0	0	0	8	0	0	0	0	0	0	10	0	0	0
S10	18	0	0	25	3	0	0	5	0	0	0	1	0	0	0,5	0	0	10	0,5	0	0
Total	122	12	19	232	23	8	1,5	24,5	4,5	1,5	27	8,5	3	1	19,5	2	3,5	93	1	2	0

Table 8.1 Details of the intracranial implantations. Contacts in the epileptic ictal zone correspond here to contacts associated to seizure onsets. Contacts in the epileptic interictal zone correspond here to contacts associated to epileptic spikes during interictal periods. Contacts between two adjacent regions were considered as half in each one. Legend: Fro (Frontal), Par (Parietal), Occ (Occipital), Cin (Cingulate), Ins (Insula), Str (Striatum).

Appendix E
Materials and methods

E.1 Subjects and EEG acquisition

For the intracranial study, the sleep EEG recordings of 10 subjects (5 Females; age range, 18-49; Mean Age = 32,9) with refractory partial epilepsy undergoing presurgical evaluation, hospitalized between February 2002 and July 2007 in the epilepsy unit at the Pitié-Salpêtrière hospital in Paris, were analyzed. Each patient was continuously explored during several days with intracranial and scalp electrodes (Nicolet acquisition system, CA, US) . Depth electrodes were composed of 4 to 10 cylindrical contacts 2.3 mm long, 1 mm in diameter, 10 mm apart center-to-center, mounted on a 1 mm wide flexible plastic probe. Subdural electrodes were strips with 4 to 8 one-sided circular contacts, 2.3 mm in diameter and with a center-to-center separation of 10 mm. The effective surface area was 7.2 mm^2 for depth contacts and 4.15 mm^2 for subdural contacts. Pre and post implantation MRI scans were evaluated to anatomically and precisely locate each contact along the electrode trajectory. Talairach coordinates of intracranial contacts were estimated with the BrainVisa/Anatomist software package (http://brainvisa.info/). The placement of electrodes within each patient was determined solely by clinical criteria; however, the routine clinical use of broad anatomical coverage for intracranial recordings provided a large sample of electrophysiological data from tissue outside of the epileptogenic zone. In particular, a total number of 417 intracranial contacts were analyzed from which 83% were located outside the epileptogenic zone. The intracranial contacts were distributed in the different brain regions in the following way: 122 in Frontal regions, 12 in Parietal regions, 19 in Occipital regions, 231.5 in Temporal regions, 23 in the Cingulate cortex, 8 in the Insula and 1.5 in the Striatum (contacts between two adjacent regions were considered as half in each one). Signals were digitalized at 400 Hz. Common average reference montage was chosen to normalize the signals. Noisy electrodes and those presenting high epileptic activity were excluded from the average by visual inspection. A data set of 22 complete nights of sleep with at least two complete sleep cycles was obtained with each subject contributing with 2-3 nights. Each night was scored for sleep stages using the software Somnologica^{TM}. All patients gave their informed consent and procedures were approved by the local ethical committee (CCP).

Scalp sleep EEG recordings of 5 male healthy subjects were also analyzed. For each subject, 3 complete nights were studied. Electrographic (EEG), electro-oculogram (EOG) and chin electro-myogram (EMG) activity were concurrently monitored and used to classify the different sleep states.

Digital bandpass filtering between frequencies $f_1 - f_2$ was, in all cases, implemented through a forward-backward digital infinite impulse response (IIR) type II Chebyshev

filter (passband: $f_1 \leq f \leq f_2$ Hz, attenuation ≤ 1 dB, monotonic; stopband: $f \leq (f_1 - k)$ or $f \geq (f_2 + k)$ Hz, where $k = 0.5$ for $f_{1,2} \geq 1$ Hz or $k = 0.05$ otherwise, attenuation ≥ 100 dB, equiripple). Electrical line noise at 50 Hz was suppressed by a bandstop filter of the same type. All analyses were implemented in MATLAB (The MathWorks^{TM}, MA, USA).

E.2 Sleep Oscillations detection criteria

For the intracranial-EEG subjects, the Slow Oscillations were first detected from a single scalp electrode and only from segments of NREM sleep. Since not all subjects shared exactly the same number of scalp electrodes, FP1 was chosen for the analysis because it was systematically recorded and because it had been previously used for studying slow wave activity [163]. For the automatic detection of the slow waves, all signals were bandpass-filtered between $0.1 - 4Hz$. The criteria for the automatic detection in the scalp EEG were chosen following those in the literature [144, 145]: (1) separation between the negative zero crossing and the subsequent positive zero crossing of 0.125-1.0 s; (2) separation between the positive zero crossing and the following negative zero crossing of 0.125-1.5 s; (3) negative peak between the first two zero crossings with a voltage $V \in [-400, -80]\mu V$; (4) a negative to positive peak-to-peak amplitude $> 140\mu V$. We disregarded the cases presenting more than one minimum between the crossings. Once a slow oscillation was detected in the Scalp EEG, a correlation study was performed to determine which other intracranial contacts had detected that particular slow wave as well. We opened a 1.5 s window around the scalp minimum and we calculated the correlation coefficient between the scalp signal and the intracranial contacts signal. We assume an intracranial electrode detected the slow oscillation if the absolute value of the correlation coefficient is > 0.6 and the amplitude of the minimum (maximum in the case of inversion) has a magnitude at least 25% of that in scalp. We identified a slow wave event when at least 40% of the active contacts detected the slow oscillation.

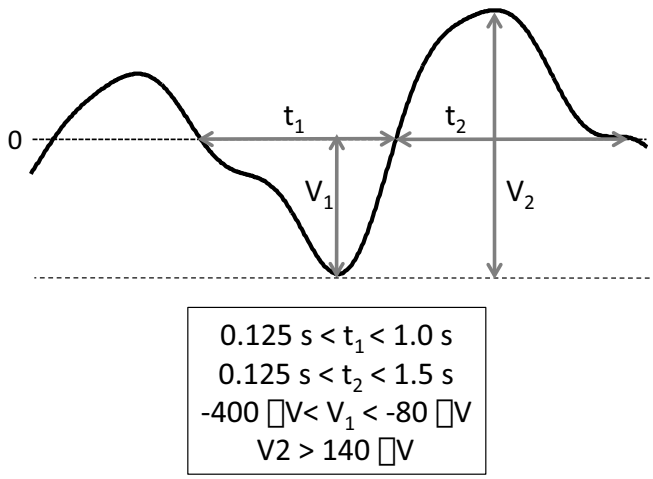

Fig. E.1 Illustration of the criteria used for the automatic detection of sleep slow oscillations.

For the scalp-EEG subjects, the Slow Oscillations were first detected from the C3 electrode. The criteria for the detection were the same as in the intracranial case. Similarly to the intracranial case, a correlation study was performed to determine which scalp contacts had also detected the slow wave event.

E.3 Kernel Density Estimation

Kernel density estimation is a method for the estimation of probability density functions and modes [174].

The theoretical basis of the KDE method is the following: Given a set of i.i.d. sampled values of a random variable X_1, X_2, X_3... we can estimate the corresponding probability density function as

$$f_n(x) = \frac{1}{nh} \sum_{j=1}^{n} K\left(\frac{x - X_j}{h}\right) \tag{E.1}$$

where $K(\dots)$ is called the kernel and h the bandwidth. The kernel is usually chosen to be of a Gaussian type

$$K\left(\frac{x - X_j}{h}\right) = \frac{1}{\sqrt{2\pi}} \exp -\frac{1}{2}\left(\frac{x - X_j}{h}\right)^2 \tag{E.2}$$

We have implemented this method using the function *ksdensity* of the software package MATLAB (The MathWorks^{TM}, MA, USA).

References

1. V. Botella-Soler, J.A. Oteo, and J. Ros. Dynamics of a map with a power-law tail. *J. Phys. A: Math. Theor.*, 42:385101, 2009.
2. V. Botella-Soler, J.M. Castelo, J.A. Oteo, and J. Ros. Bifurcations in the lozi map. *J. Phys. A: Math. Theor.*, 44:305101, 2011.
3. V. Botella-Soler, J.A. Oteo, and J. Ros. Coexistence of periods in a bifurcation. *Chaos Soliton. Fract.*, 2012.
4. V. Botella-Soler and P. Glendinning. Emergence of hierarchical networks and polysynchronous behaviour in simple adaptive systems. *Europhys. Lett.*, 97:50004, 2012.
5. V. Botella-Soler, M. Valderrama, B. Crépon, V. Navarro, and M. Le Van Quyen. Large-scale cortical dynamics of sleep slow waves. *PLoS ONE*, 7(2):e30757, 2012.
6. A. Celletti and E. Perozzi. *Celestial mechanics: the waltz of the planets*. Springer Verlag, 2007.
7. E.N. Lorenz. Deterministic non-periodic flow. *J. Atmos. Sci.*, 20:130–141, 1963.
8. S.H. Strogatz. *Nonlinear dynamics and chaos: With applications to physics, biology, chemistry, and engineering*. Westview Pr., 2000.
9. T.Y. Li and J.A. Yorke. Period three implies chaos. *Am. Math. Mon.*, 82:985–992, 1975.
10. M. Ausloos and M. Dirickx. *The logistic map and the route to chaos: from the beginnings to modern applications*. Springer Verlag, 2006.
11. R.M. May. Simple mathematical models with very complicated dynamics. *Nature*, 261:459–467, 1976.
12. M.J. Feigenbaum. Quantitative universality for a class of nonlinear transformations. *J. Stat. Phys.*, 19:25–52, 1978.
13. M.J. Feigenbaum. The universal metric properties of nonlinear transformations. *J. Stat. Phys.*, 21:669–706, 1979.
14. R.L. Devaney. *An introduction to chaotic dynamical systems*. Addison-Wesley, 1989.
15. N. Metropolis, M.L. Stein, and P.R. Stein. On finite limit sets for transformations on the unit interval. *J. Comb.Theory A*, 15:25–44, 1973.
16. M. Romera. *Técnica de los sistemas dinàmicos discretos*. CSIC, 1997.
17. S. Wiggins. *Introduction to applied nonlinear dynamical systems and chaos*, volume 2. Springer Verlag, 2003.
18. C. Grebogi, E. Ott, and J.A. Yorke. Chaotic attractors in crisis. *Phys. Rev. Lett.*, 48:1507–1510, 1982.
19. C. Grebogi, E. Ott, and J.A. Yorke. Crises, sudden changes in chaotic attractors, and transient chaos. *Physica D*, 7:181–200, 1983.
20. K.T. Alligood, T. Sauer, and J.A. Yorke. *Chaos: an introduction to dynamical systems*. Springer Verlag, 1996.
21. R.C. Hilborn. *Chaos and nonlinear dynamics*. Oxford Univ. Pr., 2000.
22. E. Ott. *Chaos in dynamical systems*. Cambridge Univ. Pr., 2002.
23. Y. Pomeau and P. Manneville. Intermittent transition to turbulence in dissipative dynamical systems. *Commun. Math. Phys.*, 74:189–197, 1980.
24. M. Di Bernardo, C.J. Budd, A.R. Champneys, and P. Kowalczyk. *Piecewise-smooth dynamical systems: theory and applications*. Springer Verlag, 2008.
25. Z.T. Zhusubaliyev and E. Mosekilde. *Bifurcations and chaos in piecewise-smooth dynamical systems*. World Scientific, 2003.
26. S. Banerjee and G.C. Verghese. *Nonlinear Phenomena in Power Electronics: Attractors, Bifurcations, Chaos, Control and Applications*. IEEE Press, 2001.
27. H.E. Nusse and J.A. Yorke. Border-collision bifurcations including. *Physica D*, 57:39–57, 1992.
28. H.E. Nusse and J.A. Yorke. Border-collision bifurcations for piecewise smooth one-dimensional maps. *Int. J. Bifurcat. Chaos*, 5:189–208, 1995.
29. S. Banerjee et al. Bifurcations in one-dimensional piecewise smooth maps-theory and applications in switching circuits. *IEEE T. Circuits-I*, 47:389–394, 2000.
30. P. Jain and S. Banerjee. Border collision bifurcations in one-dimensional discontinuous maps. *Int. J. Bifurcat. Chaos*, 13:3341–3352, 2003.
31. R.M. May et al. Time delays, density-dependence and single-species oscillations. *J. Anim. Ecol.*, 43:747–770, 1974.
32. G.C. Varley, G.R. Gradwell, and M.P. Hassell. *Insect population ecology: an analytical approach*. University of California Pr., 1973.
33. M.P. Hassell. Density-dependence in single-species populations. *J. Anim. Ecol.*, 44:283–295, 1975.
34. R.M. May and G.F. Oster. Bifurcations and dynamic complexity in simple ecological models. *Am. Nat.*, 110:573–599, 1976.
35. R.M. May. Biological populations obeying difference equations: stable points, stable cycles, and chaos. *J. Theor.Biol.*, 51:511–524, 1975.
36. S.J. Hogan, L. Higham, and T.C.L. Griffin. Dynamics of a piecewise linear map with a gap. *Proc. R. Soc. A*, 463:49–65, 2007.
37. P. Collet and J.P. Eckmann. *Iterated maps on the interval as dynamical systems*. Birkhauser, 1980.
38. J.A. Oteo and J. Ros. Double precision errors in the logistic map: Statistical study and dynamical interpretation. *Phys. Rev. E*, 76:036214, 2007.

39. D.H. Bailey. Algorithm 719: Multiprecision translation and execution of fortran programs. *ACM T. Math. Software*, 19:288–319, 1993.
40. D.H. Bailey. High-precision floating-point arithmetic in scientific computation. *Comput. Sci. Eng.*, 7:54–61, 2005.
41. R.V. Jensen and C.R. Myers. Images of the critical points of nonlinear maps. *Phys. Rev. A*, 32:1222–1224, 1985.
42. J. Eidson et al. Elementary explanation of boundary shading in chaotic-attractor plots for the feigenbaum map and the circle map. *Phys. Rev. A*, 33:2809–2812, 1986.
43. Y.C. Lai, C. Grebogi, and J.A. Yorke. Sudden change in the size of chaotic attractors: how does it occur. In J.H. Kim and J. Stringer, editors, *Applied Chaos*, pages 441–455. Wiley, 1992.
44. C. Beck and F. Schlögl. *Thermodynamics of chaotic systems: an introduction*. Cambridge Univ. Pr., 1995.
45. Y.L. Maistrenko and V.L. Maistrenko. Cycles of chaotic intervals in a time-delayed chua's circuit. *Int. J. Bifurcat. Chaos*, 3:1557–1557, 1993.
46. C. Grebogi et al. Critical exponents for crisis-induced intermittency. *Phys. Rev. A*, 36:5365–5380, 1987.
47. P. Diamond et al. Collapsing effects in numerical simulation of a class of chaotic dynamical systems and random mappings with a single attracting centre. *Physica D*, 86:559–571, 1995.
48. G. Yuan and J.A. Yorke. Collapsing of chaos in one dimensional maps. *Physica D*, 136:18–30, 2000.
49. H.E. Nusse, J.A. Yorke, B.R. Hunt, and E.J. Kostelich. *Dynamics: numerical explorations*. Springer Verlag, 1998.
50. L. Gardini, I. Sushko, and A.K. Naimzada. Growing through chaotic intervals. *J. Econ. Theory*, 143:541–557, 2008.
51. K. Matsuyama. Growing through cycles. *Econometrica*, 67:335–347, 1999.
52. V. Avrutin and M. Schanz. On multi-parametric bifurcations in a scalar piecewise-linear map. *Nonlinearity*, 19:531–552, 2006.
53. V. Avrutin and M. Schanz. On the fully developed bandcount adding scenario. *Nonlinearity*, 21:1077–1103, 2008.
54. R. Lozi. Un attracteur étrange (?) du type attracteur de Hénon. *J. Phys-Paris*, 39:C5–9, 1978.
55. M. Hénon. A two-dimensional mapping with a strange attractor. *Commun. Math. Phys.*, 50:69–77, 1976.
56. M. Misiurewicz. Strange attractors for the lozi mappings. *Ann. NY Acad. Sci.*, 357:348–358, 1980.
57. D. Baptista, R. Severino, and S. Vinagre. The basin of attraction of lozi mappings. *Int. J. Bifurcat. Chaos*, 19:1043–1049, 2009.
58. S. Banerjee and C. Grebogi. Border collision bifurcations in two-dimensional piecewise smooth maps. *Phys. Rev. E*, 59:4052–4061, 1999.
59. E. Zeraoulia and J.C. Sprott. A new simple 2-d piecewise linear map. *J. Syst. Sci. Complex*, 23:379–389, 2010.
60. M.A. Aziz-Alaoui, C. Robert, and C. Grebogi. Dynamics of a henon-lozi-type map. *Chaos Soliton. Fract.*, 12:2323–2341, 2001.
61. R.L. Devaney. A piecewise linear model for the zones of instability of an area-preserving map. *Physica D*, 10:387–393, 1984.
62. D. Aharonov, R.L. Devaney, and U. Elias. The dynamics of a piecewise linear map and its smooth approximation. *Int. J. Bifurcat. Chaos*, 7:351–372, 1997.
63. J.C. Sprott. *Chaos and time-series analysis*. Oxford Univ. Pr., 2003.
64. M. Mitchell. *Complexity: A guided tour*. Oxford Univ. Pr., 2009.
65. H.A. Simon. The architecture of complexity. *P. Am. Philos. Soc.*, 106:467–482, 1962.
66. B. Bollobás. *Modern graph theory*. Springer Verlag, 1998.
67. S. Milgram. The small world problem. *Psychol. Today*, 2:60–67, 1967.
68. D.J. Watts and S.H. Strogatz. Collective dynamics of 'small-world'networks. *Nature*, 393:440–442, 1998.
69. A.L. Barabási and R. Albert. Emergence of scaling in random networks. *Science*, 286:509, 1999.
70. R. Pastor-Satorras, J.M. Rubí, and A. Diaz-Guilera. *Statistical mechanics of complex networks*. Springer Verlag, 2003.
71. A. Barrat, M. Barthlemy, and A. Vespignani. *Dynamical processes on complex networks*. Cambridge Univ. Pr., 2008.
72. A. Pikovsky, M. Rosenblum, and J. Kurths. *Synchronization: A universal concept in nonlinear sciences*. Cambridge Univ. Pr., 2003.
73. S.H. Strogatz. *Sync: The emerging science of spontaneous order*. Hyperion, 2003.
74. Y. Kuramoto. Self-entrainment of a population of coupled non-linear oscillators. In *International symposium on mathematical problems in theoretical physics*, pages 420–422. Springer, 1975.
75. S.H. Strogatz. From kuramoto to crawford: exploring the onset of synchronization in populations of coupled oscillators. *Physica D*, 143:1–20, 2000.
76. K. Kaneko and I. Tsuda. *Complex systems: chaos and beyond: a constructive approach with applications in life sciences*. Springer Verlag, 2001.
77. A. Arenas et al. Synchronization in complex networks. *Phys. Rep.*, 469:93–153, 2008.
78. I. Stewart, M. Golubitsky, and M. Pivato. Symmetry groupoids and patterns of synchrony in coupled cell networks. *SIAM J. Appl. Dynam. Sys.*, 2:609–646, 2003.

79. M. Golubitsky, M. Nicol, and I. Stewart. Some curious phenomena in coupled cell networks. *J. Nonlinear Sci.*, 14:207–236, 2004.
80. M. Field. Combinatorial dynamics. *Dynamical Systems*, 19:217–243, 2004.
81. M. Aguiar et al. Dynamics of coupled cell networks: synchrony, heteroclinic cycles and inflation. *J. Nonlinear Sci.*, 21:271–323, 2011.
82. N. Agarwal and M. Field. Dynamical equivalence of networks of coupled dynamical systems: I. Asymmetric inputs. *Nonlinearity*, 23:1245–1268, 2010.
83. T. Gross and B. Blasius. Adaptive coevolutionary networks: a review. *J. R. Soc. Interface*, 5:259–271, 2008.
84. T. Gross and H. Sayama. *Adaptive Networks: Theory, Models and Applications*. Springer Verlag, 2009.
85. I.J. Gomez Portillo, P.M. Gleiser, and O. Sporns. An adaptive complex network model for brain functional networks. *PLoS One*, 4:418–425, 2009.
86. P.M. Gleiser and V.I. Spoormaker. Modelling hierarchical structure in functional brain networks. *Philos. T. Roy. Soc. A*, 368:5633, 2010.
87. T. Gross, C. D'Lima, and B. Blasius. Epidemic Dynamics on an Adaptive Network. *Phys. Rev. Lett.*, 96:208701, 2006.
88. T. Gross and I.G. Kevrekidis. Robust oscillations in SIS epidemics on adaptive networks: Coarse graining by automated moment closure. *Europhys. Lett.*, 82:38004, 2008.
89. L.B. Shaw and I.B. Schwartz. Enhanced vaccine control of epidemics in adaptive networks. *Phys. Rev. E*, 81:046120, 2010.
90. B. Kozma and A. Barrat. Consensus formation on adaptive networks. *Phys. Rev. E*, 77:016102, 2008.
91. C. Nardini, B. Kozma, and A. Barrat. Who's talking first? Consensus or lack thereof in coevolving opinion formation models. *Phys. Rev. Lett.*, 100:158701, 2008.
92. S. Boccaletti, V. Latora, Y. Moreno, M. Chavez, and D.U. Hwang. Complex networks: Structure and dynamics. *Phys. Rep.*, 424:175–308, 2006.
93. M.E.J. Newman, A.L. Barabasi, and D.J. Watts. *The Structure and Dynamics of Networks*. Princeton Univ. Pr., 2006.
94. J. Ito and K. Kaneko. Spontaneous Structure Formation in a Network of Chaotic Units with Variable Connection Strengths. *Phys. Rev. Lett.*, 88:028701, 2001.
95. J. Ito and K. Kaneko. Spontaneous structure formation in a network of dynamic elements. *Phys. Rev. E*, 67:046226, 2003.
96. Z. Fan and G. Chen. Evolving networks driven by node dynamics. *Int. J. Mod. Phys. B*, 18:2540–2546, 2004.
97. D. Van Den Berg and C. Van Leeuwen. Adaptive rewiring in chaotic networks renders small-world connectivity with consistent clusters. *Europhys. Lett.*, 65:459–464, 2004.
98. P Gong and C. Van Leeuwen. Evolution to a small-world network with chaotic units. *Europhys. Lett.*, 67:328–333, 2004.
99. C. Zhou and J. Kurths. Dynamical Weights and Enhanced Synchronization in Adaptive Complex Networks. *Phys. Rev. Lett.*, 96:164102, 2006.
100. W. Lu. Adaptive dynamical networks via neighborhood information: Synchronization and pinning control. *Chaos*, 17:023122, 2007.
101. T. Aoki and T. Aoyagi. Co-evolution of phases and connection strengths in a network of phase oscillators. *Phys. Rev. Lett.*, 102:34101, 2009.
102. M. Li, S. Guan, and C-H Lai. Spontaneous formation of dynamical groups in an adaptive networked system. *New J. Phys.*, 12:103032, 2010.
103. A. Scirè, I. Tuval, and V.M. Eguíluz. Dynamic modeling of the electric transportation network. *Europhys. Lett.*, 71:318–324, 2005.
104. G.C.M.A. Ehrhardt, M. Marsili, and F. Vega-Redondo. Phenomenological models of socioeconomic network dynamics. *Phys. Rev. E*, 74:036106, 2006.
105. H.F. Kwok et al. Robust emergence of small-world structure in networks of spiking neurons. *Cogn. Neurodyn.*, 1:39–51, 2007.
106. C. Meisel and T. Gross. Adaptive self-organization in a realistic neural network model. *Phys. Rev. E*, 80:061917, 2009.
107. K. Kaneko. Supertransients, spatiotemporal intermittency and stability of fully developed spatiotemporal chaos. *Phys. Lett. A*, 149:105–112, 1990.
108. C. Quince, P.G. Higgs, and A.J. McKane. Topological structure and interaction strengths in model food webs. *Ecol. Model.*, 187:389–412, 2005.
109. M. Golubitsky, K. Josic, and E. Shea-Brown. Winding numbers and average frequencies in phase oscillator networks. *J. Nonlinear Sci.*, 16:201–231, 2006.
110. K. Kaneko. Spatial period-doubling in open flow. *Phys. Lett. A*, 111:321–325, 1985.
111. F.H. Willeboordse and K. Kaneko. Pattern dynamics of a coupled map lattice for open flow. *Physica D*, 86:428–455, 1995.
112. O. Rudzick and A. Pikovsky. Unidirectionally coupled map lattice as a model for open flow systems. *Phys. Rev. E*, 54:5107–5115, 1996.
113. A. Yamaguchi. On the mechanism of spatial bifurcations in the open flow system. *Int. J. Bifurcat. Chaos*, 7:1529–1538, 1997.
114. U. Alon. Network motifs: theory and experimental approaches. *Nat. Rev. Genet.*, 8:450–461, 2007.

115. S. Parthasarathy and J. Guemez. Synchronisation of chaotic metapopulations in a cascade of coupled logistic map models. *Ecol. model.*, 106:17–25, 1998.
116. M. Gyllenberg, G. Söderbacka, and S. Ericsson. Does migration stabilize local population dynamics? Analysis of a discrete metapopulation model. *Math. Biosci.*, 118:25–49, 1993.
117. A.L. Lloyd. The coupled logistic map: a simple model for the effects of spatial heterogeneity on population dynamics. *J. Theor. Biol.*, 173:217–230, 1995.
118. B.E. Kendall and G.A. Fox. Spatial Structure, Environmental Heterogeneity, and Population Dynamics: Analysis of the Coupled Logistic Map. *Theor. Popul. Biol.*, 54:11–37, 1998.
119. H. Helmholtz. Messungen über den zeitlichen verlauf der zuckung animalischer muskeln und die fortpflanzungsgeschwindigkeit der reizung in den nerven. *Archiv für Anatomie, Physiologie und wissenschaftliche Medicin*, pages 276–364, 1850.
120. S. Ramón y Cajal. Estructura de los centros nerviosos de las aves. *Revista trimestral de histología normal y patológica*, 1:1–30, 1888.
121. E.D. Adrian and D.W. Bronk. The discharge of impulses in motor nerve fibres. *J. Physiol.*, 66:81–101, 1928.
122. A.L. Hodgkin, A.F. Huxley, and B. Katz. *J. Physiol.*, 116:424–448, 449–472, 473–496, 497–506, 1952.
123. E. R. Kandel. *In search of memory: the emergence of a new science of mind*. W.W. Norton, 2006.
124. S. Finger. *Minds behind the brain: A history of the pioneers and their discoveries*. Oxford Univ. Pr., 2005.
125. E. Olbrich, P. Achermann, and T. Wennekers. The sleeping brain as a complex system. *Philos. T. Roy. Soc. A*, 369:3697–3707, 2011.
126. D.R. Chialvo. Emergent complex neural dynamics. *Nat. Phys.*, 6:744–750, 2010.
127. O. Sporns. *Networks of the Brain*. The MIT Press, 2010.
128. M. Chavez et al. Complex networks: new trends for the analysis of brain connectivity. *Int. J. Bifurcat. Chaos*, 20:1677–1686, 2010.
129. E.R. Kandel et al. *Principles of neural science*. Elsevier, 1991.
130. P.L. Nunez and R. Srinivasan. *Electric fields of the brain: the neurophysics of EEG*. Oxford Univ. Pr., 2006.
131. P. Mitra and H. Bokil. *Observed brain dynamics*. Oxford Univ. Pr., 2008.
132. M. Steriade. *The intact and sliced brain*. The MIT Press, 2001.
133. B.E. Swartz and E.S. Goldensohn. Timeline of the history of eeg and associated fields. *Electroen. Clin. Neuro.*, 106:173–176, 1998.
134. G. Buzsáki. *Rhythms of the Brain*. Oxford Univ. Pr., 2006.
135. G. Buzsáki and A. Draguhn. Neuronal oscillations in cortical networks. *Science*, 304:1926–1929, 2004.
136. A.L. Loomis, E.N. Harvey, and GA Hobart. Cerebral states during sleep, as studied by human brain potentials. *J. Exp. Psychol.*, 21:127–144, 1937.
137. A. Rechtschaffen and A. Kales. *A manual of standardized terminology, techniques and scoring system for sleep stages of human subjects*. US Dept. of Health, Education, and Welfare, 1968.
138. C. Iber et al. *The AASM Manual for the Scoring of Sleep and Associated Events: Rules, Terminology and Technical Specifications*. AASM, Westchester, 2007.
139. M.A. Chornet Lurbe. *Análisis cuantitativo de electroencefalogramas de sueño y vigilia*. Universitat de València, 2004.
140. W.O. Tatum. *Handbook of EEG interpretation*. Demos Medical Publishing, 2007.
141. M. Steriade, A. Nunez, and F. Amzica. A novel slow (< 1 Hz) oscillation of neocortical neurons in vivo: depolarizing and hyperpolarizing components. *J. Neurosci.*, 13:3252–3265, 1993.
142. R. Huber et al. Arm immobilization causes cortical plastic changes and locally decreases sleep slow wave activity. *Nat. Neurosci.*, 9:1169–1176, 2006.
143. Y.D. Van Der Werf et al. Sleep benefits subsequent hippocampal functioning. *Nat. Neurosci.*, 12:122–123, 2009.
144. M. Massimini et al. The sleep slow oscillation as a traveling wave. *J. Neurosci.*, 24:6862–6870, 2004.
145. M. Murphy et al. Source modeling sleep slow waves. *P. Natl. Acad. Sci. USA*, 106:1608–1613, 2009.
146. M.H. Mohajerani et al. Mirrored bilateral slow-wave cortical activity within local circuits revealed by fast bihemispheric voltage-sensitive dye imaging in anesthetized and awake mice. *J. Neurosci.*, 30:3745–3751, 2010.
147. P. Achermann and AA Borbely. Low-frequency ($<$1Hz) oscillations in the human sleep electroencephalogram. *Neuroscience*, 81:213–222, 1997.
148. Y. Isomura et al. Integration and segregation of activity in entorhinal-hippocampal subregions by neocortical slow oscillations. *Neuron*, 52:871–882, 2006.
149. M.V. Sanchez-Vives and D.A. McCormick. Cellular and network mechanisms of rhythmic recurrent activity in neocortex. *Nat. Neurosci.*, 3:1027–1034, 2000.
150. M. Steriade, A. Nunez, and F. Amzica. Intracellular analysis of relations between the slow (< 1 Hz) neocortical oscillation and other sleep rhythms of the electroencephalogram. *J. Neurosci.*, 13:3266–3283, 1993.
151. M. Volgushev et al. Precise long-range synchronization of activity and silence in neocortical neurons during slow-wave sleep. *J. Neurosci.*, 26:5665–5672, 2006.

152. M. Steriade et al. The slow (< 1 hz) oscillation in reticular thalamic and thalamocortical neurons: scenario of sleep rhythm generation in interacting thalamic and neocortical networks. *J. Neurosci.*, 13:3284–3299, 1993.
153. V. Crunelli and S.W. Hughes. The slow (< 1 hz) rhythm of non-rem sleep: a dialogue between three cardinal oscillators. *Nat. Neurosci.*, 13:9–17, 2009.
154. T.J. Sejnowski and A. Destexhe. Why do we sleep? *Brain Res.*, 886:208–223, 2000.
155. R. Huber et al. Local sleep and learning. *Nature*, 430:78–81, 2004.
156. S. Diekelmann and J. Born. The memory function of sleep. *Nat. Rev. Neurosci.*, 11:114–126, 2010.
157. G. Tononi and C. Cirelli. Sleep function and synaptic homeostasis. *Sleep Med. Rev.*, 10:49–62, 2006.
158. C. Cirelli and G. Tononi. Is sleep essential? *PLoS Biol.*, 6:e216, 2008.
159. R. Csercsa et al. Laminar analysis of slow wave activity in humans. *Brain*, 133:2814, 2010.
160. S.S. Cash et al. The human k-complex represents an isolated cortical down-state. *Science*, 324:1084–1087, 2009.
161. Y. Nir et al. Regional slow waves and spindles in human sleep. *Neuron*, 70:153–169, 2011.
162. F. Amzica and M. Steriade. Electrophysiological correlates of sleep delta waves. *Electroen. Clin. Neuro.*, 107:69–83, 1998.
163. B.A. Riedner et al. Sleep homeostasis and cortical synchronization: III. A high-density EEG study of sleep slow waves in humans. *Sleep*, 30:1643–1657, 2007.
164. J. Talairach and P. Tournoux. *Co-planar stereotaxic atlas of the human brain*. Thieme Medical Publisher, 1988.
165. R. Ferri et al. Dynamics of the eeg slow-wave synchronization during sleep. *Clin. Neurophysiol.*, 116:2783–2795, 2005.
166. I. Timofeev and M. Steriade. Low-frequency rhythms in the thalamus of intact-cortex and decorticated cats. *J. Neurophysiol.*, 76:4152–4168, 1996.
167. J.N. MacLean et al. Internal dynamics determine the cortical response to thalamic stimulation. *Neuron*, 48:811–823, 2005.
168. P. Rigas and M.A. Castro-Alamancos. Thalamocortical up states: differential effects of intrinsic and extrinsic cortical inputs on persistent activity. *J. Neurosci.*, 27:4261–4272, 2007.
169. I. Timofeev et al. Origin of slow cortical oscillations in deafferented cortical slabs. *Cereb. Cortex*, 10:1185–1199, 2000.
170. D. Holcman and M. Tsodyks. The emergence of up and down states in cortical networks. *PLoS Comput. Biol.*, 2:e23, 2006.
171. M.G. Terzano et al. Atlas, rules, and recording techniques for the scoring of cyclic alternating pattern (cap) in human sleep. *Sleep Med.*, 2:537–554, 2001.
172. S. Hill and G. Tononi. Modeling sleep and wakefulness in the thalamocortical system. *J. Neurophysiol.*, 93:1671–1698, 2005.
173. F. Amzica and M. Steriade. Short-and long-range neuronal synchronization of the slow (< 1 hz) cortical oscillation. *J. Neurophysiol.*, 73:20–38, 1995.
174. E. Parzen. On estimation of a probability density function and mode. *Ann. Math. Stat.*, 33:1065–1076, 1962.